Summer 2021

Plasmonic Metallic and Semiconductor Nanomaterials

Mengqi Sun

Plasmonic Metallic and Semiconductor Nanomaterials

by

Mengqi Sun

Bachelor of Science
University of Illinois at Urbana-Champaign, 2016

Submitted in Partial Fulfillment of the Requirements

For the Degree of Doctor of Philosophy in

Chemistry

College of Arts and Science

University of South Carolina

2021

Accepted by:

Hui Wang, Major Professor

Richard D. Adams, Committee Member

Aaron K. Vannucci, Committee Member

Hans-Conrad zur Loye, Committee Member

Fanglin Chen, Committee Member

Tracey L. Weldon, Interim Vice Provost and Dean of the Graduate School

ACKNOWLEDGEMENTS

First and foremost, I would like to acknowledge the support of my advisor, Dr. Hui Wang. Without him, I do not think I can achieve what I have achieved during my PhD year. It has been five years since I joined the group. Five years ago, you saw me as a 22-year-old child who was fresh, energetic, and always spoke up his mind without much filtering. Five years later, today you probably see me as a 27-year-old child who still is fresh, energetic, and always speaks up his mind without much filtering, but perhaps also with a little bit of maturity, resilience, and reverence for science. Throughout the past five years, it was your passions and standards for scientific research that shaped me both as a person and as a researcher. This zealous pursuit of knowledge will continue.

"Passion is like fire. It will fill you with motivation and purpose like no others, but it will also burn you". This is a quote from a movie that I watched years ago. Now, I am more and more resonant with that. There should always be other aspects of my life that keep me grounded. Therefore, in the second part of this acknowledgement, I would like to acknowledge the support and sacrifice of my families. My mom has always wanted grandchild. I have disappointed her in that regard for the last five years. I appreciated that she understood and respected the decision that I have prioritized my career. My dad told me that he was immensely proud of me, a few weeks ago. I know for a 54-year-old male who is not always expressive with his emotions, it was not easy. I am immensely appreciative of him for saying that too. As I progressed my career path

forward, I hoped that I never forget to realize how important they are to me and that my family should be my number one reason to work hard.

Last but not least, I would like to acknowledge the support of my friends, both in and out of the Department of Chemistry. They either provided valuable guidance on my career or being very supportive in my personal life. I will certainly cherish the companionship of all of my friends that I am blessed to have them in my life. Guangfang and Xiaoqi were among the first people I knew when I first joined the group. They showed me what a diligent, hard-working, and experienced researcher should be. They have made my learning process in PhD easier for me. For that, I am enormously grateful.

ABSTRACT

The earliest account of localized surface plasmon resonance (LSPR) has to date back to the ancient age of Rome in 400 A.D. The famous glass of Lycurgus cup told the story of unique light-and-matter interaction at the nanoscale that confines the electromagnetic field resonance at its surface and therefore allows LSPR feature to noticeably arise. The conventional metallic LSPR nanomaterials, like Au and Ag nanoparticles attract constant attentions due to their synthetic simplicity, chemical robustness, and visible spectral response. Its ability to generate sensitive dielectric sensing of the surroundings, strong electromagnetic field and active charge carriers upon optical excitation triggered widespread curiosities among researchers. However, there are growing interests for LSPR semiconductor nanomaterials as well. It is believed that LSPR of semiconductor nanomaterials exhibits a higher degree of tunability and broader range of spectral coverage deep into the infrared spectrum than LSPR of metallic nanomaterials. As a result, both of these metallic and semiconductor LSPRs have received relentless interests in the field of optics, biomedicines, catalysis, etc.

In this dissertation, I will focus my discussion on the synthetic challenge, material-specific plasmonic properties, and photocatalytic or photothermal behaviors of plasmonic metallic and semiconductor nanomaterials.

TABLE OF CONTENTS

LIST OF FIGURES

CHAPTER 1

INTRODUCTION

1.1 Overview

The old and legendary story about the origins of plasmons is still tirelessly circulating in the researcher community: the glass of Lycurgus cup back in the age of ancient Rome in 400 A.D exhibited abnormal patterns of showing different colors, observed in different light-and-matter interactions from plasmonic nanoparticles embedded in the glass[1-2]. As opposed to bulk materials, plasmonic materials at the nanoscale are able to confine the plasmonic energy to their surface strongly enough to allow detectable and useful spectral transition, hence named localized surface plasmon resonance (LSPR). Dictated by the intrinsic polarizability (dielectric function) of the materials, the plasmonic properties of nanoparticles can also be determined by many factors: free carriers concentration level; shapes and sizes of the nanoparticles; orientation of incident electromagnetic field; crystalline structures of the nanoparticles, etc[1, 3-4]. It is therefore an intriguing topic enriched with optical and physical fundamental theorems and promising photonic applications.

To understand better, given that the particle is smaller than the wavelength of incident light, Mie scattering theory[5] can effectively break down the contribution from scattering (σ_{sct}) and absorption (σ_{abs}) components of incident light by the conducting spherical particle or molecule and yield expressions for their cross-sections[2, 6]:

$$\sigma_{ext} = \frac{18\pi\varepsilon_m^{3/2}V}{\lambda}\frac{\varepsilon_2(\lambda)}{[\varepsilon_1(\lambda)+2\varepsilon_m(\lambda)]^2+\varepsilon_2(\lambda)^2}$$

$$\sigma_{sct} = \frac{32\pi^4{\varepsilon_m}^2V^2}{\lambda^4}\frac{(\varepsilon_1-\varepsilon_m)^2+(\varepsilon_2)^2}{(\varepsilon_1+2\varepsilon_m)^2+(\varepsilon_2)^2}$$

$$\sigma_{abs} = \sigma_{ext} - \sigma_{sct}$$

where σ_{ext} is the cross-section of extinction, ε_m is the dielectric function of the medium, V is the volume of the spherical particle, λ is the wavelength, ε_1 and ε_2 are the real and imaginary part of complex dielectric functions of metals. The peak position of LSPR can be predicted using these equations. If σ_{ext} reached maximum, the denominator needed to be at its minimum where $\varepsilon_1 = -2\varepsilon_m$. Then at the wavelength where $\varepsilon_1 = -2\varepsilon_m$, LSPR will reach its peak intensity.

The classical Drude-Lorenz model[7] also provides simplified approximation in predicting and modeling behaviors of LSPR materials by demonstrating the classical nature of free electron and heavy lattice collisions[2, 8-9]. Despite its limitation, it has been convenient and useful in relating the peak position of metallic LSPR (λ_{max}) to the refractive index (n_m) of the medium, giving important basis for metallic LSPR-based sensing techniques[2]:

$$\lambda_{max} = \lambda_p(\sqrt{2{n_m}^2 + 1})$$

where λ_p is the plasma frequency of the bulk materials.

The versatile plasmonic nanomaterials can be used in many areas with suitable plasmonic capability: Surface Enhanced Raman Spectroscopy (SERS) due to the redirection of incident light and resultant electromagnetic field[10-13]; Photovoltaics and photocatalysis due to the creation of electron-hole pairs via nonradiative decay of LSPR[14-19]; Photothermal therapies due to the thermal relaxation of the electron-hole pairs[20-24]; Sensing due to the sensitivity of LSPR peaks to the dielectric medium of the

surroundings[3, 25-26]. Many plasmonic candidates have received relentless attentions, among which metallic and semiconductor nanomaterials have been researched more extensively. In this introductory Chapter, varieties of plasmonic metallic and semiconductor nanomaterials and their respective plasmonic properties will be discussed.

1.2 Plasmonic Metallic Nanomaterials

Coinage noble metals (Au, Ag, and Cu) are among the conventional class of plasmonic nanomaterials that have been studied much earlier and much thoroughly, especially Au and Ag because of their desirable dielectric characteristics, chemical robustness, and synthetic simplicity of controlling the shapes and sizes of nanoparticles[2, 27-28].

LSPR of noble metals can be regarded as oscillatory electron clouds with high-kinetic-energy charge carriers that decay following either a nonradiative pathway to produce charge carriers through Landau damping or a radiative pathway to generate strong electromagnetic field. Both of these processes lay the mechanistic foundation for applications of LSPR nanomaterials.

Typically, parameters involved for plasmonic tunabilites are either intrinsic properties, like free carrier concentrations or crystalline phases of the plasmonic nanomaterials, or geometrical factors such as the shapes and sizes of the nanomaterials or refractive index of the medium. Due to the inherent inertness of noble metals, their free carrier concentration is fixed at about 10^{23} cm^{-3} and therefore difficult to be manipulated. Often, it is the geometrical parameters like shapes and sizes of the plasmonic metallic nanoparticle that were the variables.

Nanospheres are the simplest nanostructures with high surface-to-volume ratio, great symmetries, and strong absorption capabilities at smaller size. Merely by tuning the particle sizes, LSPR of Au nanospheres is able to cover the entire visible spectrum[3, 29]. Other nanostructures, such as nanorods[13, 24, 30-31], nanocubes[32-33], and nanoshells[28, 34-36] were also obtained with excellent shape controllability. The symmetry breaking not only exposed high-index facets that are advantageous catalytically, but also created more plasmonic modes that are otherwise hard to experimentally achieve on symmetrical nanospheres[37-38], providing experimental complement for theoretical investigation in noble metallic LSPR.

Noble metallic LSPR has witnessed tremendous advancement in the last decades, with respect to both theoretical elucidation and application merits. Particularly, in the bio-related research community, plasmonic noble metals has been hugely desirable because of its sensitive and intense LSPR signals. The challenges often are the synthesis of these noble metal nanoparticles with high monodispersity, well-defined structures, controllable shapes and sizes.

1.3 Plasmonic Semiconductors Nanomaterials

Unlike the plasmonic metals, plasmonic semiconductor nanomaterials exhibited LSPR mainly through dopants. Upon doping, free carrier concentration can be tuned to appreciable level in order for LSPR to be augmented enough to arise in the mid-infrared or near-infrared range[1, 4, 39-40]. Geometrical aspects are often in supplementary role when semiconductors LSPR tunability was described.

Familiar plasmonic semiconductor nanomaterials include metal chalcogenide[41-47], metal oxides[48-49], and nitrides[50-51]. Through doping, their plasmonic characteristics can emerge, often in the infrared spectrum because of comparatively lower free carrier concentrations than that of the noble metals (about 10^{21}-10^{22} cm^{-3} for metal chalcogenide, 10^{19}-10^{20} cm^{-3} for metal oxide, and 10^{18} cm^{-3} for some nitrides).

Due to the intricacies of electronic band structures tunability of plasmonic semiconductors and relatively low free carriers concentration, theoretical models, like Drude-Lorenz model have met its limitation when trying to explain the dielectric properties of plasmonic semiconductors[1], despite of being effective in some cases[47, 52-53]. Consequently, theoretical advancement and justification of the applicability on semiconductor LSPR are research areas with open questions and challenges.

Other challenges for plasmonic semiconductor nanomaterials mostly lie on doping strategies for LSPR patterns to develop, as well as synthesis of high-quality crystalline semiconductor nanocrystals with controllable geometries and stoichiometries. In addition to the most frequently used chemical doping via inducing chemical reaction to insert or remove dopants[51, 54-55], other treatments were proved to be as feasible and effective: Photochemical charging process would blench out the photoexcited electrons with the aid of hole scavengers and ultimately create intra-conduction band transition, resulting in nonequilibrium free carriers[56-59]; Electrochemically, an external voltage can be applied to accumulate charge carriers and modulate Fermi level of a semiconductor in order to achieve free carriers at nonequilibrium conditions[60-61];

1.4 Conclusion and Outline

In this dissertation, both plasmonic semiconductor and metallic nanomaterials will be illustrated, in conjunction with their well-controlled synthetic techniques, material-specific LSPR properties and fundamentally noteworthy optical behaviors under the photocatalytic or photothermal actions.

First, a novel plasmonic bimetallic material system, Au-Cu alloy nanospheres will be first described in Chapter 2. This atomically well mixed nanomaterial system exhibited unique Au-Cu metallic bond in its atomic unit cell, fundamentally differentiating itself from monometallic Au or Cu. Their plasmonic features together with their bimodal photocatalytic behaviors will be examined. Next, a metal/semiconductor heterostructural nanoparticle will be discussed in Chapter 3. Plasmonic copper sulfide was deposited onto Au nanopsheres to form Au@Copper sulfide core@shell nanoparticles with three distinct copper sulfide stoichiometries: Au@CuS, Au@$Cu_{1.8}S$, and Au@$Cu_{2-x}S$. Their respective LSPR properties will be illustrated, in addition to interesting photocatalytic and photothermal behaviors of Au@CuS nanoparticles. In Chapter 4, two-dimensional CuS and $Cu_{1.8}S$ nanodisks were synthesized. Synthetic mechanism will be discussed, in conjunction with their tunabilties of LSPR and surface work distribution upon crystalline phase transformation.

1.5 References

1. Agrawal, A.; Cho, S. H.; Zandi, O.; Ghosh, S.; Johns, R. W.; Milliron, D. J., Localized Surface Plasmon Resonance in Semiconductor Nanocrystals. *Chem. Rev.* **2018,** *118* (6), 3121-3207.

2. Mayer, K. M.; Hafner, J. H., Localized Surface Plasmon Resonance Sensors. *Chem. Rev.* **2011,** *111* (6), 3828-3857.

3. Jain, P. K.; Huang, X. H.; El-Sayed, I. H.; El-Sayed, M. A., Noble Metals on the Nanoscale: Optical and Photothermal Properties and Some Applications in Imaging, Sensing, Biology, and Medicine. *Acc. Chem. Res.* **2008,** *41* (12), 1578-1586.

4. Coughlan, C.; Ibanez, M.; Dobrozhan, O.; Singh, A.; Cabot, A.; Ryan, K. M., Compound Copper Chalcogenide Nanocrystals. *Chem. Rev.* **2017,** *117* (9), 5865-6109.

5. Mie, G., Articles on the optical characteristics of turbid tubes, especially colloidal metal solutions. *Ann. Phys.* **1908,** *25* (3), 377-445.

6. Anderson, L. J. E.; Mayer, K. M.; Fraleigh, R. D.; Yang, Y.; Lee, S.; Hafner, J. H., Quantitative Measurements of Individual Gold Nanoparticle Scattering Cross Sections. *J. Phys. Chem. C* **2010,** *114* (25), 11127-11132.

7. Drude, P., On the electron theory of metals. *Ann. Phys.* **1900,** *1* (3), 566-613.

8. Giannini, V.; Fernandez-Dominguez, A. I.; Heck, S. C.; Maier, S. A., Plasmonic Nanoantennas: Fundamentals and Their Use in Controlling the Radiative Properties of Nanoemitters. *Chem. Rev.* **2011,** *111* (6), 3888-3912.

9. Zhong, Y. J.; Malagari, S. D.; Hamilton, T.; Wasserman, D., Review of mid-infrared plasmonic materials. *J. Nanophotonics.* **2015,** *9*.

10. Li, W. H.; Zamani, R.; Gil, P. R.; Pelaz, B.; Ibanez, M.; Cadavid, D.; Shavel, A.; Alvarez-Puebla, R. A.; Parak, W. J.; Arbiol, J.; Cabot, A., CuTe Nanocrystals: Shape and Size Control, Plasmonic Properties, and Use as SERS Probes and Photothermal Agents. *J. Am. Chem. Soc.* **2013,** *135* (19), 7098-7101.

11. Nikoobakht, B.; Wang, J. P.; El-Sayed, M. A., Surface-enhanced Raman scattering of molecules adsorbed on gold nanorods: off-surface plasmon resonance condition. *Chem. Phys. Lett.* **2002,** *366* (1-2), 17-23.

12. Jackson, J. B.; Halas, N. J., Surface-enhanced Raman scattering on tunable plasmonic nanoparticle substrates. *Proc. Natl. Acad. Sci. U.S.A.* **2004,** *101* (52), 17930-17935.

13. Nikoobakht, B.; El-Sayed, M. A., Surface-enhanced Raman scattering studies on aggregated gold nanorods. *J. Phys. Chem. A* **2003,** *107* (18), 3372-3378.

14. Wu, Y.; Wadia, C.; Ma, W. L.; Sadtler, B.; Alivisatos, A. P., Synthesis and photovoltaic application of copper(I) sulfide nanocrystals. *Nano Lett.* **2008,** *8* (8), 2551-2555.

15. Kale, M. J.; Avanesian, T.; Christopher, P., Direct Photocatalysis by Plasmonic Nanostructures. *ACS Catal.* **2014,** *4* (1), 116-128.

16. Boerigter, C.; Aslam, U.; Linic, S., Mechanism of Charge Transfer from Plasmonic Nanostructures to Chemically Attached Materials. *ACS Nano* **2016,** *10* (6), 6108-6115.

17. Wu, K.; Chen, J.; McBride, J. R.; Lian, T., Efficient hot-electron transfer by a plasmon-induced interfacial charge-transfer transition. *Science* **2015,** *349* (6248), 632-635.

18. Cui, J. B.; Li, Y. J.; Liu, L.; Chen, L.; Xu, J.; Ma, J. W.; Fang, G.; Zhu, E. B.; Wu, H.; Zhao, L. X.; Wang, L. Y.; Huang, Y., Near-Infrared Plasmonic-Enhanced Solar Energy Harvest for Highly Efficient Photocatalytic Reactions. *Nano Lett.* **2015,** *15* (10), 6295-6301.

19. Gan, X. Y.; Keller, E. L.; Warkentin, C. L.; Crawford, S. E.; Frontiera, R. R.; Millstone, J. E., Plasmon-Enhanced Chemical Conversion Using Copper Selenide Nanoparticles. *Nano Lett.* **2019,** *19* (4), 2384-2388.

20. Govorov, A. O.; Richardson, H. H., Generating heat with metal nanoparticles. *Nano Today* **2007,** *2* (1), 30-38.

21. Murphy, C. J.; Chang, H. H.; Falagan-Lotsch, P.; Gole, M. T.; Hofmann, D. M.; Hoang, K. N. L.; McClain, S. M.; Meyer, S. M.; Turner, J. G.; Unnikrishnan, M.; Wu, M.; Zhang, X.; Zhang, Y. S., Virus-Sized Gold Nanorods: Plasmonic Particles for Biology. *Acc. Chem. Res.* **2019,** *52* (8), 2124-2135.

22. Wang, S. H.; Riedinger, A.; Li, H. B.; Fu, C. H.; Liu, H. Y.; Li, L. L.; Liu, T. L.; Tan, L. F.; Barthel, M. J.; Pugliese, G.; De Donato, F.; D'Abbusco, M. S.; Meng, X. W.; Manna, L.; Meng, H.; Pellegrino, T., Plasmonic Copper Sulfide Nanocrystals Exhibiting Near-Infrared Photothermal and Photodynamic Therapeutic Effects. *ACS Nano* **2015,** *9* (2), 1788-1800.

23. Hessel, C. M.; Pattani, V. P.; Rasch, M.; Panthani, M. G.; Koo, B.; Tunnell, J. W.; Korgel, B. A., Copper Selenide Nanocrystals for Photothermal Therapy. *Nano Lett.* **2011,** *11* (6), 2560-2566.

24. Huang, X. H.; El-Sayed, I. H.; Qian, W.; El-Sayed, M. A., Cancer cell imaging and photothermal therapy in the near-infrared region by using gold nanorods. *J. Am. Chem. Soc.* **2006,** *128* (6), 2115-2120.

25. Willets, K. A.; Van Duyne, R. P., Localized surface plasmon resonance spectroscopy and sensing. *Annu. Rev. Phys. Chem.* **2007,** *58*, 267-297.

26. Haes, A. J.; Zou, S. L.; Schatz, G. C.; Van Duyne, R. P., Nanoscale optical biosensor: Short range distance dependence of the localized surface plasmon resonance of noble metal nanoparticles. *J. Phys. Chem. B* **2004,** *108* (22), 6961-6968.

27. Yu, C. X.; Irudayaraj, J., Multiplex biosensor using gold nanorods. *Anal. Chem.* **2007,** *79* (2), 572-579.

28. Sun, Y. G.; Xia, Y. N., Increased sensitivity of surface plasmon resonance of gold nanoshells compared to that of gold solid colloids in response to environmental changes. *Anal. Chem.* **2002,** *74* (20), 5297-5305.

29. Link, S.; El-Sayed, M. A., Size and temperature dependence of the plasmon absorption of colloidal gold nanoparticles. *J. Phys. Chem. B* **1999,** *103* (21), 4212-4217.

30. Murphy, C. J.; San, T. K.; Gole, A. M.; Orendorff, C. J.; Gao, J. X.; Gou, L.; Hunyadi, S. E.; Li, T., Anisotropic metal nanoparticles: Synthesis, assembly, and optical applications. *J. Phys. Chem. B* **2005,** *109* (29), 13857-13870.

31. Link, S.; Mohamed, M. B.; El-Sayed, M. A., Simulation of the optical absorption spectra of gold nanorods as a function of their aspect ratio and the effect of the medium dielectric constant. *J. Phys. Chem. B* **1999,** *103* (16), 3073-3077.

32. Hu, M.; Chen, J. Y.; Li, Z. Y.; Au, L.; Hartland, G. V.; Li, X. D.; Marquez, M.; Xia, Y. N., Gold nanostructures: engineering their plasmonic properties for biomedical applications. *Chem. Soc. Rev.* **2006,** *35* (11), 1084-1094.

33. Sun, Y. G.; Mayers, B. T.; Xia, Y. N., Template-engaged replacement reaction: A one-step approach to the large-scale synthesis of metal nanostructures with hollow interiors. *Nano Lett.* **2002,** *2* (5), 481-485.

34. Jain, P. K.; El-Sayed, M. A., Universal scaling of plasmon coupling in metal nanostructures: Extension from particle pairs to nanoshells. *Nano Lett.* **2007,** *7* (9), 2854-2858.

35. Wang, Y. W.; Xie, X. Y.; Wang, X. D.; Ku, G.; Gill, K. L.; O'Neal, D. P.; Stoica, G.; Wang, L. V., Photoacoustic tomography of a nanoshell contrast agent in the in vivo rat brain. *Nano Lett.* **2004,** *4* (9), 1689-1692.

36. Wang, H.; Tam, F.; Grady, N. K.; Halas, N. J., Cu nanoshells: Effects of interband transitions on the nanoparticle plasmon resonance. *J. Phys. Chem. B* **2005,** *109* (39), 18218-18222.

37. Wang, H.; Wu, Y. P.; Lassiter, B.; Nehl, C. L.; Hafner, J. H.; Nordlander, P.; Halas, N. J., Symmetry breaking in individual plasmonic nanoparticles. *Proc. Natl. Acad. Sci. U.S.A.* **2006,** *103* (29), 10856-10860.

38. Jing, H.; Zhang, Q. F.; Large, N.; Yu, C. M.; Blom, D. A.; Nordlander, P.; Wang, H., Tunable Plasmonic Nanoparticles with Catalytically Active High-Index Facets. *Nano Lett.* **2014,** *14* (6), 3674-3682.

39. Luther, J. M.; Jain, P. K.; Ewers, T.; Alivisatos, A. P., Localized surface plasmon resonances arising from free carriers in doped quantum dots. *Nat. Mater.* **2011,** *10* (5), 361-366.

40. Naik, G. V.; Shalaev, V. M.; Boltasseva, A., Alternative Plasmonic Materials: Beyond Gold and Silver. *Adv. Mater.* **2013,** *25* (24), 3264-3294.

41. Zhao, Y. X.; Pan, H. C.; Lou, Y. B.; Qiu, X. F.; Zhu, J. J.; Burda, C., Plasmonic Cu2-xS Nanocrystals: Optical and Structural Properties of Copper-Deficient Copper(I) Sulfides. *J. Am. Chem. Soc.* **2009,** *131* (12), 4253-4261.

42. Kriegel, I.; Jiang, C. Y.; Rodriguez-Fernandez, J.; Schaller, R. D.; Talapin, D. V.; da Como, E.; Feldmann, J., Tuning the Excitonic and Plasmonic Properties of Copper Chalcogenide Nanocrystals. *J. Am. Chem. Soc.* **2012,** *134* (3), 1583-1590.

43. Xie, Y.; Riedinger, A.; Prato, M.; Casu, A.; Genovese, A.; Guardia, P.; Sottini, S.; Sangregorio, C.; Miszta, K.; Ghosh, S.; Pellegrino, T.; Manna, L., Copper Sulfide Nanocrystals with Tunable Composition by Reduction of Covellite Nanocrystals with Cu+ Ions. *J. Am. Chem. Soc.* **2013,** *135* (46), 17630-17637.

44. Kriegel, I.; Rodriguez-Fernandez, J.; Wisnet, A.; Zhang, H.; Waurisch, C.; Eychmuller, A.; Dubavik, A.; Govorov, A. O.; Feldmann, J., Shedding Light on Vacancy-Doped Copper Chalcogenides: Shape-Controlled Synthesis, Optical Properties, and Modeling of Copper Telluride Nanocrystals with Near-Infrared Plasmon Resonances. *ACS Nano* **2013,** *7* (5), 4367-4377.

45. Liu, Y.; Liu, M.; Swihart, M. T., Plasmonic Copper Sulfide-Based Materials: A Brief Introduction to Their Synthesis, Doping, Alloying, and Applications. *J. Phys. Chem. C* **2017,** *121* (25), 13435-13447.

46. Hsu, S. W.; Ngo, C.; Tao, A. R., Tunable and Directional Plasmonic Coupling within Semiconductor Nanodisk Assemblies. *Nano Lett.* **2014,** *14* (5), 2372-2380.

47. Cordova-Castro, R. M.; Casavola, M.; van Schilfgaarde, M.; Krasavin, A. V.; Green, M. A.; Richards, D.; Zayats, A. V., Anisotropic Plasmonic CuS Nanocrystals as a Natural Electronic Material with Hyperbolic Optical Dispersion. *ACS Nano* **2019,** *13* (6), 6550-6560.

48. Liu, Z. K.; Zhong, Y. X.; Shafei, I.; Jeong, S.; Wang, L. G.; Nguyen, H. T.; Sun, C. J.; Li, T.; Chen, J.; Chen, L.; Losovyj, Y.; Gao, X. F.; Ma, W. L.; Ye, X. C.,

Broadband Tunable Mid-infrared Plasmon Resonances in Cadmium Oxide Nanocrystals Induced by Size-Dependent Nonstoichiometry. *Nano Lett.* **2020,** *20* (4), 2821-2828.

49. Lounis, S. D.; Runnerstrom, E. L.; Bergerud, A.; Nordlund, D.; Milliron, D. J., Influence of Dopant Distribution on the Plasmonic Properties of Indium Tin Oxide Nanocrystals. *J. Am. Chem. Soc.* **2014,** *136* (19), 7110-7116.

50. Palomaki, P. K. B.; Miller, E. M.; Neale, N. R., Control of Plasmonic and Interband Transitions in Colloidal Indium Nitride Nanocrystals. *J. Am. Chem. Soc.* **2013,** *135* (38), 14142-14150.

51. Barragan, A. A.; Ilawe, N. V.; Zhong, L.; Wong, B. M.; Mangolini, L., A Non-Thermal Plasma Route to Plasmonic TiN Nanoparticles. *J. Phys. Chem. C* **2017,** *121* (4), 2316-2322.

52. Kasic, A.; Schubert, M.; Einfeldt, S.; Hommel, D.; Tiwald, T. E., Free-carrier and phonon properties of n- and p-type hexagonal GaN films measured by infrared ellipsometry. *Phys. Rev. B* **2000,** *62* (11), 7365-7377.

53. Donovan, B. F.; Sachet, E.; Maria, J. P.; Hopkins, P. E., Interplay between mass-impurity and vacancy phonon scattering effects on the thermal conductivity of doped cadmium oxide. *Appl. Phys. Lett.* **2016,** *108* (2).

54. Dorfs, D.; Hartling, T.; Miszta, K.; Bigall, N. C.; Kim, M. R.; Genovese, A.; Falqui, A.; Povia, M.; Manna, L., Reversible Tunability of the Near-Infrared Valence Band Plasmon Resonance in Cu2-xSe Nanocrystals. *J. Am. Chem. Soc.* **2011,** *133* (29), 11175-11180.

55. Muhammed, M. A. H.; Doblinger, M.; Rodriguez-Fernandez, J., Switching Plasmons: Gold Nanorod-Copper Chalcogenide Core-Shell Nanoparticle Clusters with

Selectable Metal/Semiconductor NIR Plasmon Resonances. *J. Am. Chem. Soc.* **2015,** *137* (36), 11666-11677.

56. Faucheaux, J. A.; Jain, K., Plasmons in Photocharged ZnO Nanocrystals Revealing the Nature of Charge Dynamics. *J. Phys. Chem. Lett.* **2013,** *4* (18), 3024-3030.

57. Gavrilyuk, A. I., Photochromism in WO3 thin films. *Electrochim. Acta* **1999,** *44* (18), 3027-3037.

58. Schimpf, A. M.; Lounis, S. D.; Runnerstrom, E. L.; Milliron, D. J.; Gamelin, D. R., Redox Chemistries and Plasmon Energies of Photodoped In2O3 and Sn-Doped In2O3 (ITO) Nanocrystals. *J. Am. Chem. Soc.* **2015,** *137* (1), 518-524.

59. Haase, M.; Weller, H.; Henglein, A., Photochemistry and Radiation-Chemistry of Colloidal Semiconductors .23. Electron Storage on Zno Particles and Size Quantization. *J. Phys. Chem.* **1988,** *92* (2), 482-487.

60. Garcia, G.; Buonsanti, R.; Runnerstrom, E. L.; Mendelsberg, R. J.; Llordes, A.; Anders, A.; Richardson, T. J.; Milliron, D. J., Dynamically Modulating the Surface Plasmon Resonance of Doped Semiconductor Nanocrystals. *Nano Lett.* **2011,** *11* (10), 4415-4420.

61. Wang, C. J.; Shim, M.; Guyot-Sionnest, P., Electrochromic nanocrystal quantum dots. *Science* **2001,** *291* (5512), 2390-2392.

CHAPTER 2

INTERBAND AND INTRABAND HOT CARRIER-DRIVEN PHOTOCATALYSIS ON PLASMONIC BIMETALLIC NANOPARTICLES: A CASE STUDY OF AU-CU ALLOY NANOPARTICLES

2.1 Introduction

Plasmonic metallic nanomaterials have received extensive attentions due to their versatile photophysical properties. The characteristic collective free-electron clouds that are known as plasmon can be resonant with incident light to provide a unique pathway of creating kinetically energetic charge carriers through Landau damping[1-2]. Localized surface plasmon resonance (LSPR) of noble metallic materials at nanoscale enables them to perform plasmon-driven photocatalysis[3-7]. Once the energy of incident light increases, the $d \rightarrow sp$ interband transition occurs and directly produces lattice-bonded electron-hole pairs with higher energies than the plasmonic charge carriers. This bimodal optical route for generating catalytically active charge carriers of the monometallic coinage noble metal nanomaterials (e.g. Au, Ag, and Cu) has been researched broadly[8-12]. It has been concluded that: (a) the interband transition-produced hot carriers are more catalytically efficient due to longer lifetime than those from the plasmonic intraband (picosecond vs. femtosecond)[10-11]; (b) plasmonic hot electrons possess higher kinetic energy upon excitation, which permits hot electron injections to the conduction band of adjacent semiconductors. The interband hot electrons, on the other hand, do not have high enough kinetic energy to initiate this electron transfer[11-12]; (c) plasmonic charge carriers have shorter lifetime and therefore better photothermal conversion efficiencies than interband charge carriers[11]. However established these claims are about plasmonic monometallic nanomaterials, study on a bimetallic system is otherwise comparatively underwhelming.

Herein, we integrated two noble metals into one nanomaterial system by synthesizing atomically well intermixed Au-Cu alloy nanosparticles (NPs) in spherical shape using a glycol-assisted colloidal synthetic method and explored photocatalytic

behaviors of their photoinduced charge carriers by conducting photocatalytic mineralization of Rhodamine B (RhB) reaction. Upon further manipulating the particle sizes and alloy compositions, this hybrid Au-Cu alloy NPs deliver two key tunabilities of both of their $d \rightarrow sp$ interband and plasmonic intraband transitions: Firstly, Au has a stronger plasmonic responses (Higher on optical extinction coefficient and cross-section) than Cu while Cu has a wider interband-dominant window than Au (2.1 eV for Cu vs. 2.4 eV for Au as threshold energy)[13-16]. This difference in their optical spectral overlap serves as the main design principle of the bimetallic system; Secondly, Au and Cu has different band structures and Fermi level (4.5 eV for Cu vs. 5.1 eV for Au), yet their hot carrier generation distribution exhibits similar pattern as the generated hot holes are more kinetic than the hot electrons[7, 17]. Nonetheless, it can be foreseen that the hot electrons are becoming more energetic upon incorporating more Cu contents because Cu has a Fermi level with higher energy than Au. In addition to these tunabilities on optical and electronical properties, chemically monometallic Cu is prone to surface oxidation, exerting challenges on liquid-phase experiments. Au-Cu alloys, however, are known for their chemical robustness, synthetic simplicity and delicate compositional control due to their excellent miscibility arising from much similar physicochemical properties[15, 18-21]. To better interpret the origins and photocatalytic behaviors of photoinduced charge carriers, Mie scattering theory[22] was adopted as the simulation method to compute coefficients of extinction, scattering, and absorption of monometallic Au and Cu nanospheres with various particle sizes. Our synthesized Au-Cu alloy NPs with various particle sizes and alloy stoichiometries were also complemented with Mie scattering

theory-calculated optical spectra, coefficients and cross-sections that are contributed by either one of the optical components (extinction, absorption, or scattering).

2.2 Results and Discussion

In Figure 2.1A, we illustrated the energy distribution of both interband and plasmonic intraband transitions of monometallic Au and Cu. It is believed that these two metals present analogous energy profiles[17]: Upon optical excitation, the $5d \rightarrow 6sp$ of Au and $3d \rightarrow 4sp$ of Cu interband transitions both leave a hot electron close to the Fermi level and a hot hole in the filled valence d-band farther down the Fermi level, whereas their plasmonic intraband generates a nonthermal Fermi-Dirac distribution of unbonded hot electrons above the Fermi level and hot holes below the Fermi level after the excited LSPR energy nonradiatively decays. However, it is noted that Cu has a higher Fermi level than Au, presumably leading to produced hot electrons gaining momentous kinetic energies when more Cu atoms are being alloyed with Au. The main difference lies on the intrinsic dielectric properties of monometallic Au and Cu: The wavelength-dependent real part (ε') and imaginary part (ε'') of dielectric functions of Au and Cu[23]. The Drude model renders the real part of dielectric functions to be the polarization responses and the imaginary part to be the optical losses of a conducting material to the incident lights[24-25]. At nanoscale, it can be assumed that dielectric functions are independent of particle sizes and shapes of NPs[19, 26]. The change of slope in ε' for Au and Cu can be deemed as the onsets for the $d \rightarrow sp$ interband transition and helps determine the threshold energy to be about 2.4 eV and 2.1 eV, respectively. ε'' is responsible for damping or broadening of plasmonic peaks. Seemingly, Cu suffers more optical losses than Au. This optical

property consequently dictates the extinction spectra features of Au and Cu. Due to the spectral background of wider interband window of Cu, it is obvious that for nanospheres below 100 nm in diameter, the LSPR peaks of Cu are smaller in intensity, while for nanospheres larger than 100 nm, LSPR peaks show comparable intensity and broadness for both Cu and Au. Additionally, the quadrupole and octupole of LSPR peaks of Cu require larger diameter size to become visible, which is also the direct impact of strong interband transition of Cu in the spectral background.

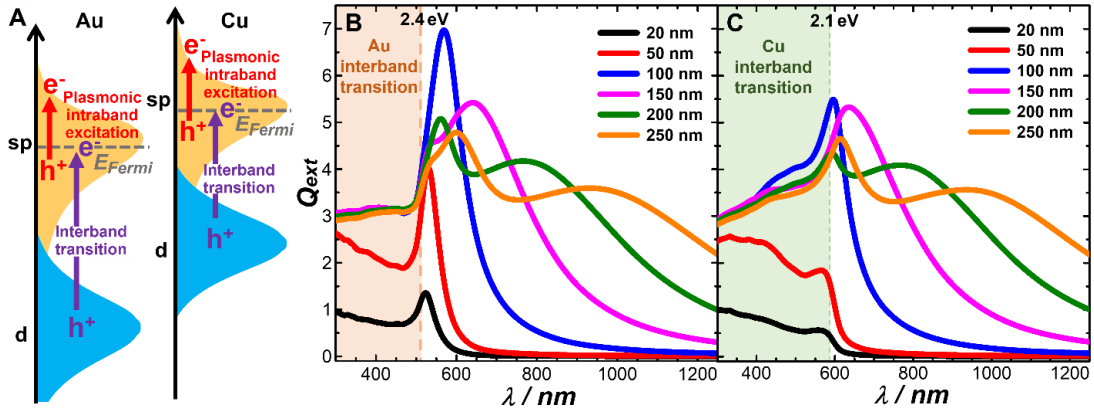

Figure 2.1. (A) Schematic illustrations of Interband transitions and plasmonic intraband excitation of monometallic gold and copper. (B) Q_{ext} of monometallic gold and (C) copper nanospheres with a particle size of 20 nm, 50 nm, 100 nm, 150 nm, 200 nm, 250 nm in diameter. Interband transition-dominant windows were shown in the shaded regions.

It is clear that when the NPs are below 100 nm and above 100 nm in diameter, particle size dependence of their spectral patterns is different. Therefore, in order to better elucidate the particle size dependence of both the spectral patterns and photocatalytic activity, it is of vital importance to ensure the size tunability of our synthesized Au-Cu alloy and Au NPs to span from around 50 nm to 200 nm in diameter. Table 1 summarized all the synthesized Au-Cu alloy and Au NPs that were used in this work, together with

their alloy stoichiometry obtained using powder X-ray diffraction (PXRD) patterns or energy-dispersive spectroscopy (EDS), particle sizes determined using their transmission electron microscopy (TEM) images, and sample labelling information. We synthesized one set of particle size-varying Au NPs (Au-i, Au-ii, and Au-iii) and two sets of Au-Cu alloy NPs, from which one set of Au-Cu alloy NPs (AuCu-i, AuCu-ii, AuCu-iii, and AuCu-iv) have fixed alloy stoichiometry at about 4.3 of Cu-to-Au atomic ratio but different particle sizes, while another set (AuCu-iii, AuCu-v, AuCu-vi, and AuCu-vii) have fixed particle sizes at about 141 nm in diameter but different alloy stoichiometry.

Table 2.1. Summary table of various Au-Cu alloy and Au NPs.

	Cu/Au atomic ratios		**Particle size / nm**	**Sample label**
	PXRD	EDS		
Au-i	0	0	58 ± 7.1	Au-58
Au-ii	0	0	139 ± 11.5	Au-139
Au-iii	0	0	180 ± 12.6	Au-180
AuCu-i	4.5	4.3 ± 0.34	58 ± 5.6	$AuCu_{4.3}$-58
AuCu-ii	4.3	4.4 ± 0.37	115 ± 10.8	$AuCu_{4.4}$-115

AuCu-iii	4.5	4.2 ± 0.32	142 ± 12.0	$AuCu_{4.2}$-142
AuCu-iv	4.7	4.5 ± 0.33	178 ± 14.6	$AuCu_{4.5}$-178
AuCu-v	2.0	2.2 ± 0.16	138 ± 10.7	$AuCu_{2.2}$-138
AuCu-vi	0.72	0.83 ± 0.064	140 ± 11.2	$AuCu_{0.83}$-140
AuCu-vii	0.23	0.27 ± 0.028	141 ± 12.6	$AuCu_{0.27}$-141

In Figure 2.2, the particle size-varying Au-i, Au-ii, and Au-iii NPs were characterized to be monometallic gold and adopt fcc crystal structure (JCPDS 04-0784). Their particle sizes were determined using their TEM images (Figure 2.2B-D) to be 58 nm, 139 nm, and 180 nm, according to size distribution histograms in Figure 2.2E.

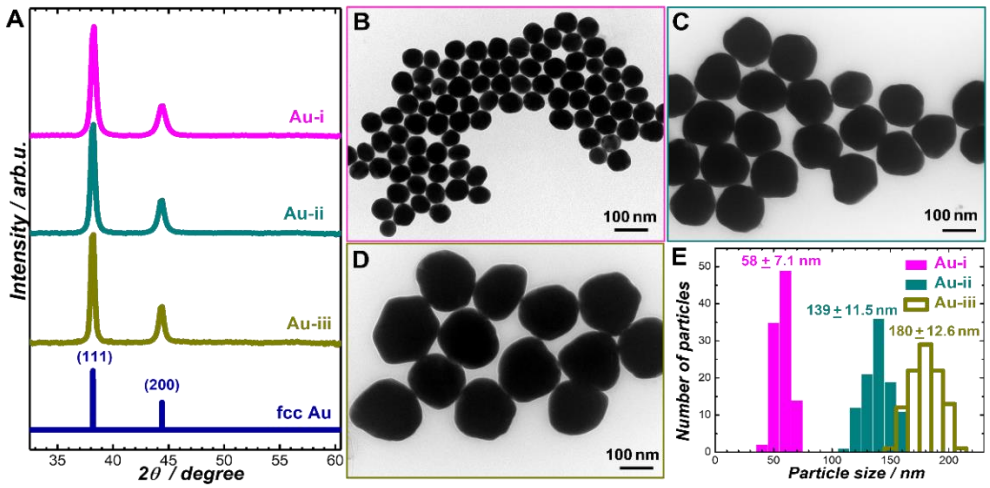

Figure 2.2. (A) PXRD patterns of metallics gold NPs: Au-i, Au-ii, and Au-iii. TEM images of (B) Au-i, (C) Au-ii, and (D) Au-iii. (E) Particle size distribution.

In Figure 2.3, particle size-varying AuCu-i, AuCu-ii, AuCu-iii, and AuCu-iv NPs were designed and confirmed to be Cu-rich Au-Cu alloy NPs. According to Vegard's law[27], the lattice constant of an alloy material (solid solution) is in linear relation with lattice constants of its constituent metals (solute and solvent). An empirical equation can adequately describe the composition-dependent lattice constant of the alloy NPs:

$$a = (1 - x)a_1 + xa_2 \qquad (1),$$

where a is the lattice constant of alloy, x is the composition of one of the constituent metals, a_1 is the lattice constant of one of the constituent metals, and a_2 is the lattice constant of another constituent metals. Au-Cu alloy is believed to show very little deviation to Vegard's law[28]. The particle sizes of these Au-Cu alloy NPs were determined using their TEM images (Figure 2.3B-E) to be 58 nm, 115 nm, 142 nm, and 178 nm, according to size distribution histograms in Figure 2.3F.

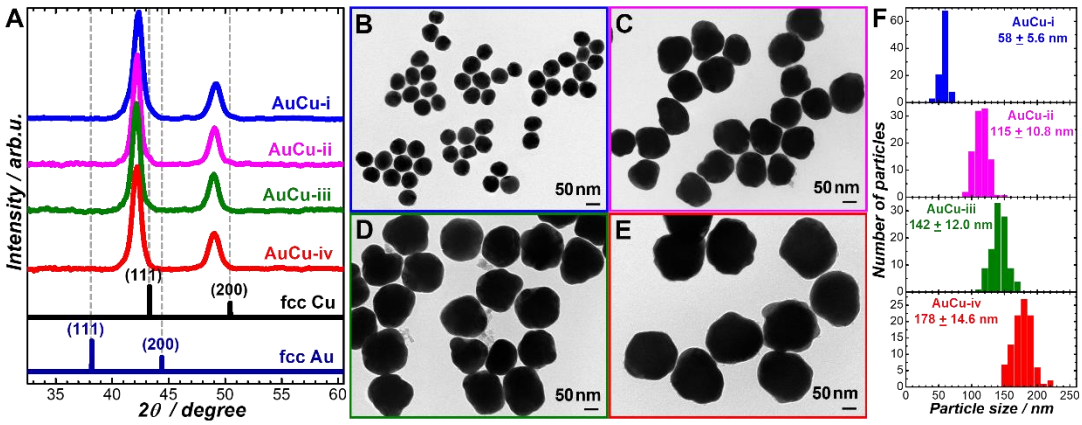

Figure 2.3. (A) PXRD patterns of particle size-varying alloy Au-Cu NPs: AuCu-i, AuCu-ii, AuCu-iii, and AuCu-iv. TEM images of (B) AuCu-i, (C) AuCu-ii, (D) AuCu-iii, and (E) AuCu-iv. (F) Particle size distribution.

In Figure 2.4A, alloy stoichiometry-varying AuCu-iii, AuCu-v, AuCu-vi, and AuCu-vii NPs were characterized to show different alloy stoichiometry in decreasing

order of Cu content. The particle sizes of these Au-Cu alloy NPs were determined using their TEM images (Figure 2.4B-E) to be 142 nm, 138 nm, 140 nm, and 141 nm, according to size distribution histograms Figure 2.4F.

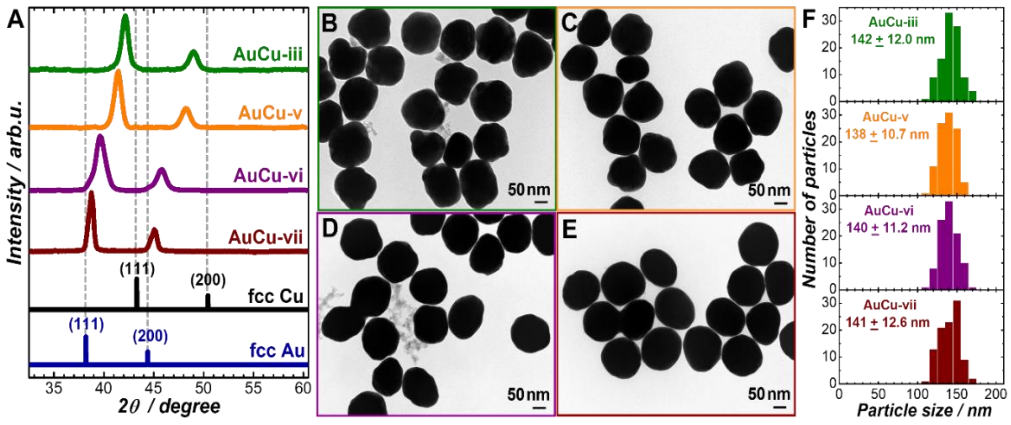

Figure 2.4. (A) PXRD patterns of alloy composition-varying alloy Au-Cu NPs: AuCu-iii, AuCu-v, AuCu-vi, and AuCu-vii. TEM images of (B) AuCu-iii, (C) AuCu-v, (D) AuCu-vi, and (E) AuCu-vii. (F) Particle size distribution.

We have chosen four representative NPs (Au-i labeled as Au-58, AuCu-i labeled as $AuCu_{4.3}$-58, Au-ii labeled as Au-180, and AuCu-iv labeled as $AuCu_{4.5}$-178) to perform photocatalytic mineralization reaction of industrial dye, RhB, with the wavelength of excitation sources (λ_{ex}) across the visible spectrum: Namely, 445 nm, 520 nm, 638 nm, 785 nm, and 980 nm continuous-wave lasers were used. The reaction mechanism of photocatalytic degradation of RhB was schematically illustrated in Figure 2.5A. This reaction is believed to be driven by both the photoinduced hot electrons and hot holes of the Au or Au-Cu alloy NPs.

Both interband transition-produced and plasmonic intraband transition-produced hot electrons can intercept the excessively added H_2O_2 to form ·OH as the reactive oxygen species (ROS) that directly participates in the reaction, as shown in equation (2).

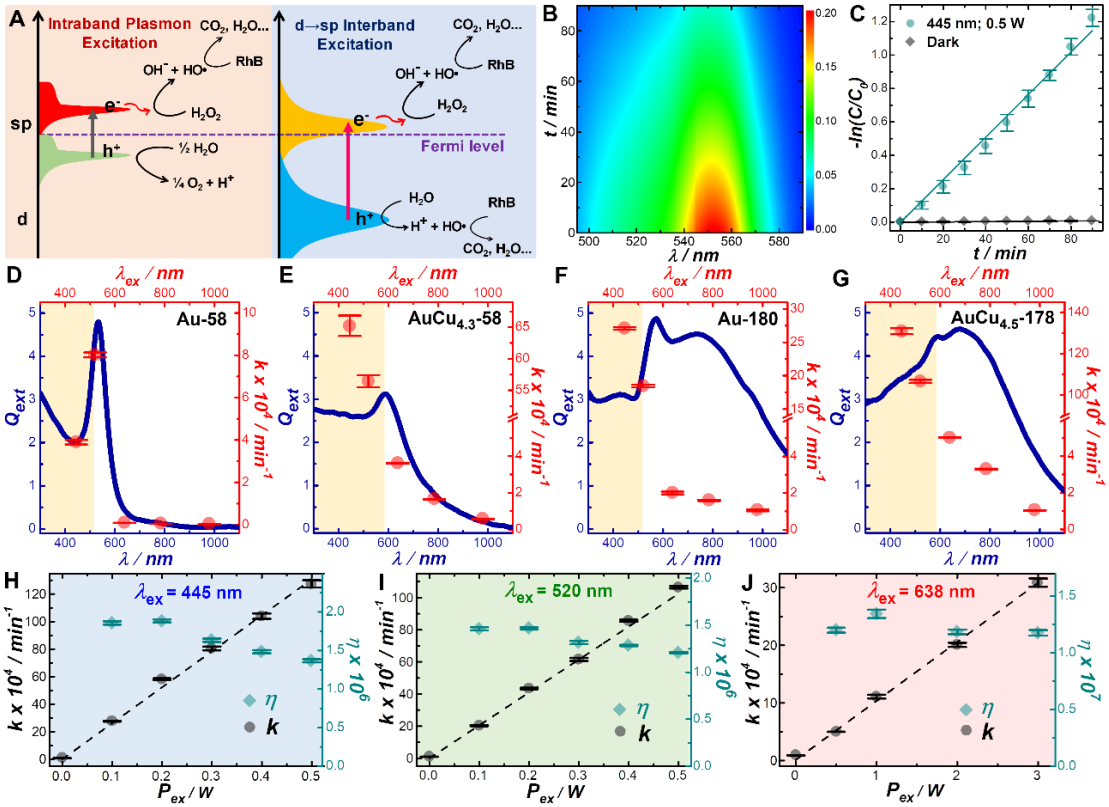

Figure 2.5. (A) Schematic illustrations of the reaction mechanism of photocatalytic decolorization of RhB via plasmonic intraband excitation and $d \rightarrow sp$ interband transition respectively. Temporal evolution of (B) UV-vis absorption of decolorization of RhB and (C) its $-\ln(C/C_0)$ during photocatalytic reaction, catalyzed by $AuCu_{4.5}$-178 at the λ_{ex} of 445 nm and the P_{ex} of 0.5 W. $-\ln (C/C_0)$ of dark reaction was shown for comparison. Action spectra comprising of the Q_{ext} and k of (D) Au-58, (E) $AuCu_{4.3}$-58, (F) Au-180, and (G) $AuCu_{4.5}$-178 NPs at λ_{ex}s of 445 nm, 520 nm, 638 nm, 785 nm, and 980 nm. P_{ex} dependence of k and η at the λ_{ex} of (H) 445 nm, (I) 520 nm, and (J) 638 nm.

For hot holes, however, the interband transition-produced hot holes are able to intercept water molecule to produce ·OH as the ROS supply, while the plasmonic intraband transition-produced hot holes are not kinetic enough to activate it and instead are consumed by the O_2 evolution reaction (Redox potentials of $\cdot OH/H_2O$ and O_2/H_2O are -7.5 eV and -5.7 eV vs. vacuum).

$$-\frac{d[RhB]}{dt} = k'[RhB][\cdot OH] \qquad (2),$$

where k' is the reaction constant. Due to the excessiveness of ·OH, this reaction can be simplified to be a pseudo first-order decolorization reaction, of which UV-vis spectrum can be straightforwardly and effectively used to monitor and solve the reaction kinetics:

$$\ln\left(\frac{C}{C_0}\right) = \ln\left(\frac{I}{I_0}\right) = -kt \qquad (3),$$

where k is the apparent reaction constant, C_0 is the initial concentration of RhB, I_0 is the intensity of absorption peaks at 553 nm of RhB, C is the reaction-time concentration of RhB, and I is the intensity of absorption peaks at 553 nm of RhB. Concentration and intensity of absorption peaks are related by the Beer-Lambert law.

In Figure 2.5B, decolorization of RhB was shown, catalyzed by $AuCu_{4.5}$-178 with the λ_{ex} of 445 nm and excitation power (P_{ex}) of 0.5 Watts. The temporal evolution of $-\ln\left(\frac{C}{C_0}\right)$ of this reaction was shown in Figure 2.5C, along with that of a dark reaction without any external laser illuminations. We later constructed four action spectra of the four representative Au-Cu alloy and Au NPs in photocatalytic action, comprising of their Q_{ext} and k at their respective λ_{ex}s (Figure 2.5D-G). For Au-58, as seen in Figure 2.5D, k matches well with its extinction spectrum. At the λ_{ex} of 520 nm, photocatalytic performance is the best among all five λ_{ex}s, because it is on resonance with its LSPR peak. When alloying with Cu, nonetheless, Au-58 becomes $AuCu_{4.3}$-58 with a Cu-to-Au atomic ratio of 4.3 and subsequently undergoes a change in its extinction pattern and energy distribution of photoinduced charge carriers. Evidently, as indicated in Figure 2.5E, LSPR peak of $AuCu_{4.3}$-58 was suppressed, due to the expanding interband

transition region in the background upon incorporation of Cu. It manifests the best photocatalytic performance at λ_{ex} of 445 nm, which is well into the interband transition region. At λ_{ex} of 520 nm, interband transition is as well triggered, but suffers the comparison of photocatalytic performance to λ_{ex} of 445 nm, due to having less incident photonic energy. Noticeably, for λ_{ex} of 638 nm, 785 nm, and 980 nm, plasmonic intraband transition-produced charge carriers are slightly more photocatalytic active than that of Au upon alloying with Cu as well. At a larger particle size regime, when Au-180 was put in photocatalytic action, it can be observed that its best photocatalytic performance still sits at λ_{ex} of 445 nm, while the second best sits at λ_{ex} of 520 nm. In comparison to the photocatalytic performance of Au-58, this is reasonable because (1) interband transition is enhanced upon increasing the particle size; (2) at the λ_{ex} of 520 nm, the doorstep of interband transition window of Au, plasmonic intraband transition becomes dominant and is known not to produce as photocatalytic active charge carriers as interband transition do; (3) at the λ_{ex} of 520 nm, photocatalytic performance is still better than that at λ_{ex} of 638 nm, 785 nm, and 980 nm as absorption responses are very limited at these wavelengths. For $AuCu_{4.5}$-178, the incorporated Cu content predictably suppresses the quadrupole of LSPR peak and boosts the photocatalytic performance across all five λ_{ex}s, especially at the λ_{ex} of 445 nm and 520 nm (About five-fold enhancement compared to two-fold enhancement at the λ_{ex} of 638 nm, 785 nm, and 980 nm). From these results, it is consequently definitive that interband-produced charge carriers are more photocatalytic active than the plasmonic intraband-produced charge carriers, and alloying Au with Cu lead to photoinduced hot electrons becoming more energetic and therefore enhanced photocatalytic activity.

To better express the effectiveness of photoinduced charge carriers in photocatalytic action, we calculated apparent quantum efficiency, η:

$$\eta = \frac{h \times c \times (C_0 - C_{3600s}) \times V \times N_A}{P_{ex} \times \lambda_{ex} \times 3600s} \quad (4),$$

where h is the Planck's constant (6.626×10^{-34} m^2 kg s^{-1}), c is the speed of light (3.0×10^{-8} m s^{-1}), C_0 is the initial concentration of RhB (2×10^{-6} M), C_{3600} is the concentration of RhB after 60 minutes of photoreactions, V is the volume of the solution (2.0×10^{-3} L), N_A is the Avogadro's number (6.022×10^{23} mol^{-1}). In Figure 2.5H-J, P_{ex} dependence of η and k were demonstrated at the λ_{ex} of 445 nm, 520 nm, and 638 nm. Perceptibly, k obeys a linear relationship with respect to increasing P_{ex} below 0.5 Watts at the λ_{ex} of 445 nm and 520 nm and increasing P_{ex} below 3.0 Watts at the λ_{ex} of 638 nm. η, in contrast, appears to show a slight decreasing trend at the λ_{ex} of 445 nm and 520 nm, but is unchanged at the λ_{ex} of 638 nm. This can be ascribed to the intrinsic differences of interband transition-produced orbital-bonded electron-hole pairs and plasmonic intraband-produced free hot carriers: the former needs to occupy an excited state at the sp band, which is subject to population plateau, while the latter is highly unbonded and unlocalized. Therefore, at the λ_{ex} of 445 nm and 520 nm, increasing photonic supply upon increasing P_{ex} does not necessarily translate into proportional photocatalytic active charge carriers, hence the decreasing trend of η. At the same time, unlocalized plasmonic hot carriers, at the λ_{ex} of 638 nm, can still proportionally contribute to photocatalytic action upon absorbing more incoming photons, hence largely unaffected η.

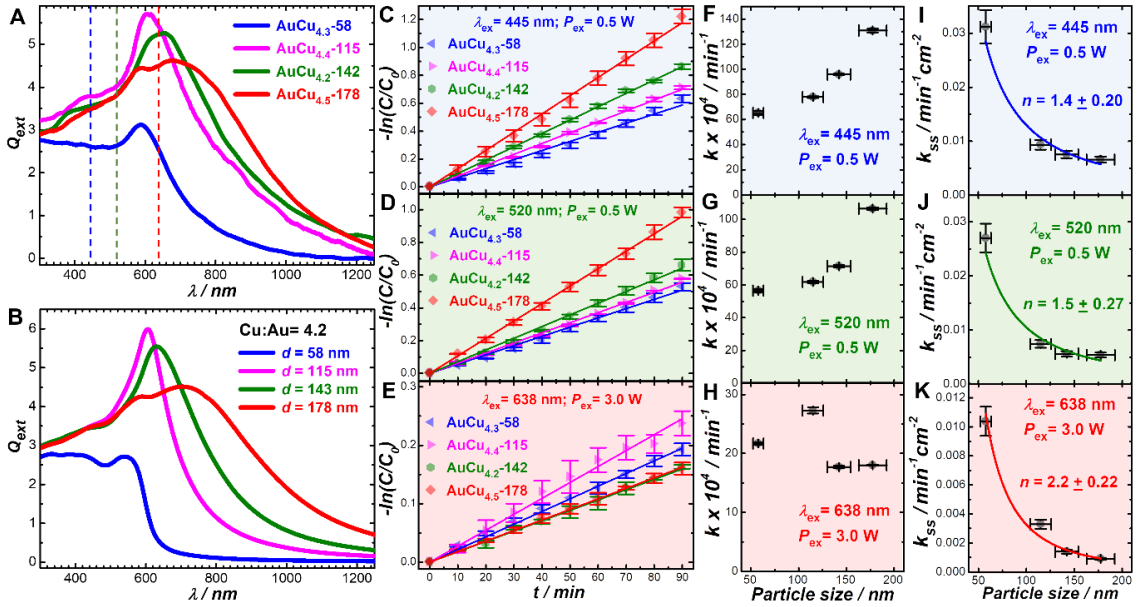

Figure 2.6. (A) The experimental and (B) theoretically calculated Q_{ext} of the particle size-varying Au-Cu alloy NPs: AuCu$_{4.3}$-58, AuCu$_{4.4}$-115, AuCu$_{4.3}$-142, and AuCu$_{4.5}$-178 alloy NPs. Dashed lines in (A) represents λ_{ex}s of 445 nm, 520 nm, and 638 nm. Temporal evolution of -ln(C/C$_0$) of RhB during photocatalytic reaction at the λ_{ex} of (C) 445 nm with a P_{ex} of 0.5 Watts, (D) 520 nm with a P_{ex} of 0.5 Watts, and (E) 638 nm with a P_{ex} of 3.0 Watts. Particle size dependence of k at the λ_{ex} of (F) 445 nm with a P_{ex} of 0.5 Watts, (G) 520 nm with a P_{ex} of 0.5 Watts, and (H) 638 nm with a P_{ex} of 3.0 Watts. Particle size dependence of k_{ss} at the λ_{ex} of (I) 445 nm with a P_{ex} of 0.5 Watts, (J) 520 nm with a P_{ex} of 0.5 Watts, and (K) 638 nm with a P_{ex} of 3.0 Watts.

To examine the particle size dependence of the photocatalytic activity of Au-Cu alloy NPs, one set of particle size-varying Au-Cu alloy NPs (AuCu$_{4.3}$-58, AuCu$_{4.4}$-115, AuCu$_{4.2}$-142, and AuCu$_{4.5}$-178) were put in photocatalytic action, at λ_{ex}s of 445 nm, 520 nm, and 638 nm. In Figure 2.6A, Q_{ext} of these Au-Cu alloy NPs was shown, which agrees well with the Mie scattering theory-calculated Q_{ext}, shown in Figure 2.6B. Temporal evolutions of $-\ln\left(\frac{C}{C_0}\right)$ of RhB at λ_{ex}s of 445 nm and 520 nm, as indicated in Figure 2.6C and 2.6D, reveal that k increases with the increase of particle size of NPs while alloy composition remains the same. This suggests that for interband transition, more lattices contribute to more production of charge carriers, thus better apparent

photocatalytic activity (Figure 2.6F and 2.6G). At the λ_{ex} of 638 nm, however, temporal evolution of $-\ln\left(\frac{C}{C_0}\right)$ of RhB does not necessarily follow this pattern, as $AuCu_{4.4}$-115 exhibits the best apparent photocatalytic activity among this set of Au-Cu alloy NPs (Figure 2.6E). Particle size dependence of k at the λ_{ex} of 638 nm, as shown in Figure 3H, indicates a 'volcano'-shaped relationship. This is likely due to stronger absorption capability of $AuCu_{4.4}$-115 at the λ_{ex} of 638 nm. However, it is worth noting that $AuCu_{4.3}$-58 has the second best k, even with lowest absorption coefficient and cross section, at the λ_{ex} of 638 nm. To better consider the size-dependence photocatalytic activity of these charge carriers, we calculated surface-specific reaction constant, k_{ss}, to take into account the catalytically active surface area of these Au-Cu alloy NPs:

$$k_{ss} = A\frac{1}{r^n} \qquad (5),$$

where A is the pre-factor coefficient, r is the radius of the NPs, and n is the exponential factor. As exhibited in Figure 2.6I and 2.6J, k_{ss} demonstrates a decreasing trend with respect to increasing particle size of Au-Cu alloy NPs at λ_{ex}s of 445 nm and 520 nm. This is more thorough evaluation on the size dependence of photocatalytic activity because, with larger particle sizes, not only more lattices can be harnessed for light absorption and subsequent charge carriers generation upon interband transition excitation, but also longer diffusion length of charge carriers from the bulk to the surface is required. Consequently, NPs with larger particle size, does not necessarily lead to enhanced photocatalytic activity for interband transition-produced charge carriers. Similarly, as shown in Figure 2.6K, when plasmonic intraband transition is excited at the λ_{ex} of 638 nm, $AuCu_{4.3}$-58 exhibits the best k_{ss} owing to the shortest diffusion length of

charge carriers, despite comparatively insignificant absorption coefficient and cross section areas.

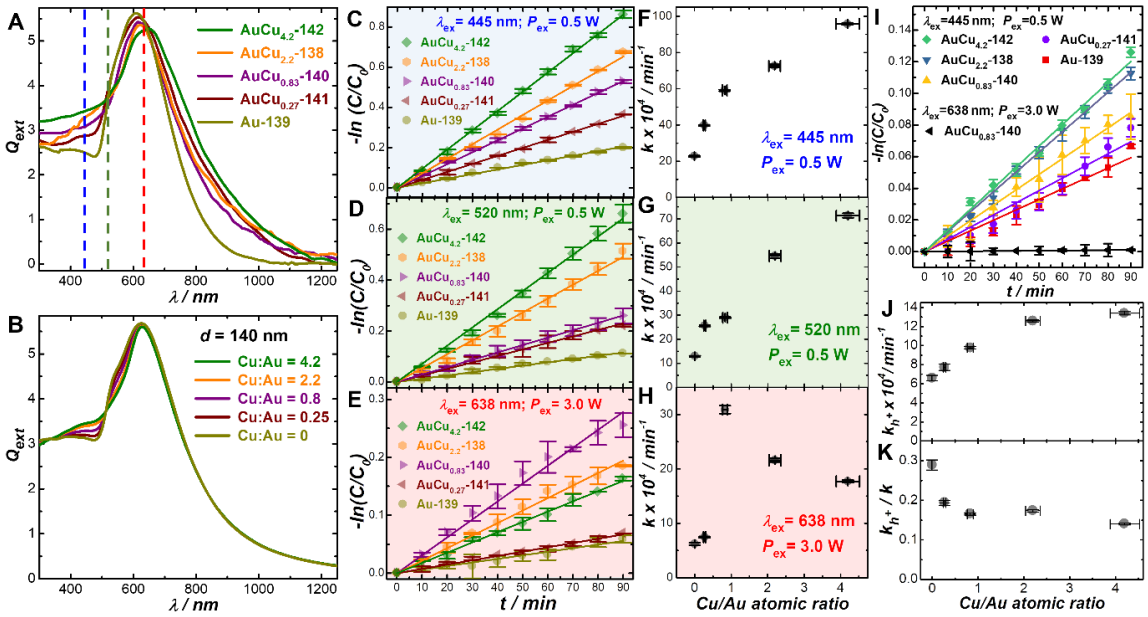

Figure 2.7. (A) The experimental and (B) theoretically calculated Q_{ext}s of the alloy composition-varying Au-Cu alloy and Au NPs: $AuCu_{4.2}$-142, $AuCu_{2.2}$-138, $AuCu_{0.83}$-140, $AuCu_{0.27}$-141 alloy NPs and Au-139 NPs. Dashed lines in (A) represents λ_{ex}s of 445 nm, 520 nm, and 638 nm. Temporal evolution of -ln(C/C$_0$) of RhB during photocatalytic reaction at the λ_{ex} of (C) 445 nm with a P_{ex} of 0.5 Watts, (D) 520 nm with a P_{ex} of 0.5 Watts, and (E) 638 nm with a P_{ex} of 3.0 Watts. Alloy composition dependence of k at the λ_{ex} of (F) 445 nm with a P_{ex} of 0.5 Watts, (G) 520 nm with a P_{ex} of 0.5 Watts, and (H) 638 nm with a P_{ex} of 3.0 Watts. (I) Temporal evolution of –ln(C/C$_0$) of RhB during hole-driven photocatalytic reaction at the λ_{ex} of 445 nm with a P_{ex} of 0.5 Watts, or at λ_{ex} of 638 nm with a P_{ex} of 3.0 Watts. Alloy composition dependence of (J) k_{h^+} and (K) k_{h^+}/k.

Alloy composition dependence of photocatalytic activity of the Au-Cu alloy and Au NPs photocatalysts was next studied. In Figure 2.7A, Q_{ext} of a set of alloy stoichiometry-varying Au-Cu alloy and Au NPs ($AuCu_{4.2}$-142, $AuCu_{2.2}$-138, $AuCu_{0.83}$-140, $AuCu_{0.27}$-141, and Au-139) was shown. The calculated Q_{ext}, in Figure 2.7B, shows good agreement with experimentally obtained Q_{ext}. Temporal evolutions of $-\ln\left(\frac{C}{C_0}\right)$ of

RhB at λ_{ex}s of 445 nm and 520 nm in Figure 2.7C and 2.7D show that k increases with more Cu contents being alloyed while the particle size of Au-Cu alloy NPs is unchanged, despite a minor weakening of absorption coefficients at λ_{ex}s of 445 nm and 520 nm. This can be ascribed to the interband transition-produced hot electrons gathering more energies as $4sp$ band of Cu is more energetic than $6sp$ band of Au, as the Cu-to-Au atomic ratio dependence of k has suggested in Figure 2.7F and 2.7G. When the plasmonic intraband transition is excited at the λ_{ex} of 638 nm, temporal evolution of $-\ln\left(\frac{C}{C_0}\right)$ of RhB, as shown in Figure 2.7E, shows that $AuCu_{0.83}$-140 exhibits the best apparent photocatalytic performance. All Together, in Figure 2.7H, the Cu-to-Au atomic ratio dependence of k implies another 'volcano'-shaped relationship. To better understand how the photoinduced charge carriers of Au-Cu alloy NPs, upon alloying with more Cu atoms, behave at greater depth, we designed photothermal measurements to explore the impact of an alternative light-to-thermal pathway other than photocatalysis. We have examined the involvement of hot holes to the photocatalytic activity. In the absence of H_2O_2, photoinduced hot electrons were not able to generate ROS, but instead participated in hydrogen evolution reaction. Interband transition-produced hot holes, however, are still kinetically energetic enough to create ·OH as the ROS to drive the photocatalytic mineralization of RhB. As shown in temporal evolution of $-\ln\left(\frac{C}{C_0}\right)$ of RhB in Figure 2.7I, alloy composition dependence of hot-hole driven photocatalytic activity was interrogated as the incoming Cu contents contribute to better apparent photocatalytic activity. k_{h^+}, reaction constant of hot-hole driven photocatalysis, also shows increasing trend with respect to increasing Cu-to-Au atomic ratio. However, when

taking into account the overall photocatalytic activity, $\frac{k_{h^+}}{k}$ illustrates a different trending pattern in Figure 2.7K, as the more Cu contents tend to lessen the hot-hole driven photocatalytic activity. This is largely expected, because with more incoming Cu contents, hot electrons become more energetic and more reducing, hot holes are as well more reducing, but less oxidizing and therefore less energetic. It is worth noting that at the λ_{ex} of 638 nm, hot hole driven photocatalysis is essentially inhibited, as implied in the temporal evolution of $-\ln\left(\frac{C}{C_0}\right)$ of RhB, catalyzed by $AuCu_{0.83}$-140 Au-Cu alloy NPs, in Figure 2.7I.

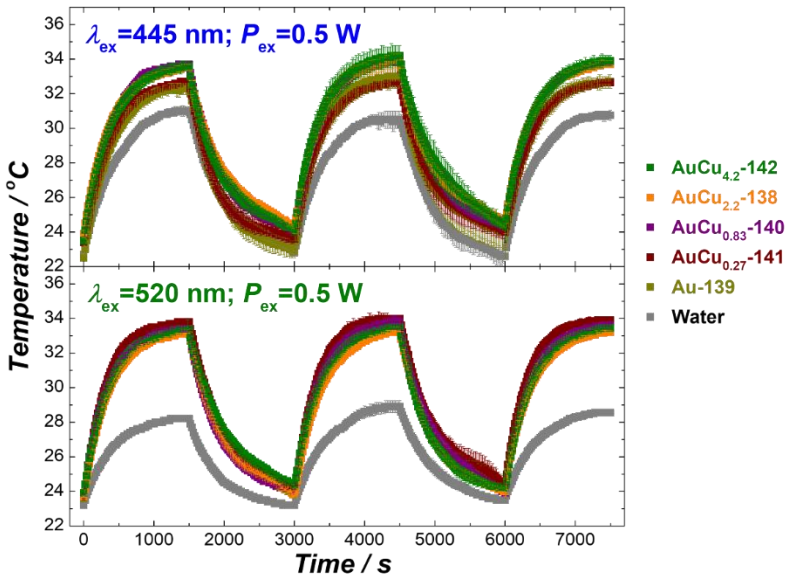

Figure 2.8. Temperature evolution of colloidal alloy composition-varying Au-Cu alloy and Au NPs ($AuCu_{4.2}$-142, $AuCu_{2.2}$-138, $AuCu_{0.83}$-140, $AuCu_{0.27}$-141 alloy NPs and Au-139 NPs) over three cycles of 445 nm and 520 nm continuous-wave laser illumination and natural cooling with an P_{ex} of 0.5 Watts.

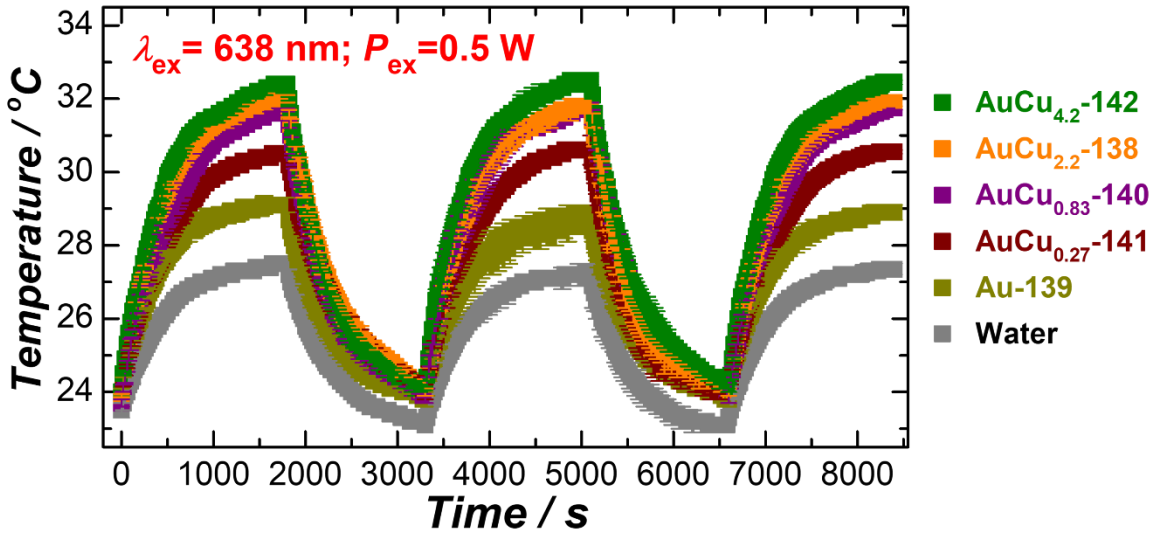

Figure 2.9. Temperature evolution of colloidal alloy composition-varying Au-Cu alloy and Au NPs ($AuCu_{4.2}$-142, $AuCu_{2.2}$-138, $AuCu_{0.83}$-140, $AuCu_{0.27}$-141 alloy NPs and Au-139 NPs) over three cycles of 638 nm continuous-wave laser illumination and natural cooling with an P_{ex} of 0.5 Watts.

Recorded in Figure 2.8 and 2.9 are the temperature evolutions of 2.0 mL water in quartz cuvette contained with the set of alloy stoichiometry-varying Au-Cu alloy and Au NPs in colloidal suspension form, upon switching on-and-off of laser illumination at λ_{ex}s of 445 nm, 520 nm, and 638 nm. Cooling cycles, initiated when lasers were switched off, were taken for photothermal efficiency (ϕ) calculations:

$$\phi = \frac{hA(T_{max}-T_{amb})-Q_0}{P_{ex}(1-10^{-A_\lambda})} \qquad (6),$$

where h is the heat transfer coefficient, A is the cross-sectional surface area of thermal convection of the solution to the air (1.0 cm^2), T_{max} is the maximum temperature upon elevation, T_{amb} is the ambient temperature before elevation, Q_0 is the photoinduced heat by only water, which is measured and calculated separately, and A_λ is the absorption

of NPs at the wavelength of laser excitation. It is worth mentioning that A_λ is adjusted based on the Q_{ext} of the set of Au-Cu alloy and Au NPs and extinction-to-absorption ratio of coefficients to only consider absorption component and eliminate the impact of scattering. As shown in Figure 2.8, at λ_{ex}s of 445 nm and 520 nm, temperature evolutions are nearly comparable for Au-Cu alloy NPs with different Cu-to-Au stoichiometry. In stark contrast, at the λ_{ex} of 638 nm, Au-Cu alloy NPs seemingly better elevate temperatures with more Cu contents, as the most Cu-rich $AuCu_{4.2}$-142 NPs raised the temperature for about 9 degrees while monometallic Au-139 NPs brought up the temperature for roughly 5 degrees, as shown in Figure 2.9. For other Au-Cu alloy NPs, temperature elevation is shrinking with decreasing Cu-to-Au stoichiometry.

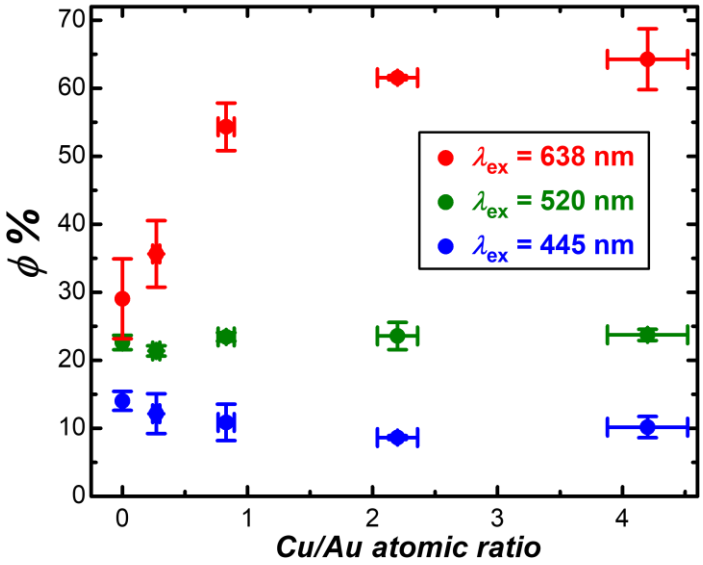

Figure 2.10. Alloy composition dependence of ϕ at the excitation of 445 nm, 520 nm, and 638 nm lasers respectively.

ϕs were subsequently calculated and tabulated in Figure 2.10. Noticeably, at λ_{ex}s of 445 nm and 520 nm, ϕs remain unchanged for all Cu-to-Au stoichiometry. Whereas, at the λ_{ex} of 638 nm, ϕs increase as Cu-to-Au atomic ratio increases and is better than ϕs

at λ_{ex}s of 445 nm and 520 nm, at each individual Cu-to-Au atomic ratio. To put this photothermal analysis into perspective with the photocatalytic performance, it can be concluded that plasmonic intraband transition-produced charge carriers, as compared to the interband transition-produced ones, are more efficient at photothermal than at photocatalysis, in which these two processes are essentially competing with one another. This could explain the 'volcano'-shape relationship of k and Cu-to-Au atomic ratio of Au-Cu alloy NPs, since the more energetic charge carriers becomes, the likelier they will take the preferred photothermal pathway rather than the unpreferred photocatalytic activity, causing a downturn trend of its alloy composition dependence of k.

2.3 Conclusion

In this work, we have emphasized on unraveling the spectral patterns and photocatalytic behaviors of an atomically well-mixed Au-Cu alloy nanomaterial system that are intricated by their bimodal optical transitions: the $d \rightarrow sp$ interband and plasmonic intraband transitions. We have shown that the interband transition-produced charge carriers are generally more photocatalytically active than the plasmonic intraband transition-produced charge carriers. However, they both become even more active upon alloying with more Cu contents, due to a higher energy of electronic bands of Cu. These findings aim to provide useful insights on photocatalytic mechanism and material designs for efficient photocatalysts.

2.4 Experiments and methods

Chemicals and Materials. Copper nitrate hydrate ($Cu(NO_3)_2 \cdot 3H_2O$), chloroauric acid ($HAuCl_4 \cdot 4H_2O$), ethylene glycol (EG), polyvinylpyrrolidone (PVP, average

molecular weight of 58,000), tetraethylene glycol (TEG), and rhodamine B (RhB) were purchased from Alfa Aesar. Hydrogen peroxide (30% by volume, 9.8 M) was purchased from Ward's science. Trizma base (TB) and hydrazine solution ($N_2H_4 \cdot 3H_2O$, 35 wt%) were purchased from Sigma-Aldrich. Trisodium citrate dihydrate ($Na_3C_6H_5O_7 \cdot 2H_2O$) and sodium hydroxide (NaOH) were purchased from Fisher Scientific. Five continuous-wave diode lasers were purchased from Lasever Inc. with emission wavelength at 445 nm (model no. LSR445SD), 520 nm (model no. LSR520CPD), 638 nm (model no. LSR638CP8), 785 nm (model no. LSR785NL), and 980 nm (model no. LSR980NL). All reagents received were used without further purification. Ultrapure Milli-Q water (18.2 Ω) was used for all experiments.

Characterizations. The transmission electron microscopy (TEM) images were obtained using a Hitachi H-7800 transmission electron microscope, operated at an accelerating voltage of 120 kV. Samples for TEM measurement were dispersed in ethanol and drop-dried on 300 mesh carbon-coated Cu grids (Electron Microscopy Science Inc.). Energy dispersive spectroscopy (EDS) measurements were conducted using a Zeiss Ultraplus thermal field emission scanning electron microscope (SEM). An EDS unit attached to the microscope was used to quantify the Au and Cu stoichiometries in the samples. Atomic ratios were quantified based on the relative area of the Au Mα, Cu Lα peaks in the EDS spectra. Samples for EDS measurements were dispersed in ethanol and drop-dried on silicon wafers. Powder X-ray diffraction (PXRD) patterns were collected on a SAXSLab Ganesha at the South Carolina Collaborative (Cu Kα = 1.5405 Å). The optical extinction spectra were recorded in aqueous phase using SpectraMax M2 Multimode Microplate Readers.

Synthesis of spherical Au NPs. Spherical gold nanoparticles were synthesized using a growth method reported elsewhere[29]. Briefly, 17 nm Au seed NPs were first prepared by reducing $HAuCl_4$ with trisodium citrate in an aqueous solution. 1.5 mL of 1 wt% trisodium citrate aqueous solution was added into 48 mL boiling water under magnetic stir of 300 resolution per minute (rpm). Subsequently, 0.5 mL of 25 mM $HAuCl_4$ was injected into the solution. The reaction was kept at boiling temperature for 30 minutes. This homogeneously nucleated Au seed nanoparticle serves as the seed particles used next for seed-mediated regrowth to obtain Au NPs with increased particle sizes, upon reduction of $HAuCl_4$ with trizma base (TB). Typically, 2 mL of 0.1 M of TB was added into 45 mL boiling water under magnetic stir of 300 rpm. After 10 minutes of stirring, 1 mL of 25 mM of $HAuCl_4$ and 2 mL of the as-synthesized 17 nm-Au seed particles solution were added. The reaction solution was maintained at gentle boil for 30 minutes. The amount of 17 nm Au seed particles introduced was varied in order to obtain Au NPs with desired overall particle sizes.

Synthesis of Au-Cu alloy NPs. The atomically intermixed Au-Cu alloy NPs were synthesized following a previously published paper[30]. First, a cuprous oxide layer was deposited onto the spherical Au NP. In a 30 mL water dissolved with 2 wt% PVP, varying amount of colloidal Au NPs and $Cu(NO_3)_2$ was added in order for different shell thickness. Subsequently, 67 μL of 5.0 M NaOH and 30 μL of $N_2H_4 \cdot 3H_2O$ were added under magnetic stirring of 300 rpm. The reaction was kept under ice bath for 15 minutes. Then, the as-synthesized $Au@Cu_2O$ core@shell NPs were added into 10 mL TEG dissolved with 0.1 g of PVP to produce Au-Cu alloy NPs. The reaction solution was kept at 300 °C for 2 hr. Finally, multiple centrifugation-redispersion cycles were adopted to

rinse the glycol and PVP residues of the obtained Au-Cu alloy NPs. The alloy composition and particle size are systematically tuned by adjusting the relative dimensions of Au@Cu_2O core@shell NPs and the particle size of the core Au spherical NPs, respectively.

Photocatalytic degradation of RhB. Photocatalytic reaction of RhB was conducted using a quartz cuvette cell (1.0 cm x 1.0 cm x 4.5 cm). 2 mL of 0.001 mM RhB aqueous solution was first prepared. Au-Cu alloy or Au colloidal NPs were dispersed into the cell and kept in dark for four hours prior to laser exposure to establish adsorption-desorption equilibrium. The concentration of NPs added were ~ 1.0 x 10^9 particles/mL. When 2 mM H_2O_2 was added and circulating water bath was introduced, photocatalytic reaction was initiated upon switching on the continuous-wave lasers. The kinetic evolution of the photocatalysis was evaluated by collecting absorption spectra of RhB every 10 minutes for 90 minutes.

Apparent quantum efficiency calculation. A previously published literature work was followed[10]. As an indicator to how efficiently the photoinduced charge carriers was exploited for catalyzing RhB molecules, apparent quantum efficiency (η) was determined by the ratio of the number of RhB molecules that were photocatalyzed (n_{RhB}) to the number of laser-induced photons generated from the laser illumination ($n_{Photons}$):

$$\eta = \frac{h \times c \times (C_0 - C_{3600s}) \times V \times N_A}{P_{ex} \times \lambda_{ex} \times 3600s}$$

$$\eta = \frac{n_{RhB}}{n_{Photons}}$$

n_{RhB} and $n_{Photons}$ were further calculated following these equations:

$$n_{RhB} = (C_0 - C_{3600s}) \times V \times N_A$$

$$n_{Photons} = \frac{P_{ex} \times \lambda_{ex} \times 3600s}{h \times c}$$

where C_0 is the initial concentration of RhB (2×10^{-6} M), C_{3600} is the concentration of RhB after 60 minutes of photoreactions, V is the volume of the solution (2.0×10^{-3} L), N_A is the Avogadro's number (6.022×10^{23}), P_{ex} is the excitation power of lasers, λ_{ex} is the excitation wavelength, h is the Planck's constant, 6.626×10^{-34} m^2 kg s^{-1}, and c is the speed of light, 3.0×10^8 m s^{-1}.

Photothermal experiments and calculations. Photothermal measurement of Au-Cu alloy and Au NPs were evaluated by recoding temperature values of the colloidal NPs suspension solution with a total volume of 2.0 mL under magnetic stirring of 300 rpm upon switching on and off the laser illuminations. Heating period lasts 1500 s at λ_{ex}s of 445 nm and 520 nm, and 1800 s at the λ_{ex} of 638 nm. Cooling period lasts 1500 s.

Photothermal data was processed following a thermophysical theoretical model[31] and was previously reported by us[11]. Temperature values during cooling periods were extracted and fitted into dimensionless thermodynamic driving force (θ), dictating the thermal equilibrium of the system:

$$\theta \equiv \frac{T_{amb} - T}{T_{amb} - T_{max}}$$

where T_{amb} is the ambient temperature and T_{max} is the maximum system temperature at equilibrium. When irradiation switched off, at θ = 1, t = 0, the sample system begins to cool down exponentially (Cooling cycle follows exponential pattern better than the heating cycle due to less thermal gradients). Therefore, -ln(θ) vs. time can be linearly fitted to find thermal equilibrium time constant (τ_s), extracting first 900 seconds of cooling data:

$$\ln(\theta) = -\frac{1}{\tau_s}t$$

To further describe the energy balance of the system, energy terms of laser-induced heat generation of NCs upon electron-phonon relaxation of plasmonic energy (Q_{NPs}), laser-induced heat generation of the solvent (Q_0), and external heat dissipation of the system to surroundings (Q_e) are considered as major sources to the thermal energy introduced to the system:

$$\sum_i m_i C_{p,i} \frac{dT}{dt} = Q_{NPs} + Q_0 - Q_e$$

where m_i and $C_{p,i}$ are the mass and heat capacity of i^{th} component. Our calculation was simplified by ignoring the negligible contributions from NCs, and only considering water (Namely, $m_i = m_{water} =$ 2.0 g and $C_{p,i} = C_{p,water} = 4.184$ J/K). Q_{NPs} renders the light to heat conversion of NPs and relates the resonant absorbance of NPs at the excitation wavelength (A_λ), power of laser excitation (P_{ex}), and photothermal conversion efficiency (ϕ) through:

$$Q_{NPs} = P_{ex}(1 - 10^{-A_\lambda})\phi$$

A_λ is adjusted based on the extinction-to-absorption ratio implied in the calculated coefficients. Q_0, on the other hand, evaluates the heat produced by only solvent upon laser illumination:

$$Q_0 = h_{water} A (T_{max} - T_{amb})$$

where m and C_p are the mass and heat capacity of water. $(T_{max} - T_{amb})$ is the maximum temperature elevation generated by laser-irradiated water. A simplified heat transfer energy term, Q_e describes the heat lost to the environments, conveniently simplifying the thermal convection and radiation:

$$Q_e = hA(T - T_{amb})$$

where h is the heat transfer coefficient, A is the cross-section surface area of thermal convection of the solution to the air (the cross-section area of quartz cuvette, 1.0 cm^2). Here in this heat-transfer model, served as the mediator constant of heat loss and temperature difference between the system and the surroundings, heat-transfer coefficient is indicative of both the convective and radiative thermal transport features of the system, encompassing the boundary layer thermodynamics, fluid motion of the solvent, and surface geometries, etc. Heat transfer coefficient is relating to τ_s through:

$$h = \frac{\sum_i m_i C_{p,i}}{A \tau_s}$$

Consequently, when the system is at thermal equilibrium, external heat flux (Q_e) equals the internal laser-induced heat generation:

$$Q_e = Q_{NPs} + Q_0$$

Substituting the Q_e and Q_{NPs}, and rearranging the equation to obtain expression for photothermal conversion efficiency, ϕ:

$$\phi = \frac{hA(T_{max} - T_{amb}) - Q_0}{P_{ex}(1 - 10^{-A_\lambda})}$$

2.5 References

1. Landau, L., On the Vibrations of the Electronic Plasma. *Zh. Eksperim. i Teor. Fiz.* **1946,** *16* (7), 574-586.

2. Ryutov, D. D., Landau damping: half a century with the great discovery. *Plasma Phys. Control. Fusion* **1999,** *41*, A1-A12.

3. Linic, S.; Christopher, P.; Ingram, D. B., Plasmonic-metal nanostructures for efficient conversion of solar to chemical energy. *Nat. Mater.* **2011,** *10* (12), 911-921.

4. Zhang, Q. F.; Zhou, Y. D.; Fu, X. Q.; Villarreal, E.; Sun, L. C.; Zou, S. L.; Wang, H., Photothermal Effect, Local Field Dependence, and Charge Carrier Relaying Species in Plasmon-Driven Photocatalysis: A Case Study of Aerobic Nitrothiophenol Coupling Reaction. *J. Phys. Chem. C* **2019,** *123* (43), 26695-26704.

5. Kale, M. J.; Avanesian, T.; Christopher, P., Direct Photocatalysis by Plasmonic Nanostructures. *ACS Catal.* **2014,** *4* (1), 116-128.

6. Brongersma, M. L.; Halas, N. J.; Nordlander, P., Plasmon-induced hot carrier science and technology. *Nat. Nanotechnol.* **2015,** *10* (1), 25-34.

7. Zhang, Y. C.; He, S.; Guo, W. X.; Hu, Y.; Huang, J. W.; Mulcahy, J. R.; Wei, W. D., Surface-Plasmon-Driven Hot Electron Photochemistry. *Chem. Rev.* **2018,** *118* (6), 2927-2954.

8. Zhu, H. Y.; Chen, X.; Zheng, Z. F.; Ke, X. B.; Jaatinen, E.; Zhao, J. C.; Guo, C.; Xie, T. F.; Wang, D. J., Mechanism of supported gold nanoparticles as photocatalysts under ultraviolet and visible light irradiation. *Chem. Commun.* **2009,** (48), 7524-7526.

9. Zhao, J.; Nguyen, S. C.; Ye, R.; Ye, B. H.; Weller, H.; Somorjai, G. A.; Alivisatos, A. P.; Toste, F. D., A Comparison of Photocatalytic Activities of Gold Nanoparticles Following Plasmonic and Interband Excitation and a Strategy for Harnessing Interband Hot Carriers for Solution Phase Photocatalysis. *ACS Cent. Sci.* **2017,** *3* (5), 482-488.

10. Fu, X. Q.; Li, G. G.; Villarreal, E.; Wang, H., Hot carriers in action: multimodal photocatalysis on Au@SnO2 core-shell nanoparticles. *Nanoscale* **2019,** *11* (15), 7324-7334.

11. Sun, M. Q.; Fu, X. Q.; Chen, K. X.; Wang, H., Dual-Plasmonic Gold@Copper Sulfide Core-Shell Nanoparticles: Phase-Selective Synthesis and Multimodal Photothermal and Photocatalytic Behaviors. *ACS Appl. Mater. Interfaces* **2020,** *12* (41), 46146-46161.

12. Hou, W. B.; Hung, W. H.; Pavaskar, P.; Goeppert, A.; Aykol, M.; Cronin, S. B., Photocatalytic Conversion of CO2 to Hydrocarbon Fuels via Plasmon-Enhanced Absorption and Metallic Interband Transitions. *ACS Catal.* **2011,** *1* (8), 929-936.

13. Johnson, P. B.; Christy, R. W., Optical-Constants of Copper and Nickel as a Function of Temperature. *Phys. Rev. B* **1975,** *11* (4), 1315-1323.

14. Wang, H.; Tam, F.; Grady, N. K.; Halas, N. J., Cu nanoshells: Effects of interband transitions on the nanoparticle plasmon resonance. *J. Phys. Chem. B* **2005,** *109* (39), 18218-18222.

15. Motl, N. E.; Ewusi-Annan, E.; Sines, I. T.; Jensen, L.; Schaak, R. E., Au-Cu Alloy Nanoparticles with Tunable Compositions and Plasmonic Properties: Experimental Determination of Composition and Correlation with Theory. *J. Phys. Chem. C* **2010,** *114* (45), 19263-19269.

16. Mulvaney, P., Surface plasmon spectroscopy of nanosized metal particles. *Langmuir* **1996,** *12* (3), 788-800.

17. Sundararaman, R.; Narang, P.; Jermyn, A. S.; Goddard, W. A.; Atwater, H. A., Theoretical predictions for hot-carrier generation from surface plasmon decay. *Nat. Commun.* **2014,** *5*.

18. Kim, D.; Resasco, J.; Yu, Y.; Asiri, A. M.; Yang, P. D., Synergistic geometric and electronic effects for electrochemical reduction of carbon dioxide using gold-copper bimetallic nanoparticles. *Nat. Commun.* **2014,** *5*.

19. Gilroy, K. D.; Ruditskiy, A.; Peng, H. C.; Qin, D.; Xia, Y. N., Bimetallic Nanocrystals: Syntheses, Properties, and Applications. *Chem. Rev.* **2016,** *116* (18), 10414-10472.

20. Ozolins, V.; Wolverton, C.; Zunger, A., Cu-Au, Ag-Au, Cu-Ag, and Ni-Au intermetallics: First-principles study of temperature-composition phase diagrams and structures. *Phys. Rev. B* **1998,** *57* (11), 6427-6443.

21. Li, G. G.; Villarreal, E.; Zhang, Q. F.; Zheng, T. T.; Zhu, J. J.; Wang, H., Controlled Dealloying of Alloy Nanoparticles toward Optimization of Electrocatalysis on Spongy Metallic Nanoframes. *ACS Appl. Mater. Interfaces* **2016,** *8* (36), 23920-23931.

22. Aden, A. L.; Kerker, M., Scattering of Electromagnetic Waves from 2 Concentric Spheres. *J. Appl. Phys.* **1951,** *22* (10), 1242-1246.

23. Macdonald, F.; Lide, D. R., CRC handbook of chemistry and physics: From paper to web. *Abstr. Pap. Am. Chem. Soc.* **2003,** *225*, U552-U552.

24. Drude, P., On the electron theory of metals. *Ann. Phys.* **1900,** *1* (3), 566-613.

25. Mayer, K. M.; Hafner, J. H., Localized Surface Plasmon Resonance Sensors. *Chem. Rev.* **2011,** *111* (6), 3828-3857.

26. Scholl, J. A.; Koh, A. L.; Dionne, J. A., Quantum plasmon resonances of individual metallic nanoparticles. *Nature* **2012,** *483* (7390), 421-U68.

27. Vegard, L., The constitution of the mixed crystals and the filling of space of the atoms. *Z. Phys.* **1921,** *5*, 17-26.

28. Lubarda, V. A., On the effective lattice parameter of binary alloys. *Mech. Mater.* **2003,** *35* (1-2), 53-68.

29. Jain, P. K., Taking the Heat Off of Plasmonic Chemistry. *J. Phys. Chem. C* **2019,** *123* (40), 24347-24351.

30. Goldstein, S.; Aschengrau, D.; Diamant, Y.; Rabani, J., Photolysis of aqueous H2O2: Quantum yield and applications for polychromatic UV actinometry in photoreactors. *Environ. Sci. Technol.* **2007,** *41* (21), 7486-7490.

31. Zhang, P. N.; Li, Y. J.; Wang, D. Y.; Xia, H. B., High-Yield Production of Uniform Gold Nanoparticles with Sizes from 31 to 577 nm via One-Pot Seeded Growth and Size-Dependent SERS Property. *Part. Part. Syst. Charact.* **2016,** *33* (12), 924-932.

32. Li, G. G.; Sun, M. Q.; Villarreal, E.; Pandey, S.; Phillpot, S. R.; Wang, H., Galvanic Replacement-Driven Transformations of Atomically Intermixed Bimetallic Colloidal Nanocrystals: Effects of Compositional Stoichiometry and Structural Ordering. *Langmuir* **2018,** *34* (14), 4340-4350.

33. Roper, D. K.; Ahn, W.; Hoepfner, M., Microscale heat transfer transduced by surface plasmon resonant gold nanoparticles. *J. Phys. Chem. C* **2007,** *111* (9), 3636-3641.

CHAPTER 3

DUAL-PLASMONIC GOLD@COPPER SULFIDE CORE-SHELL NANOPARTICLES: PHASE-SELECTIVE SYNTHESES AND MULTIMODAL PHOTOTHERMAL AND PHOTOCATALYTIC BEHAVIORS

3.1 Introduction

Nanostructures of noble metals and doped semiconductors display intriguing optical properties that originate from the collective oscillations of free charge carriers, known as plasmons.[1-2] In noble metals, such as Ag and Au, localized plasmons within the confinement by nanoparticles (NPs) can be optically excited when the incident light is on resonance with the oscillations of free electrons in the conduction band (CB).[3-4] The plasmonic electron oscillations decay either radiatively through photon scattering to create dramatically enhanced local fields on the nanoparticle (NP) surfaces or nonradiatively through Landau damping, which gives rise to transient, nonthermal distribution of energetic hot electrons above the Fermi level of the metals.[5-7] The plasmonic hot electrons may be injected into unpopulated orbitals of the molecules adsorbed on the NP surfaces following Landau damping or even get directly excited in the molecular adsorbates through chemical interface damping to catalyze interfacial reactions along unique molecule-transforming pathways distinct from those typically involved in thermal catalysis and semiconductor-based photocatalysis.[7-9] These short-lived hot electrons may also undergo thermal relaxation through electron-electron, electron-surface, and electron-phonon scattering over multiple time-scales ranging from sub-picoseconds to nanoseconds, resulting in local heating of the NPs followed by heat dissipation to the surrounding media, a process known as plasmonic photothermal conversion.[5] Structurally tailored noble metal NPs, such as nanoshells,[10] nanocages,[11] nanorods,[12] and nanosponges,[13] that combine high photothermal conversion efficiencies with tunable plasmon resonances in the near-infrared (NIR) water windows have been of

particular interest for biomedical applications, such as photothermally triggered drug release and photothermal cancer therapy.

While noble metals constitute the prototype material system most intensively investigated in the field of nanoplasmonics, NPs of semiconductors, such as metal chalcogenides,[14-23] oxides,[24-27] phosphides,[28] and nitrides,[29] may also become metal-like with emerging plasmonic characteristics when they are deliberately doped to achieve appropriate free carrier concentrations. Similar to their metallic analogs, doped semiconductor NPs support localized plasmons whose resonance frequencies and spectral lineshapes can be tuned by tailoring the particle sizes and shapes as well as the local environment surrounding the NPs.[15, 17, 23, 26-27] Fundamentally distinct from those in metallic NPs, however, the oscillating charge carriers responsible for plasmon resonances in doped semiconductor NPs are essentially the free holes in the valence band (VB) of the materials rather than the delocalized conduction electrons.[1-2, 30-31] The energetic hot holes derived from the plasmon decay in doped semiconductor NPs can be harnessed for photocatalytic oxidative transformations of molecular adsorbates.[32] The non-equilibrium hot electrons, on the other hand, may also be sufficiently energetic for catalyzing reduction reactions, as exemplified by the recently discovered plasmon-driven photoreduction of nitrothiophenol on Cu vacancy-doped $Cu_{2-x}Se$ NPs.[33] Plasmon-driven photocatalysis on doped semiconductor NPs represents a largely unexplored research area full of fundamentally intriguing open questions well-worthy of in-depth investigations. Although doped semiconductor NPs have also been used as photothermal transducers for biomedical applications,[34-38] no consensus has been reached whether they outperform or underperform their metallic counterparts because the structures, compositions, and

plasmonic features of the NPs, the local heat transfer environments, and the light illumination conditions in previous investigations vary drastically from case to case, lacking a unified system that enables rigorous comparison of the intrinsic photothermal efficacies of these two distinct types of plasmonic materials.

Integration of noble metal and doped semiconductor domains in one hybrid nanoscale entity enables systematic exploration of a series of intricate photophysical and photochemical processes occurring in dual- or even multi-plasmonic heteronanostructures. Au and copper chalcogenides (Cu_xE, $1 \leq x \leq 2$, E = S, Se, or Te) represent particularly interesting materials combinations for the assembly of such dual-plasmonic heteronanostructures. A variety of Au-Cu_xE heteronanostructures with distinct structural configurations, such as Janus-like heterodimers,[39-40] core-shell NPs,[40-46] yolk-shell NPs,[47] and UFO-like NPs,[48] have been experimentally realized through deliberately designed colloidal syntheses. Interestingly, some of these heteronanostructures acted as better-performing photothermal transducers in comparison to their metal and semiconductor constituents alone,[42, 45, 48] though the detailed mechanisms underpinning such enhanced photothermal performances are still open to further scrutiny. When executing their photocatalytic functions, Au-Cu_xE heteronanostructures might also outperform the mono-component Cu_xE NPs upon optical excitations of the interband transitions primarily due to the fact that Au served as an electron sink promoting the charge separation in the excitons.[40, 43] How the plasmonic hot carriers in these Au-Cu_xE heteronanostructures behave differently from the excitons, however, still remains unexplored.

This work focuses on Au@copper sulfide core-shell NPs, which exhibit tunable, multiplex optical features dominated by three distinct types of optical transitions, specifically the free hole oscillations in the semiconductor shells, the free electron oscillations in the metallic cores, and light absorption arising from interband electronic transitions, all of which are exploitable for photothermal conversion and photocatalysis. Unlike asymmetric heteronanostructures, the choice of spherically symmetric core-shell NPs not only eliminates the complication caused by structural anisotropy but also maximizes the interfacial contact between the metal and semiconductor domains to facilitate heat and charge transfers. These dual-plasmonic core-shell NPs exhibit multimodal photothermal and photocatalytic behaviors upon selective excitations of different optical transitions, opening up unique opportunities for us to rigorously compare the photothermal transduction efficiencies of two distinct types of plasmon resonances (free-electron and free-hole oscillations) and the photocatalytic efficacies of multiple types of hot charge carriers all photoexcited within the same hybrid NPs.

3.2 Results and Discussion

Au nanocrystals typically adopt the face centered cubic (fcc) structure, which is thermodynamically favored over other crystalline phases. Only under certain special conditions can peculiar non-fcc phases emerge locally in some unconventional, exotic Au nanostructures.[49-50] In striking contrast to the structural monotony of Au is the structural diversity of copper sulfides, a large family of binary compounds embracing numerous polymorphic crystalline phases that accommodate Cu and S atoms in a variety of lattice configurations over a wide range of compositions expressed by a general formula of $Cu_{2-x}S$ ($1 \leq x \leq 2$).[51] Several crystalline phases with appreciable thermodynamic stabilities existing in both natural mineral samples and chemically synthesized colloidal NPs include covellite (CuS), yarrowite ($Cu_{1.12}S$), anilite ($Cu_{1.75}S$), digenite ($Cu_{1.8}S$), djurleite ($Cu_{1.96}S$), and chalcocite (Cu_2S),[51] which are listed in the order of increasing Cu:S stoichiometric ratios. Although structurally and compositionally distinct from each other, these binary compounds share a common feature that the S atoms form either cubic or hexagonal close-packed lattices with the structurally less ordered Cu atoms occupying various interstitial sites in the S lattices. Direct deposition of copper sulfides with specifically targeted compositional stoichiometries and crystalline phases on Au NP surfaces to form conformal core-shell nanostructures has been synthetically challenging because of the structural dissimilarity and large lattice mismatches between Au and copper sulfides.[52] While $Au@Cu_{2-x}S$ core-shell NPs have been either derived from other core-shell NPs through multistep ionic exchange processes[44-45, 53] or synthesized through seed-mediated growth guided by specifically tailored surface-capping molecular ligands,[42, 46] it remains challenging to systematically tune the Cu:S stoichiometries and crystalline phases while retaining the well-defined core-shell NP geometries. Here we

developed a straightforward seed-mediated growth method for the phase-selective synthesis of colloidal Au@copper sulfide core-shell NPs using $Cu(NO_3)_2$ and thiourea (TU) as the Cu and S precursors, respectively, in a polyol solvent, ethylene glycol (EG). By adjusting the molar ratios between the Cu and S precursors, we were able to grow nanoshells comprising Cu-deficient covellite or Cu-rich digenite on Au NP surfaces in a phase-selective and thickness-controlled manner. When exposing Au@digenite core-shell NPs to a mild oxidizing environment, the digenite shells further evolved into non-stoichiometric $Cu_{2-x}S$ phases with increased free carrier concentrations. Our synthetic approach allowed us not only to precisely control the core and shell dimensions but also to systematically tailor the crystalline structures and compositional stoichiometries of the copper sulfide shells.

Au@CuS Core-Shell NPs. As schematically illustrated in Figure 3.1A, we used Au NPs as the preformed seeds to mediate the growth of Au@CuS core-shell NPs at the boiling temperature of the EG solvent (197 ^{o}C). Keeping the Cu:TU molar ratio at 1:3 enabled us to selectively grow CuS in pure hexagonal covellite phase (space group: $P6_3/mmc$) on the Au cores without forming other non-stoichiometric crystalline phases. The average sizes of the Au cores could be precisely tuned in the range from ~ 20 nm to ~ 200 nm following a previously reported synthetic protocol,[54] while the apparent thicknesses of the CuS shells were tuned simply by adjusting the amount of $Cu(NO_3)_2$ relative to that of the Au seeds. Figures 3.1B-3.1E show the transmission electron microscopy (TEM) images of Au@CuS core-shell NPs with an average core diameter of 62 nm and various apparent shell thicknesses, which were labeled as Au@CuS-i, Au@CuS-ii, Au@CuS-iii, and Au@CuS-iv, respectively, in the order of increasing CuS

shell thickness. The core-shell heterostructure could be clearly visualized by TEM directly based on the image contrast. Instead of forming monocrystalline CuS shells with uniform thicknesses, the seed-mediated growth under the current synthetic conditions resulted in multi-crystalline CuS shells consisting of plate-like nanocrystals that were fused together to form a flower-like morphology (Figure 3.1F). The driving force for the formation of plate-like CuS sub-units in the shells was essentially tied to the intrinsic structural anisotropy of covellite. The unit cell of covellite is composed of alternating CuS_4-CuS_3-CuS_4 structural units that are connected through van der Waals S-S bonds.[55] Such an anisotropic lamella structure is not only the main reason why CuS has strong propensity to grow into quasi-two-dimensional nanoplates[17, 20, 23] but also a built-in structural factor underpinning the anisotropic plasmonic features and hyperbolic optical dispersion observed in CuS nanostructures.[23]

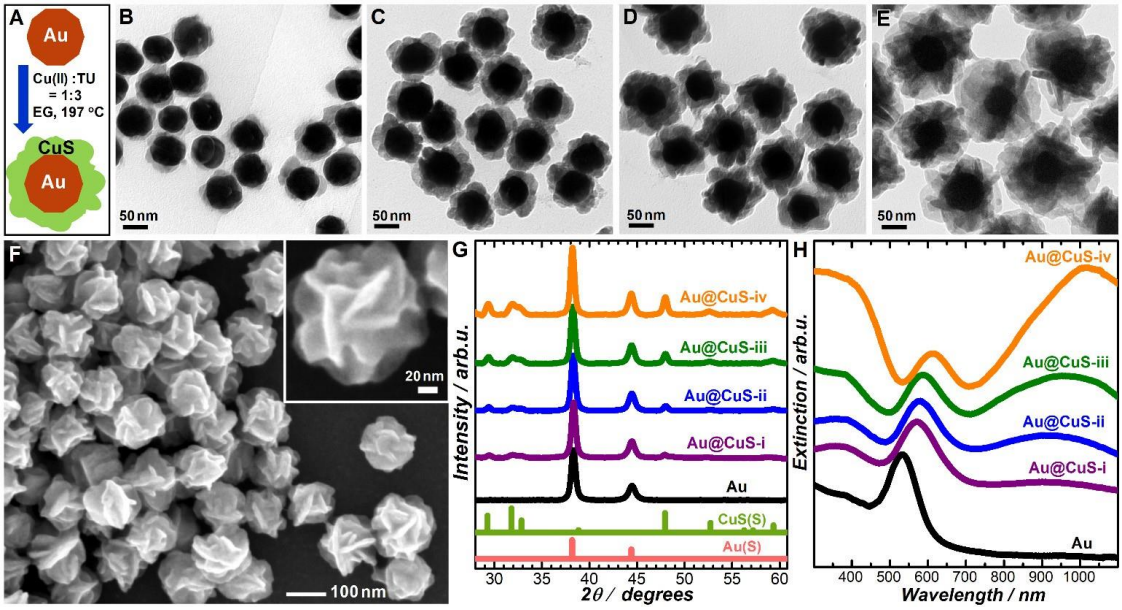

Figure 3.1. (A) Schematic illustration of the synthesis of Au@CuS core-shell NPs. TEM images of Au@CuS core-shell NPs composed of 62 nm Au cores and CuS shells with various thicknesses. The fourNP samples were labeled as (B) Au@CuS-i, (C) Au@CuS-ii, (D) Au@CuS-iii, and (E) Au@CuS-iv, respectively, in the order of increasing CuS shell thickness. (F) SEM image of Au@CuS-iv core-shell NPs.The inset shows the SEM image

of one individual particle. (G) PXRD patterns of Au NPs, Au@CuS-i, Au@CuS-ii, Au@CuS-iii, and Au@CuS-iv core-shell NPs. Standard XRD patterns for Au (JCPDS 04- 0784) and CuS (covellite, JCPDS 6-464) were also presented for reference. PXRD patterns were offset for clarity. (H) Optical extinction spectra of colloidal Au NPs, Au@CuS-i, Au@CuS-ii, Au@CuS-iii, and Au@CuS-iv core-shell NPs dispersed in H_2O. The spectra were offset for clarity.

The structures and compositions of the core-shell NPs were further characterized by powder X-ray diffraction (PXRD), high-resolution TEM (HRTEM), and EDS-based elemental analysis. As shown in Figure 3.1G, two sets of diffraction peaks corresponding to the fcc phase of Au (JCPDS 04-0784) and the covellite phase of CuS (JCPDS 6-464) were well-resolved by PXRD, with no detectable features of any other copper sulfide phases. As the shell thickness progressively increased, the PXRD peaks of covellite became increasingly more pronounced with respect to those of Au. It is revealed that the atomic ratios of S:Au and Cu:Au both increased with the shell thickness, while the Cu:S stoichiometric ratios remained close to 1:1, independent of the shell thickness.

Covellite is the most stable stoichiometric member in the entire family of copper sulfides with high density of free holes in its VB.[51] Therefore, covellite resembles heavily doped *p*-type semiconductors, exhibiting intrinsic metal-like, plasmonic properties without the need for Cu vacancy doping in its lattices.[20, 23] In the optical extinction spectra of colloidal Au@CuS core-shell NPs (dispersed in water), spectral features associated with three different optical transitions were clearly resolved (Figure 1H). The broad NIR extinction peak centered around 1000 nm signified the plasmonic hole oscillations in the CuS shells, whereas the plasmonic electron oscillations in the Au cores were optically excited in the visible region (~ 540-620 nm). The plasmon resonance band of CuS was located at longer wavelengths than those of the Au plasmons because the free hole concentration in CuS (~10^{22} cm^{-3}) was approximately one order of magnitude lower

than that in Au (~10^{23} cm^{-3}).[20, 23] The interband electronic transitions from the VB to the CB of CuS occurred when the energies of the excitation photons exceeded the band gap of CuS, giving rise to strong light absorption at wavelengths below 520 nm. We used diffuse reflectance spectroscopy (DRS) to measure the absorption spectrum of Au@CuS-iv core-shell NPs, based on which the direct band gap of the CuS shells was determined to be ~ 2.4 eV (~ 516 nm), well within the range of the values previously reported on CuS.[14, 56-57] Because the dimensions of the CuS shells were significantly larger than the Bohr radius of CuS (< 10 nm),[14] we did not expect to observe significant band gap widening due to quantum confinement in these core-shell NPs. As the shell thickness increased, both the spectral features of interband transitions and the plasmon resonances of CuS became increasingly more pronounced relative to that of the Au plasmons. The Au plasmon peak progressively red-shifted with the thickening of the CuS shells because the refractive indices of CuS were remarkably larger than those of H_2O, whereas the resonance wavelengths of the CuS plasmons remained essentially unchanged, indicating that the free hole concentrations in the CuS shells were primarily determined by the crystalline structures and compositions, independent of the shell thickness. As the thickness of the CuS shells varied, aqueous suspensions of colloidal Au@CuS core-shell NPs exhibited vivid color evolution, which was dominated by the spectral shift of the Au plasmon resonances in the visible with negligible contribution from the NIR CuS plasmons.

Au@$Cu_{1.8}$S Core-Shell NPs. As illustrated in Figure 3.2A, the crystalline structures of the copper sulfide shells switched from covellite to the cubic digenite phase (space group: $Fm\bar{3}m$) when changing the Cu:TU molar ratio in the reactant mixtures

from 1:3 to 3:1. We used Au NPs with an average diameter of 62 nm as the seeds to grow Au@$Cu_{1.8}S$ core-shell NPs with four different average shell thicknesses, which were denoted as Au@$Cu_{1.8}S$-i, Au@$Cu_{1.8}S$-ii, Au@$Cu_{1.8}S$-iii, and Au@$Cu_{1.8}S$-iv, respectively, in the order of increasing shell thickness. TEM images (Figures 3.2B-3.2E) show that the as-synthesized NPs all exhibited a spherically symmetric core-shell structure. It is verified that the Cu:S atomic ratios of various core-shell NP samples remained very close to 1.8:1, regardless of the shell thickness. While all S was fully reacted with Cu to form $Cu_{1.8}S$ shells on Au NP cores, about 32 % of the ionic Cu precursors remained in the solution phase after the completion of shell growth because the Cu was in excess with respect to S. The results of PXRD (Figure 3.2F) provided convincing evidence for the formation of pure digenite phase in the core-shell NPs. The uniform coating of Au cores with conformal $Cu_{1.8}S$ shells resulted in smoothly curved outer surfaces (Figure 3.2G), a morphology drastically different from that of Au@CuS core-shell NPs (Figure 3.1F). The distinct morphologies of the digenite and covellite shells could be interpreted as the consequence of inherent structural difference between the two crystalline phases. Digenite can be considered as the "copper deficient" analog of the fully stoichiometric cubic chalcocite (Cu_2S) phase because both digenite and cubic chalcocite share the same fcc S lattices, except that digenite contains 6 Cu vacancy sites in each unit cell.[51] Strikingly distinct from covellite, digenite does not have layered, anisotropic structural units interconnected by van der Waals S-S bonds,[58] thereby lacking the intrinsic driving force to grow into plate-shaped nanocrystalline domains.

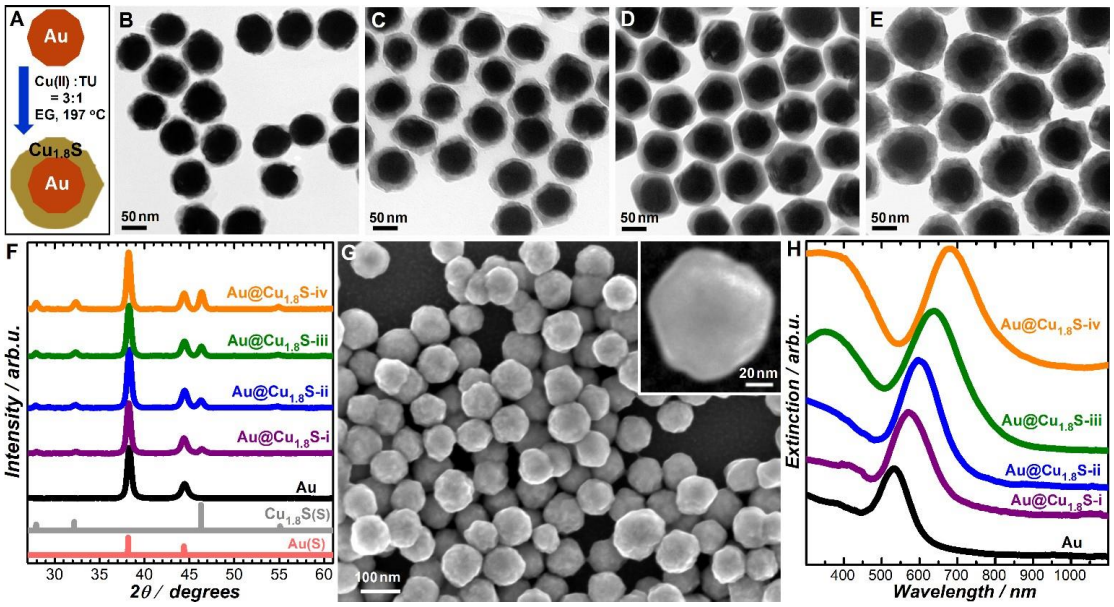

Figure 3.2. (A) Schematic illustration of the synthesis of Au@$Cu_{1.8}S$ core-shell NPs. (B-E) TEM images of Au@$Cu_{1.8}S$ core-shell NPs composed of 62 nm Au cores and CuS shells with various thicknesses. The four NP samples were labeled as (B) Au@$Cu_{1.8}S$-i, (C) Au@$Cu_{1.8}S$-ii, (D) Au@$Cu_{1.8}S$-iii, and (E) Au@$Cu_{1.8}S$-iv, respectively, in the order of increasing $Cu_{1.8}S$ shell thickness. (F) PXRD patterns of Au NPs, Au@$Cu_{1.8}S$-i, Au@ $Cu_{1.8}S$-ii, Au@$Cu_{1.8}S$-iii, and Au@$Cu_{1.8}S$-iv core-shell NPs. Standard XRD patterns for Au (JCPDS 04-0784) and $Cu_{1.8}S$ (digenite, JCPDS 6-464) were also presented for reference. PXRD patterns were offset for clarity. (G) SEM image of Au@$Cu_{1.8}S$-iv core-shell NPs. The inset shows the SEM image of one individual particle. (H) Optical extinction spectra of colloidal Au NPs, Au@$Cu_{1.8}S$- i, Au@ $Cu_{1.8}S$-ii, Au@$Cu_{1.8}S$-iii, and Au@$Cu_{1.8}S$-iv core-shell NPs. The spectra were offset for clarity.

As shown in Figure 3.2H, the extinction spectral features of colloidal Au@$Cu_{1.8}S$ core-shell NPs were dominated by the plasmonic electron oscillations of the Au cores in the visible and strong light absorption on the blue side of the Au plasmons, which arose from the VB-to-CB interband transitions in the $Cu_{1.8}S$ shells. The thickening of the $Cu_{1.8}S$ shells caused spectral red-shift of the plasmon resonance of the Au cores, giving rise to vibrant color changes of the colloidal Au@$Cu_{1.8}S$ core-shell NPs. The resonance wavelengths of the Au plasmons in the Au@$Cu_{1.8}S$ core-shell NPs depended more sensitively on the shell thickness than in the case of Au@CuS core-shell NPs, because

$Cu_{1.8}S$ had larger refractive indices than those of CuS in the visible spectral region[59] and the $Cu_{1.8}S$ shells were coated more uniformly with higher materials packing density than those of their CuS counterparts. Interestingly, we did not observe any extinction spectral features associated with the $Cu_{1.8}S$ plasmons in the wavelength range below 1100 nm because the excitation of $Cu_{1.8}S$ plasmons occurred at longer wavelengths far beyond 1100 nm. For colloidal NPs dispersed in H_2O, however, the wavelength range of extinction spectroscopic measurements was limited by the fact that H_2O started to absorb light strongly at wavelengths longer than ~1350 nm. To expand the spectral range of measurements, we switched the samples from colloidal NPs to Au@$Cu_{1.8}S$ core-shell NPs dried on a glass coverslip, which allowed us to measure the extinction spectra over a much broader wavelength range from 300 nm all the way to 3000 nm. The plasmonic features of copper sulfide nanocrystals are intimately tied to the Cu:S stoichiometry, *i. e.* the Cu vacancy doping in the crystalline lattices. The stoichiometric Cu_2S chalgocite phase is the Cu-richest member in the copper sulfide family without any Cu vacancies in its lattices. Therefore, Cu_2S is, in principle, plasmonically inactive due to lack of free holes in its VB.[14-15] However, Cu_2S is intrinsically unstable under ambient conditions and readily evolves into copper-deficient phases, most notably djurleite and digenite, by introducing Cu vacancies into the crystalline lattices.[51] Such phase transitions resulted in generation of free holes in the VB, which caused the emergence of plasmon resonances. The plasmon resonance frequencies of $Cu_{1.8}S$ NPs were significantly lower than those of their CuS counterparts essentially due to lower free carrier concentrations in $Cu_{1.8}S$ than in CuS.

Au@$Cu_{2-x}S$ Core-Shell NPs. When stored in water or ethanol as colloidal suspensions under ambient conditions, the as-synthesized Au@$Cu_{1.8}S$ core-shell NPs were found to be stable over several months without any structural or compositional changes detectable by PXRD, TEM, and EDS. However, upon exposure to a mildly oxidative environment containing H_2O_2, the $Cu_{1.8}S$ shells underwent phase transitions to gradually evolve into non-stoichiometric $Cu_{2-x}S$ phases that were more Cu vacancy-rich. Unlike Au NPs whose free electron concentration was essentially fixed, the free hole concentrations in $Cu_{2-x}S$ could be methodically modulated by adjusting the doping levels of Cu vacancies.[14-15, 22, 30] Figures 3.3A and 3.3B show the temporal evolution of the optical extinction spectra after exposing colloidal Au@$Cu_{1.8}S$-iv core-shell NPs to an aqueous solution of 0.3 mM H_2O_2. Upon initiation of the reactions, a broad extinction peak characteristic of the $Cu_{2-x}S$ plasmons emerged in the NIR, which progressively blue-shifted and became increasingly more intense during the reactions as a result of elevated doping level of Cu vacancies, *i.e.*, increased free hole concentrations in the VB of the $Cu_{2-x}S$ shells. In addition, the incorporation of Cu vacancies in the shells caused weakening and blue-shift of the Au plasmon peak due to reduced refractive indices of the materials surrounding the Au cores. The refractive indices of $Cu_{2-x}S$ were composition-dependent, with larger values of x corresponding to lower values of the refractive indices.[59] Meanwhile, the introduction of Cu vacancies led to the transformation of the originally continuous, uniform $Cu_{1.8}S$ shells into nanoporous $Cu_{2-x}S$ shells comprising loosely packed primary nanocrystals (Figures 3.3C and 3.3D). For colloidal core-shell NPs dispersed in H_2O, such nanoporosity allowed H_2O molecules to penetrate into the shells, effectively reducing the refractive indices of the materials surrounding the Au

cores. Furthermore, the onset of the interband absorption of the Au@$Cu_{2-x}S$ core-shell NPs exhibited modest but non-negligible spectral blue-shift during the reactions primarily because of the widening of the band gap caused by the increase of free hole concentrations in the VB.

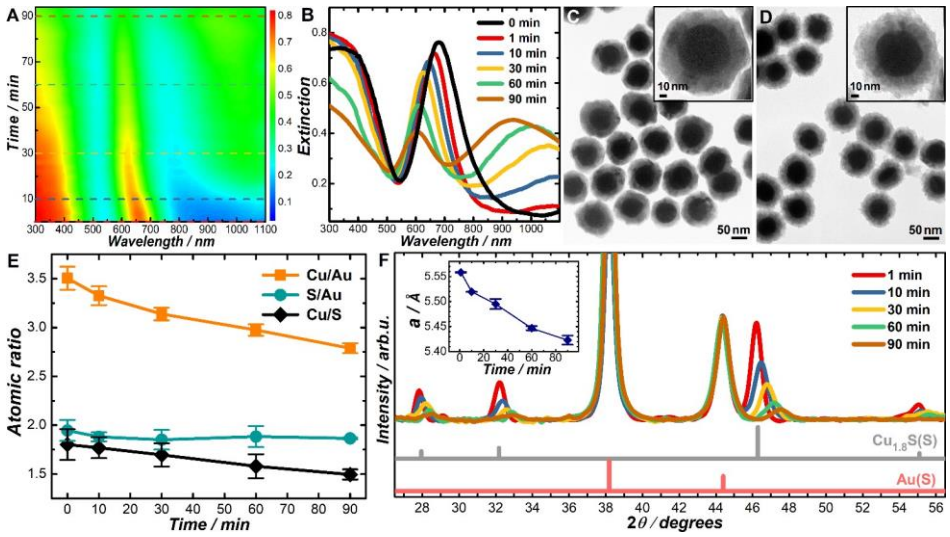

Figure 3.3. (A) Temporal evolution of extinction spectra of colloidal Au@$Cu_{1.8}S$-iv core-shell NPs upon exposure to 0.3 mM H_2O_2. (B) Snapshot extinction spectra at various reaction times (indicated by the dashlines in panel A). TEM images of the NPs obtained after exposing Au@$Cu_{1.8}S$-iv core-shell NPs to 0.3 mM H_2O_2 for (C) 10 and (D) 90 min. (E) Evolution of the Cu:Au, S:Au, and S:Cu atomic ratios of the core-shell nanoparticles (quantified by EDS) during the phase transitions. (F) PXRD patterns showing the phase transition of $Cu_{1.8}S$ to $Cu_{2-x}S$ after exposing Au@$Cu_{1.8}S$-iv core-shell NPs to 0.3 mM H_2O_2 for various reaction times. Standard XRD patterns for Au (JCPDS 04-0784) and $Cu_{1.8}S$ (digenite, JCPDS 6- 464) were also presented for reference. PXRD patterns were normalized to the intensity of Au. The inset panel shows the change of the lattice constants calculated from the PXRD patterns. The error bars represented the standard deviations of the lattice constant values calculation from (220), (200), and (111)diffraction peaks.

To further correlate the observed extinction spectral evolution to detailed structural and compositional changes of the NPs, we used EDS and PXRD to characterize the core-shell NPs that were kinetically trapped and separated from the reaction mixtures through centrifugation at various reaction stages. The EDS results (Figure 3.3E) showed that the loss of Cu from the $Cu_{2-x}S$ shells was a continuous process until a saturated

doping level of Cu vacancies was reached after 90 min, whereas no S vacancies were introduced into the crystalline lattices. Therefore, the $Cu_{2-x}S$ shells became progressively more Cu-deficient, with x varying continuously from ~ 0.2 to ~ 0.5. Figure 3.3F shows the PXRD patterns of Au@$Cu_{2-x}S$ core-shell NPs with various Cu vacancy-doping levels. To compare the relative intensities of $Cu_{2-x}S$ peaks of various samples, we chose the (200) diffraction peak of Au as an internal reference for spectral normalization considering the fact that the Au cores remained intact during the phase transitions of the shells. The intensities of the diffraction peaks of $Cu_{2-x}S$ decreased as increasing amount of Cu was removed from the shells. The Cu vacancy doping also caused shrinkage of the fcc lattices of the S atoms, as reflected by the shift of the characteristic fcc diffraction peaks toward higher Bragg angles. We calculated the lattice constants, *a*, of the fcc $Cu_{2-x}S$ (inset of Figure 3.3F) using the following equation according to the Bragg's law:

$$a = \frac{2\sin(\theta_{hkl})}{\lambda}\sqrt{h^2 + k^2 + l^2} \qquad (1),$$

where λ was the wavelength of the incident X-ray (λ = 1.5405 Å for Cu $K\alpha$) and θ_{hkl} was the incident angle for a crystalline plane designated with a miller index of (*hkl*). Apparently, the lattice constants of the fcc phase decreased with increasing doping level of Cu vacancies. It is particularly noteworthy that the fcc crystalline structure remained unchanged during the phase transitions, with no other crystalline phases detected by PXRD at any specific Cu:S stoichiometric ratios. After reacting the Au@$Cu_{1.8}S$-iv core-shell NPs with 0.3 mM H_2O_2 for 10 min, the $Cu_{2-x}S$ shells became compositionally very close to anilite ($Cu_{1.75}S$); however, no anilite phase was present in the shells as clearly shown by the PXRD results. In $Cu_{2-x}S$ compounds, the positions of the S atoms are

essentially locked by the fcc lattices, whereas the Cu atoms within the fcc sublattice of S atoms are remarkably more mobile than the S atoms.[51] Rearrangement of S atoms from fcc to other packing configurations has higher energy barriers than those of the Cu vacancy doping. Therefore, $Cu_{2-x}S$ can adopt a number of metastable fcc structures over a broad compositional range, all of which exhibit *p*-type electronic characters and support tunable plasmon resonances as the doping level of Cu vacancies varies. As increasing numbers of Cu vacancies were created, nanocavities started to form in the $Cu_{2-x}S$ shells, resulting in the formation of nanoporous shell structures.

Multimodal Photothermal Behaviors. In Au@CuS core-shell NPs, several optical transitions can be photoexcited selectively at distinct resonance frequencies to generate multiple types of intraband and interband hot carriers all directly relevant to photothermal heating. While the photothermal effects observed in noble metal NPs essentially originates from the thermal relaxation of plasmonic hot electrons, the plasmonic hole oscillations in doped semiconductor NPs also contribute to photothermal heating through nonradiative decay involving multistep hole-hole and hole-phonon scattering. In addition, the nonthermal electrons generated upon interband excitonic excitations in semiconductors undergo intraband internal conversion within the CB and nonradiative recombination with the holes in the VB, both of which deposit thermal energy to the lattice vibrations, causing temperature increase of the NPs. Au@CuS core-shell NPs provided a unique hybrid heteronanostructure ideal for quantitative assessment of the photothermal effects associated with plasmonic holes, plasmonic electrons, and excitonic charge carriers that were all photoexcited within the same NPs. We compared the multimodal photothermal behaviors of three Au@CuS core-shell NP samples with

nominally the same apparent shell thicknesses of ~ 35 nm but different average core diameters of 62, 80, and 104 nm (see TEM images of the NPs in Figures 3.4A-3.4C). The three Au NP samples were denoted as Au-1, Au-2, and Au-3, respectively, in the order of increasing particle sizes, and the corresponding core-shell NPs were denoted as Au-1@CuS, Au-2@CuS, and Au-3@CuS accordingly. Figure 3.4D shows the extinction spectra of colloidal suspensions of Au NPs and Au@CuS core-shell NPs with particle concentrations all kept of 4×10^9 particles mL^{-1}. As the average sizes of the Au NPs increased from 62 to 104 nm, the Au plasmon resonance red-shifted by 45 nm in wavelength and the extinction peak became more intense due to increased extinction cross-sections of the NPs. For the Au@CuS core-shell NPs, the Au plasmon peak red-shifted with the increase of core sizes, whereas the spectral positions of both the plasmon resonances and the interband transitions of the CuS shells remained essentially unchanged as the core size varied.

The photothermal performances of Au@CuS core-shell NPs were evaluated by monitoring the temperature evolution of 2.0 mL aqueous suspensions of colloidal NPs (4×10^9 particles mL^{-1}) in a quartz cuvette (1.0 cm × 1.0 cm × 4.5 cm) embedded in a styrofoam holder under illumination by collimated continuous-wave lasers (see details in the Experimental Section). We selectively excited the CuS plasmons, the Au plasmons, and the interband transitions at excitation wavelengths (λ_{ex}) of 980, 638, and 445 nm, respectively, with an excitation power (P_{ex}) fixed at 1.0 W. The colloidal NPs were illuminated with laser continuously until reaching a steady state temperature, and then the solution was allowed to naturally cool down to ambient temperature without laser illumination (Figure 3.4E).

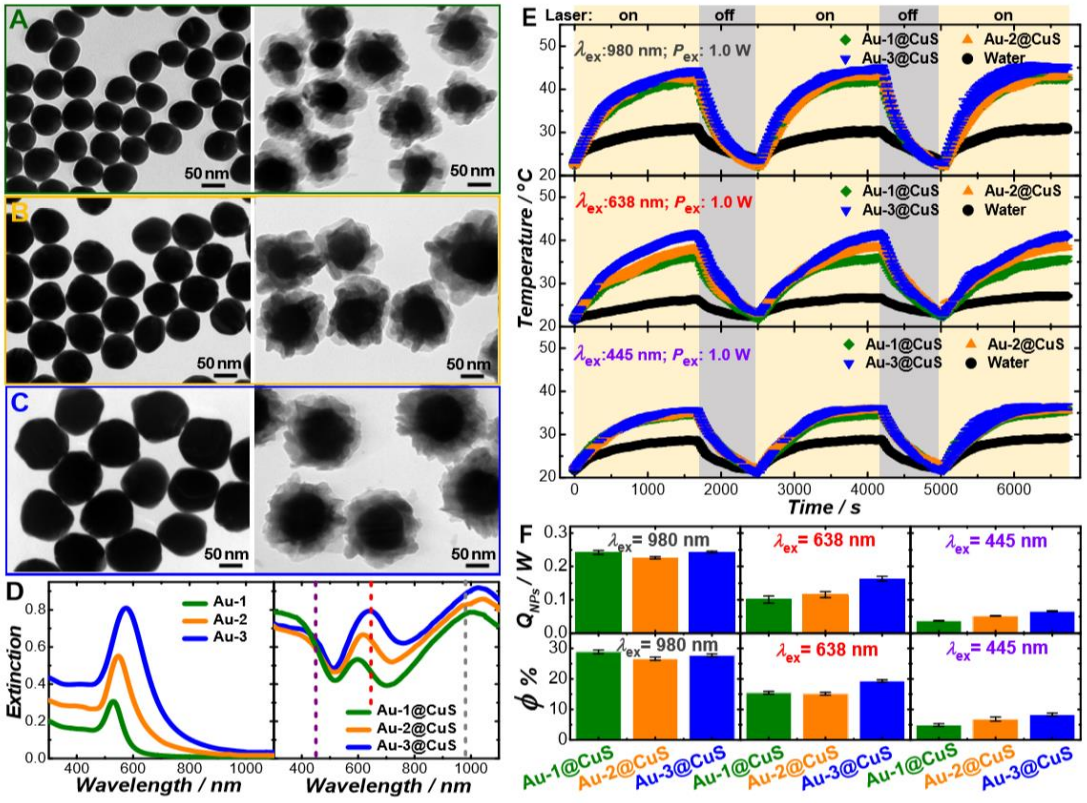

Figure 3.4. TEM images of (A) Au-1 and Au-1@CuS, (B) Au-2 and and Au-2@CuS, and (C) Au-3 and Au-3@CuS NPs. The left and right panels showed the TEM images of Au NPs and the corresponding Au@CuS core-shell NPs, respectively. (D) Extinction spectra of various (*left panel*) Au NPs and (*right panel*) Au@CuS core-shell NPs. The λ_{ex} for photothermal measurements were indicated by vertical dash lines in the right panel. (E) Temperature evolution of colloidal Au@CuS core-shell NPs and pure H_2O over 3 cycles of laser illumination (λ_{ex} = 980 nm, 638 nm, and 445 nm; P_{ex} = 1.0 W) and natural cooling under ambient conditions. The error bars represent the standard deviations of 3 experimental runs under each condition. (F) ϕ of Au-1@CuS, Au-2@CuS, and Au-3@CuS core-shell NPs at various λ_{ex}.

The results of photothermal measurements were analyzed using a thermophysical model developed by Roper and coworkers,[60] as described in detail in Experiments and Methods section. When the photon energy input and system heat dissipation reached the equilibrium, the photothermal heat generation in the NPs, Q_{NPs}, could be calculated using the following equation,

$$Q_{NPs} = hA(T_{max} - T_{amb}) - Q_0 \qquad (2),$$

where T_{amb} was the ambient temperature and T_{max} was the maximum temperature of the colloidal suspensions when reaching the thermal equilibrium under laser illumination. h was the heat transfer coefficient, which could be obtained by fitting the experimentally measured cooling curves. A was the cross-section area of the thermal convection of the solution to the ambient air. Q_0 referred to the heat generated by the H_2O solvent under laser illumination. The photothermal transduction efficiency, ϕ, was related to Q_{NPs}, the optical extinction of the colloidal NPs at the incident wavelength, E_λ, and excitation power, P_{ex}, as expressed by the following equation,

$$\phi = \frac{Q_{NPs}}{P_{ex}(1-10^{-E_\lambda})} \times 100\,\% \qquad (3).$$

In Figure 3.4F, we directly compared the Q_{NPs} and ϕ values of various Au@CuS core-shell NPs at different λ_{ex}. When the CuS plasmons were excited at λ_{ex} of 980 nm, the three core-shell NP samples exhibited similar Q_{NPs} and ϕ values because of their similar plasmon resonance wavelengths and comparable optical extinctions at 980 nm. At λ_{ex} of 638 nm, Q_{NPs} increased as the plasmons of the Au cores became more resonant with the excitation laser. The Q_{NPs} of Au-3@CuS was ~ 60 % higher than that of Au-1@CuS because of resonant excitation of the Au plasmons. However, the ϕ of Au-3@CuS was only ~ 20 % higher than that of Au-1@CuS. The differences in ϕ among the three NP samples under comparison were less significant than those in Q_{NPs} primarily due to higher extinction and stronger scattering of the larger NPs. Comparing the ϕ values at λ_{ex} of 980 and 638 nm, it was apparent that CuS plasmons were more efficient than Au plasmons in terms of photothermal conversion when using the Au@CuS core-shell NPs as the photothermal transducers. It turned out to be less meaningful, however, to directly compare the ϕ values of our samples to those of other noble metal and copper

chalcogenide NPs reported in the literature, because ϕ was sensitively dependent upon the sizes, shapes, and compositions of the NPs, the detailed light absorption and scattering properties of the NPs, the excitation wavelengths, and the local environments for heat dissipation, all of which varied drastically from case to case in previous studies. We believe there is still plenty of room for the further improvement of ϕ for both the CuS and Au plasmons through structural engineering of the cores, the shells, and the core-shell interfaces. The excitonic charge carriers generated upon the VB-to-CB interband transitions in CuS were much longer-lived than the plasmonic electrons and holes, and appeared less efficient in generating heat during the thermal relaxation processes. The excitations of the interband transitions at λ_{ex} of 445 nm resulted in much less efficient photothermal conversion with ϕ values below 8 %, which were significantly lower than those of the plasmon excitations.

Several Au@copper sulfide heteronanostructures have been previously observed to exhibit enhanced photothermal transducing performances in comparison to the physical mixtures of their Au and copper sulfide components, hypothetically owing to the coupling between the metal and semiconductor plasmons.[45, 48] To better understand how the Au cores modified the photothermal behaviors of the CuS shells, we synthesized CuS NPs (see experimental details in Experiments and Methods section), which served as a monocomponent counterpart for comparative studies. The as-synthesized CuS NPs exhibited a flower-like morphology similar to that of their core-shell analogs, with an average diameter around 120 nm, which was comparable to that of Au-1@CuS core-shell NPs. The band gap of the Cu NPs was determined to be ~ 2.4 eV, in excellent agreement with that of the CuS shells in the Au@CuS core-shell NPs. The presence of the Au cores

substantially enhanced the optical extinction in the NIR and blue-shifted the CuS plasmon resonances, which could be interpreted most reasonably in the context of local-field enhancements and charge transfer between Au and CuS. Electrodynamic simulations indicated that although the Au plasmons were off-resonance with NIR excitations, the local fields on Au NP surfaces were still enhanced to certain extent,[48] which was responsible for enhancing the NIR light absorption by the CuS shells in the hybrid heteronanostructures. In addition, the interfacial electron transfer from the plasmonically excited CuS shells to the Au cores resulted in increased free hole concentrations in CuS, causing spectral blue-shift of the CuS plasmon resonances and enhancement of light absorption at the resonance frequencies. Such enhanced NIR absorption and plasmon blue-shift were also previously observed in UFO-like Au-$Cu_{1.8}S$ heteronanostructures[48] and Au@$Cu_{2-x}S$ core-shell NPs.[45]

Multimodal Photocatalytic Behaviors. In Au@CuS core-shell NPs, multiple types of hot carriers could be selectively photoexcited, enabling us to systematically compare the photocatalytic efficacies of hot carriers derived from plasmonic hole oscillations, plasmonic electron oscillations, and interband electronic transitions. We chose photocatalytic mineralization of Rhodamine B (RhB) dye molecules in aqueous solution at the neutral pH of 7.0 mediated by an efficient electron acceptor, H_2O_2, as a model reaction for detailed kinetic studies (see details in the Experimental Section). The injection of photoexcited hot electrons into the antibonding π^* orbital of the surface-adsorbed H_2O_2 effectively triggered the cleavage of the O-O bond to generate •OH radicals, a reactive oxygen species (ROS) capable of driving the degradation of RhB and other aromatic organic molecules into fully mineralized small molecules, such as CO_2

and H_2O.[61] The kinetics of the photocatalytic reactions could be resolved most conveniently using UV-vis absorption spectroscopy by monitoring the temporal intensity evolution of the characteristic absorption band of RhB centered at 553 nm.

Figure 3.5A illustrates the energy levels of the VB and CB of the CuS shell with respect to that of the Fermi level of the Au core, E_F(Au), on an energy scale of eV with the vacuum level serving as the reference. E_F(Au) was located ~5.1 eV below the vacuum. The Fermi level of CuS, E_F(CuS), represented the chemical potential of electrons in the semiconductor, which was, in essence, equal to absolute electronegativity, -χ.[62] The χ value of CuS was estimated empirically from the arithmetic mean of the electron affinity and the first ionization energy of the constituent elements, which was reported to be 5.3 eV in the literature.[56, 62] Therefore, E_F(CuS) was located ~5.3 eV below the vacuum, aligned closely to the E_F(Au). The energy difference between the VB and the CB of the CuS was the band gap, which was measured to be 2.4 eV for the Au@CuS core-shell NPs. Because of its *p*-type nature, the Fermi level of CuS was located closer to the edge of the VB than to the CB. While the quantitative determination of the exact positions of the band-edges of the VB and CB of CuS requires carefully designed measurements and computations, the qualitative illustration of the relative band positions shown in Figure 3.5A allowed us to rationally interpret a series of charge transfer processes involved in the photocatalytic reactions. Photoexcitation of the CuS plasmons at λ_{ex} of 980 nm resulted in nonthermal distribution of plasmonic hot holes in the range from E_F(CuS) to E_F(CuS)-1.26 eV, leaving the hot electrons above E_F(CuS). The energetic hot electrons injected into the surface-adsorbed H_2O_2 could be harnessed to initiate the •OH-driven mineralization of RhB, while the hot holes were most likely to be

consumed by the O_2 evolution from H_2O (standard redox potential of O_2/H_2O was -5.7 eV). At λ_{ex} of 980 nm, the transfer of the plasmonic hot electrons from CuS to surface-adsorbed H_2O_2 was strongly favored over the electron transfer from CuS to Au because H_2O_2 was a more efficient electron acceptor than the electron-rich Au nanoparticles, as indicated in energy diagrams of schematic illustrations in Figure 3.5. This pathway served as the major reaction pathway to drive the photocatalytic reaction. While the complete mineralization of RhB involved multiple steps of reactions, the time-resolved UV-vis absorption spectroscopy only allowed us to resolve the kinetics of the decolorization of RhB.

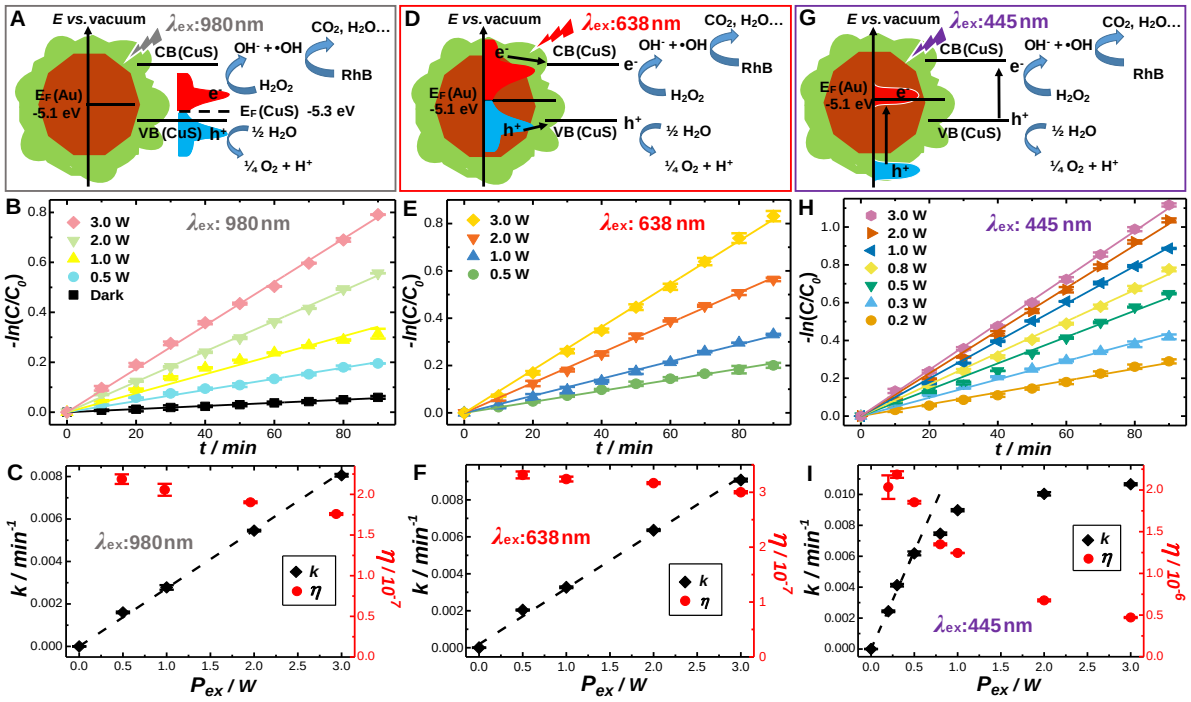

Figure 3.5. Scheme illustrating the mechanisms of photocatalytic mineralization of RhB on Au@CuS core-shell NPs at λ_{ex} of (A) 980, (D) 638, and (G) 445 nm. P_{ex}-dependent temporal evolution of -ln(C/C_0) during photocatalytic mineralization of RhB on Au-3@CuS core-shell nanoparticles at λ_{ex} of (B) 980, (E) 638, and (H) 445 nm. P_{ex}-dependence of k and η at λ_{ex} of (C) 980, (F) 638, and (I) 445 nm. The error bars in panels B, E, and H represented the standard deviations of 3 experimental runs under each condition. Theerror bars of k represent the standard deviations obtained from least squares curve fitting.

Simplifying the decolorization of RhB as an elementary reaction between •OH and RhB, the derivative form of the rate law could be written as

$$-\frac{d[RhB]}{dt} = k'[RhB][^{\bullet}OH] \qquad (4),$$

where *k'* was a second-order rate constant. Considering the fact that H_2O_2 was in large excess with respect to RhB and further assuming a steady state concentration of the •OH radicals, it could be further simplified as a pseudo-first-order reaction. As shown in Figure 3.5B, the rates of RhB decolorization catalyzed by Au-3@CuS core-shell NPs at λ_{ex} of 980 nm could be well-described by a first-order rate law:

$$-\ln\frac{C}{C_0} = -\ln\frac{I}{I_0} = k'' \times t \qquad (5),$$

where C_0 was the initial concentration of RhB, and *C* was the concentration of RhB at a reaction time, *t*. *C* was directly proportional to the intensity of the absorption peak at 553 nm, *I*, according to the Beer-Lambert Law. *k"* was the apparent first-order rate constant, which could be obtained by fitting the temporal evolution of the $-ln(C/C_0)$ with a linear equation. This reaction was found to be spontaneous even without laser illumination, in line with previous observations that CuS NPs exhibited intrinsic peroxidase-mimicking activities toward the decomposition of H_2O_2 into •OH.[63-64] Although the dark reaction was kinetically very slow, illumination of the reaction mixtures with the 980 nm laser drastically accelerated the molecule-transforming processes as a result of plasmon-driven photocatalysis. We further subtracted the rate constant of the dark reaction, k_{dark}, from *k"* to obtained *k*, a rate constant that more accurately reflected the intrinsic rate of the photocatalytic reactions. When the excitation

power, P_{ex}, was varied in the range of 0-3.0 W, k was found to be proportional to P_{ex} (Figure 3.5C), strongly suggesting that the photocatalytic reactions were driven by plasmonic hot carriers with negligible contribution from photothermal heating, which was signified by a superlinear dependence of k on P_{ex} underpinned by the Arrhenius relation.[7, 65-66] To suppress the temperature elevation due to photothermal heating, we kept the colloidal photocatalysts under fast magnetic stir and immersed 2 mL of the reaction mixtures in a large water bath (4 L in volume) during the entire reaction process to facilitate rapid heat dissipation to the surroundings.[67] Increasing the reaction temperature from room temperature to 50 °C only led to a slight increase (less than 10%) in the rate of the dark reactions, verifying that the kinetic enhancement was dominated by plasmon-driven photocatalysis rather than the photothermal effects. We calculated the apparent photonic efficiency, η, which was defined as the ratio between the number of hot electrons harnessed for the reactions and the number of photons incident on the samples over a 1-hour reaction time. According to the mechanism illustrated in Figure 3.5A, one hot electron injected into the surface-adsorbed H_2O_2 induced the generation of one •OH radical. Assuming that the reaction consumed •OH and RhB at a stoichiometric ratio of 1:1, we calculated η using the following equation:

$$\eta = \frac{h \times c \times V \times N_A \times (C_0 - C_{1h})}{P_{ex} \times \lambda_{ex} \times 3600\,s} \qquad (6),$$

where h was the Planck's constant (6.626×10^{-34} m^2 kg s^{-1}), c was the speed of light (3.0×10^8 m s^{-1}), V was the total volume of the reaction mixtures (2.0×10^{-3} L), N_A was the Avogadro's number (6.022×10^{23} mol^{-1}), C_0 was the initial concentration of RhB (1×10^{-6} M), and C_{1h} was the concentration of RhB at a reaction time of 1 h. The η values

of Au-3@CuS core-shell NPs at λ_{ex} of 980 nm and various P_{ex} were calculated to be on the order of 10^{-7} (Figure 3.5C). In principle, these calculated η values were significantly lower than the actual quantum efficiency, which was defined as the ratio between the number of hot electrons involved in the reactions and the number of photons absorbed by the colloidal NPs. At a NP concentration of 1 x 10^9 particles mL^{-1}, about 60 % of the incident photons (λ_{ex} of 980 nm) were transmitted through the samples without being absorbed or scattered by the NPs. In addition, a significant portion of the incident photons were scattered by the NPs rather than being absorbed due to the relatively large particle sizes. Furthermore, η was calculated assuming the •OH:RhB reaction stoichiometry to be 1:1, which led to significant underestimate of η values because the complete mineralization of one RhB molecule required the participation of multiple •OH radicals derived from the hot electron-driven photolysis of H_2O_2.[61]

When switching the λ_{ex} from 980 nm to 638 nm, the plasmonic electron oscillations in the Au cores were selectively photoexcited, which gave rise to the nonthermal distribution of energetic hot electrons and hot holes above and below the Fermi level of Au, respectively. A subpopulation of the hot electrons had sufficient energy to transfer to the CB of CuS by overcoming the Schottky barriers at the Au-CuS interface, as illustrated in Figure 3.5D. The electrons injected into the CB of CuS could then be exploited for the photocatalytic mineralization of RhB. Meanwhile, some of the hot holes photoexcited in the Au cores might also be transferred to the VB of CuS and subsequently catalyzed the O_2 evolution from H_2O. In analogy to the case of CuS plasmons, the reactions driven by the hot carriers derived from the Au plasmons also obeyed the first-order kinetics (Figure 3.5E) and k increased linearly with P_{ex} when P_{ex}

was varied from 0 to 3.0 W (Figure 3.5F). The photoexcitations of the plasmonic electron oscillations in Au cores and the plasmonic hole oscillations in CuS shells resulted in similar k values at a given P_{ex}, and the η values at λ_{ex} of 638 nm were calculated to be about 1.5 times of those at λ_{ex} of 980 nm (Figure 3.5F).

We further explored the photocatalysis driven by the excitonic charge carriers derived from the photoexcitation of VB-to-CB interband transitions in the CuS shells at λ_{ex} of 445 nm, as illustrated in Figure 3.5G. Besides the interband transitions of CuS, the d-to-sp interband electronic transitions of Au were also excited when the energy of the excitation photons exceeded 2.3 eV (λ_{ex} < 538 nm).[68-69] However, the interband transitions of Au resulted in photoexcited electrons in the CB distributed near the Fermi level of Au, energetically insufficient to transfer into the CB of CuS to execute their photocatalytic functions. It was worth mentioning that H_2O_2 underwent photolysis to form •OH radicals when illuminated with UV, violet, or blue light.[70] At λ_{ex} of 445 nm, the decolorization of RhB induced by H_2O_2 photolysis appeared to be a first order reaction occurring at a slow but non-negligible rate even in the absence of any photocatalysts. The contribution of H_2O_2 photolysis to the overall rates of the photocatalytic RhB decolorization was subtracted when calculating the k values at λ_{ex} of 445 nm. Although the •OH-mediated reaction mechanism (Figure 3.5G) and the first-order reaction kinetics (Figure 3.5H) remained essentially unchanged, the interband excitations generated excitonic electron-hole pairs that were much longer-lived than the plasmonic hot carriers, resulting in remarkably higher k and η values than those of the plasmon-driven reactions (Figure 3.5I). The k of the interband exciton-driven reactions at λ_{ex} of 445 nm exhibited an excitation power dependence that was strikingly distinct from those of the plasmon-

driven photocatalytic reactions at λ_{ex} of 638 and 980 nm. As shown in Figure 3.5I, under weak excitations (P_{ex} < 0.8 W), the linear relationship between k and P_{ex} still held, and η was independent of P_{ex}. The values of η in this low P_{ex} regime were on the order of 10^{-6}, which were approximately one order of magnitude higher than those of the plasmon-driven reactions. However, as P_{ex} further increased, k started to deviate significantly from the linear dependence on P_{ex}, asymptotically approaching a plateau at P_{ex} above 2.0 W. In the high P_{ex} regime, increase of P_{ex} caused η to drop remarkably by more than 75 % until reaching P_{ex} of 3.0 W. The observed deviation from the linear power dependence could be interpreted primarily as the consequence of saturated optical excitations of the interband transitions. Interestingly, in the P_{ex} range of 0-3.0 W, such saturation of optical excitations was not observed when exciting the plasmons at λ_{ex} of 638 and 980 nm essentially due to the substantially shorter life-times and faster decay of the plasmonic hot carriers in comparison to those of the interband excitonic charge carriers.[5]

Regardless of which optical transition in the Au@CuS core-shell NPs was photoexcited, the photocatalytic mineralization of RhB was always driven by the hot electrons under the current reaction conditions. Neither the plasmonic hot holes nor the interband excitonic holes were capable of driving the direct oxidative degradation of the RhB molecules or the formation of •OH through heterolytic cleavage of H_2O (standard redox potential of •OH/H_2O was -7.5 eV *vs.* vacuum). The results of the control experiments in the absence of H_2O_2 further suggested that the electron acceptor mediating the photocatalytic reactions was essentially H_2O_2 rather the molecular O_2 dissolved in water. Other than being harnessed for photocatalysis, the photoexcited holes may also cause the photo-corrosion of the photocatalysts.[68] However, this possibility was ruled out

because the Au@CuS core-shell NPs exhibited excellent photo-stability and catalytic durability over multiple cycles of photocatalytic reactions. Therefore, it was most likely that the photoexcited holes were used to drive the O_2 evolution from H_2O. The pH values of the reaction solutions at various λ_{ex} were all found to remain around 7 during the photocatalytic reactions, fully in line with the mechanisms schematically illustrated in Figures 3.5A, 3.5D, and 3.5G.

To further unravel the structure-property relationship underpinning the multimodal photocatalytic behaviors, we performed systematic comparative studies on several groups of NP samples. We first compared the photocatalytic activities of a group of Au@CuS core-shell NP samples (Au-1@CuS, Au-2@CuS, and Au-3@CuS) with nominally the same apparent shell thickness but different average core sizes. In this set of comparative studies, the concentrations of the colloidal NPs were all kept at 1 x 10^9 particles mL^{-1}.

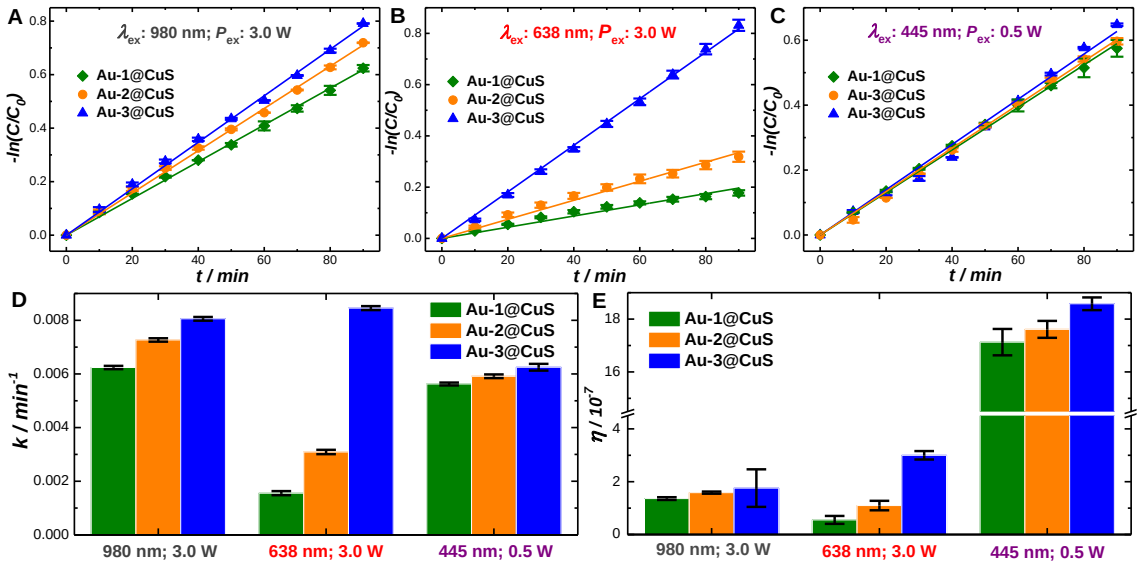

Figure 3.6. Temporal evolution of -ln(C/C_0) during photocatalytic mineralization of RhB on Au-1@CuS, Au-2@CuS, and Au-3@CuS core-shell NPs at (A) λ_{ex} of 980 nm and P_{ex} of 3.0 W, (B) λ_{ex} of 638 nm andP_{ex} of 3.0 W, and (C) λ_{ex} of 445 nm and P_{ex} of

0.5 W. Comparison of (D) k and (E) η of Au-1@CuS, Au-2@CuS, and Au-3@CuS core-shell NPs at various λ_{ex} and P_{ex}.

The photocatalytic reactions occurring on the three NP samples under comparison all obeyed the first-order rate law upon optical excitations of the CuS plasmons at λ_{ex} of 980 nm (Figure 3.6A), the Au plasmons at λ_{ex} of 638 nm (Figure 3.6B), and the CuS interband transitions at λ_{ex} of 445 nm (Figure 3.6C). At λ_{ex} of 638 nm, Au-3@CuS core-shell NPs exhibited the highest k and η values because of the on-resonance excitation of the Au plasmons. As the core sizes decreased, the Au plasmons were detuned from the excitation, resulting in significant decrease in both k (Figure 3.6D) and η (Figure 3.6E). At λ_{ex} of 980 and 445 nm, both the k and η were observed to increase with the sizes of the Au cores primarily due to higher amount of materials in the CuS shells and larger surface areas of the NPs. However, the differences in k and η among the three samples were remarkably less significant than those at λ_{ex} of 638 nm, because both the plasmon resonances and the band gap of the CuS shells were essentially unshifted when the core sizes varied. The interband excitations were photocatalytically more efficient than the plasmonic excitations, as evidenced by the higher η values at λ_{ex} of 445 nm than those at λ_{ex} of 980 and 638 nm (Figure 3.6E).

3.3 Conclusion

We combined metallic Au with semiconducting copper sulfides in a core-shell NP geometry to construct dual-plasmonic heteronanostructures that exhibited multiplex optical characteristics originating from plasmonic hole oscillations, plasmonic electron oscillations, and interband electronic transitions. Through deliberately designed seed-mediated growth and post-synthesis phase transitions, we successfully synthesized colloidal core-shell NPs composed of fcc Au cores coated with covellite, digenite, and

non-stoichiometric $Cu_{2-x}S$ shells in a phase-selective and size-controlled manner. The frequencies of the plasmonic electron oscillations in the Au cores could be tuned in the visible by tailoring the core and shell dimensions, whereas the plasmon resonance frequencies of the copper sulfide shells were tuned in the NIR through variation of the free hole concentrations, which were intimately tied to the crystalline phases and Cu:S stoichiometric ratios. These dual-plasmonic core-shell NPs exhibited unique optical tunability and multimodality, enabling us to selectively excite different optical transitions at distinct excitation wavelengths to rigorously compare the photothermal transduction efficiencies and the photocatalytic efficacies of multiple types of hot charge carriers all photoexcited in the same metal-semiconductor heteronanostructures. In these geometrically simple, spherical core-shell NPs, the hot carriers derived from the electron and hole plasmons exhibited commensurate photothermal and photocatalytic efficiencies when the plasmonic hole oscillations were off-resonance with the plasmonic electron oscillations. It is possible, however, to further improve the photothermal and photocatalytic efficiencies if the plasmons of both the Au cores and the copper sulfide shells are tuned to be on resonance with each other in the NIR, which can be achieved most straightforwardly by substituting the spherical Au cores with NIR-resonant Au NPs adopting non-spherical anisotropic shapes, such as nanorods.[12] These anisotropic core-shell heteronanostructures provide a structurally more complex materials system that allows us to further improve the photothermal and photocatalytic performances by rationally tuning the plasmon coupling between the metal and doped semiconductor domains, which is well-worthy of meticulous investigations in the future. We also found that the interband excitonic charge carriers were photocatalytically more efficient than

the intraband plasmonic hot carriers, whereas the plasmonic hot carriers exhibited higher photothermal efficiencies than the interband excitons. Our results further imply that with a fixed number of photoexcited hot carriers in a NP, the optimization of the photocatalytic performance is inevitably accompanied by compromised photothermal efficacy and vice versa because the photocatalysis and photothermal conversion are essentially tied to two competing non-radiative decay pathways of photoexcited hot carriers. This work provides important insights concerning the intrinsic photothermal and photocatalytic efficacies of multiple types of photoexcited charge carriers in hybrid heteronanostructures. These insights serve as important guiding principles for the design and construction of structurally sophisticated dual- or even mulit-plasmonic heteronanostructures that exhibit multiplex optical properties fine-optimizable for photothermal and photocatalytic applications.

3.4 Experiments and Method

Chemicals and Materials. Copper nitrate hydrate ($Cu(NO_3)_2 \cdot 3H_2O$), chloroauric acid ($HAuCl_4 \cdot 4H_2O$), ethylene glycol (EG), thiourea (TU), polyvinylpyrrolidone (PVP, average molecular weight of 58,000), tetraethylene glycol (TEG), and rhodamine B (RhB) were purchased from Alfa Aesar. Hydrogen peroxide (30% by volume, 9.8 M) was purchased from Ward's science. Trizma base (TB) was purchased from Sigma-Aldrich. Trisodium citrate dihydrate ($Na_3C_6H_5O_7 \cdot 2H_2O$) was purchased from Fisher Scientific. All reagents received were used without further purification. Ultrapure Milli-Q water (18.2 Ω) was used for all experiments.

Characterizations. The transmission electron microscopy (TEM) images were obtained using a Hitachi H-7800 transmission electron microscope, operated at an

accelerating voltage of 100 kV. High-resolution TEM (HRTEM) images were obtained using a JEOL JEM-2100 transmission electron microscope operated at an accelerating voltage of 200 kV. Samples for TEM measurements were dispersed in ethanol and drop-dried on 300 mesh carbon-coated Cu grids (Electron Microscopy Science Inc.). The scanning electron microscopy (SEM) images and energy dispersive spectroscopy (EDS) measurements were conducted using a Zeiss Ultraplus thermal field emission scanning electron microscope. An EDS unit attached to the microscope was used to quantify the Au, Cu, and S stoichiometries in the samples. Atomic ratios were quantified based on the relative area of the Au Mα, Cu Lα, and S Kα peaks in the EDS spectra. Samples for SEM and EDS measurements were dispersed in ethanol and drop-dried on silicon wafers. Powder X-ray diffraction (PXRD) patterns were collected on a SAXSLab Ganesha at the South Carolina Collaborative (Cu Kα = 1.5405 Å). The optical extinction spectra of colloidal NPs dispersed in water were recorded at room temperature using a Beckman coulter Du 640 spectrophotometer. To characterize the broad-band plasmon resonance of the Au@$Cu_{1.8}S$ core-shell NPs, optical extinction spectra were collected on glass-supported NPs using Cary 5000 UV/vis/NIR spectrophotometer in the wavelength range of 300-3000 nm. The diffuse reflectance spectroscopy (DRS) measurements were performed on a UV-2600 spectrophotometer (Shimadzu, Japan) equipped with an integration sphere. $BaSO_4$ powders were used as a reference. Raman spectra were acquired on a Bayspec Nomadic confocal Raman microscopy built on an Olympus BX51 microscope. A 785 nm continuous wave diode laser was used as an excitation source. The Raman spectra were collected from powder samples on glass coverslips at an excitation power of 5 mW and spectral acquisition time of 1 min.

Synthesis of Au Nanoparticles (NPs). Colloidal Au NPs were synthesized following a previously reported protocol.[71] Briefly, 17 nm Au seed NPs were first synthesized by reducing chloroauric acid with trisodium citrate in an aqueous solution. 1.5 mL of 1 wt % trisodium citrate aqueous solution was added into 48 mL boiling water under magnetic stir. Then 0.5 mL of 25 mM chloroauric acid was injected into the solution. The reaction was kept at boiling temperature for 30 minutes. The particle concentration, C_{NPs}, of the resulting 17 nm Au seeds was calculated based on the optical extinction spectrum using the following equation,

$$C_{NPs}(particles\ mL^{-1}) = \frac{2.3 \times E}{Q_{ext} \times \sigma(cm^2) \times l(cm)} \qquad \text{(Equation E1),}$$

where E is the optical extinction of the colloidal Au NPs at the plasmon peak wavelength (524 nm), Q_{ext} is the extinction coefficient (optical cross-section/physical cross-section), which was calculated to be 1.137 for a spherical Au NP with a diameter of 17 nm dispersed in water at a wavelength of 524 nm according to the Mie scattering theory calculations using the dielectric functions of Au reported by Johnson and Christy.[72] σ is the physical cross-section of the Au NPs, which is $\pi \times (8.5 \times 10^{-7})^2$ nm^2. l is path-length of the colloidal samples, which was 1 cm in this case.

The resulting 17 nm Au NPs were used next for seed-mediated regrowth to obtain larger Au NPs upon reduction of chloroauric acid with trizma base (TB). Typically, 2 mL of 0.1 M of TB was added into 45 mL boiling water under magnetic stir. After 10 minutes of stirring, 1 mL of 25 mM of chloroauric acid and 2 mL of 17 nm Au seed colloids were added. The reaction solution was maintained at gentle boil for 30 minutes. The amount of 17 nm Au seed particles introduced was varied in order to obtain Au NPs

with desired particle sizes. This method enabled us to tune the average diameters of Au NPs in the range from ~ 25 nm to ~ 200 nm.

Synthesis of CuS NPs. CuS NPs was synthesized using TEG as the solvent. Briefly, 0.5 mL of 0.1 M $Cu(NO_3)_2$ and 1.5 mL of 0.1 M TU were added into 8 mL of TEG containing 0.1 g pre-dissolved PVP. The reaction mixtures were brought to 220 ^oC for 20 minutes. The resulting products were centrifuged, washed with ethanol three times, and finally redispersed in ethanol for future use.

Synthesis of Au@CuS Core-Shell NPs. Au NPs with precisely controlled average particle sizes were synthesized following a previously reported protocol [54]. The as-synthesized Au NPs then served as the seeds to mediate the growth of CuS shells in EG to form Au@CuS core-shell NPs using $Cu(NO_3)_2$ and TU as the Cu and S sources, respectively, in the presence of polyvinylpyrrolidone (PVP) as the surface-capping ligands that kept the colloidal NPs from aggregation. In a typical procedure, 0.1 g of PVP was dissolved in 8 mL of EG, followed by the addition of various amounts of 0.1 M $Cu(NO_3)_2$ and 0.1 M TU. After 2 mL of colloidal Au seeds (108 μg mL^{-1} Au) were introduced, the reaction mixtures were brought to boiling and kept at 197 ^oC for 40 minutes. The molar ratio of Cu:TU was kept at 1:3 and the relative amount of $Cu(NO_3)_2$ *vs.* Au was adjusted as needed to systematically tune the shell thickness. The resulting Au@CuS core-shell NPs were separated from the reaction mixtures through 3 cycles of centrifugation and redispersion in ethanol and were finally stored in ethanol for future use.

Synthesis of Au@$Cu_{1.8}$S Core-Shell NPs. Au@$Cu_{1,8}$S core-shell NPs were synthesized following a procedure similar to that of Au@CuS core-shell NPs except that

the molar ratio of Cu:TU was kept at 3:1 instead of 1:3. Briefly, $Cu(NO_3)_2$ and TU were mixed with Au NPs in EG containing 0.1 g PVP and the reactions were carried out at 197 ^oC for 10 minutes. The thickness of the $Cu_{1.8}S$ shells was adjusted by varying the relative amount of $Cu(NO_3)_2$ *vs.* Au. The resulting Au@$Cu_{1,8}S$ core-shell NPs were centrifuged and redispersed in ethanol 3 times and were finally stored in ethanol for future use.

Synthesis of Au@$Cu_{2-x}S$ Core-Shell NPs. Upon exposure of Au@$Cu_{1.8}S$ core-shell NPs to H_2O_2 in aqueous environment at room temperature, the digenite shells underwent a phase-transition process to evolve into non-stoichiometric $Cu_{2-x}S$ while still retaining the core-shell heteronanostructures. In a typical process, Au@$Cu_{1.8}S$ core-shell NPs were mixed with 0.3 mM H_2O_2 aqueous solution under ambient air. Aliquots of colloidal NPs at various reaction stages were quickly taken out, centrifuged, and finally redispersed in ethanol for further characterizations.

Photothermal Measurements. The photothermal performances of Au@CuS and Au@$Cu_{2-x}S$ core-shell NPs were evaluated by monitoring the temporal evolution of temperature of 2.0 mL aqueous suspensions of colloidal NPs in a quartz cuvette (1.0 cm × 1.0 cm × 4.5 cm) embedded in a styrofoam holder under continuous laser illumination using a digital thermocouple (Therma Waterproof Thermometer for Type K Thermocouples, Priggen Special Eletronic). The particle concentrations of various colloidal NPs were kept at 4.0×10^9 particles mL^{-1}, which was calculated based on the original concentration of the ~ 17 nm Au seeds used for the synthesis of various Au NPs and core-shell NPs. The light sources for excitations were continuous-wave diode lasers purchased from Lasever Inc. (Ningbo, Zhejiang, China) with the tunable power output in the range of 0-3.0 W and emission wavelengths at 445 nm (model no. LSR445SD), 638

nm (model no. LSR638CP8), and 980 nm (model no. LSR980NL). The laser beams were collimated with a 4 mm × 4 mm square cross-section and incident vertically from the top surface into the solution at an excitation power of 1.0 W for the photothermal measurements. After reaching the thermal equilibrium, the illumination laser was turned off and the colloidal solution was naturally cooled down to room temperature under ambient air. The temporal evolution of temperature was monitored over three cycles of photothermal heating and natural cooling processes.

Analysis of Photothermal Effect. The results of photothermal measurements performed on colloidal Au@CuS core-shell NPs were analyzed following a widely used thermophysical theoretical model.[60] The temperature change of the bulk solutions during cooling periods (see Figure 3.4E) was extracted to calculate the temporal evolution of the dimensionless thermodynamic driving force (θ) toward the thermal equilibrium of the system, which was defined by the following equation,

$$\theta \equiv \frac{T_{amb} - T}{T_{amb} - T_{\max}} \qquad \text{(Equation E2),}$$

where T_{amb} is the ambient temperature and T_{max} is the maximum temperature when reaching the thermal equilibrium under laser illumination. When the laser irradiation was switched off, at time (t) of 0, the initial θ is equal to 1. As the sample system began to cool down, the temperature dropped exponentially. The temperature evolution during the cooling process followed the exponential pattern better than that during photothermal heating due to less thermal gradients. The thermal equilibrium time constant (τ_s) could be obtained by fitting the experimental results using the following linear equation,

$$\ln(\theta) = -\frac{1}{\tau_s} \times t \qquad \text{(Equation E3).}$$

Because of the nonlinearity when logarithmic operand approached 0, the results of the first 500 s during the cooling process were extracted for the least squares curve fitting.

Considering the energy balance of the system, the relationships among the laser-induced heating of the NPs (Q_{NPs}), laser-induced heating of the solvent (Q_0), and external heat dissipation from the system to surroundings (Q_{ext}) could be described by the following equation,

$$\sum_i m_i C_{p,i} \frac{dT}{dt} = Q_{NPs} + Q_0 - Q_{ext} \qquad \text{(Equation E4)},$$

where m_i and $C_{p,i}$ are the mass and constant-pressure heat capacity of i^{th} component in the system. Our calculations were simplified by only considering the contribution of water (m_{water} = 2.0 g and $C_{p,water}$ = 4.184 J K^{-1} g^{-1}) while ignoring the negligible contribution from the NPs. Q_{NPs}, which rendered the light to heat conversion of the colloidal NPs, was related to the optical extinction at the incident wavelength (E_λ), the power of the excitation laser (P_{ex}), and conversion efficiency (ϕ) through the following equation,

$$Q_{NPs} = P_{ex}(1-10^{-E_\lambda})\phi \qquad \text{(Equation E5)}.$$

The values of E_λ were extracted from the extinction spectra of the NPs (Figure 3.4D). Q_{ext} was calculated using a simplified thermal convection and radiation model derived from the Newton's law of cooling[73]

$$Q_{ext} = hA(T - T_{amb}) \qquad \text{(Equation E6)},$$

where h is the heat transfer coefficient, A is the cross-section surface area of thermal convection of the solution to the air (the cross-section area of glass cuvette, 1.0 cm^{-2}). In this heat-transfer model, h is indicative of both the convective and radiative

thermal transport features of the system, encompassing the boundary layer thermodynamics, fluid motion of the solvent, and surface geometries. h is related to τ_s through

$$h = \frac{\sum_i m_i C_{p,i}}{A\tau_s} \qquad \text{(Equation E7).}$$

When the system reaches the thermal equilibrium, external heat flux (Q_{ext}) is equal to the total laser-induced heat generation from both the NPs and the solvent:

$$Q_{ext} = Q_{NPs} + Q_0 \qquad \text{(Equation E8).}$$

The values of Q_0 were calculated based on the temperature changes of the solvent containing no NPs upon laser illumination using the following equation,

$$Q_0 = h_{water} A(T_{max} - T_{amb}) \qquad \text{(Equation E9).}$$

Here h_{water} was calculated based on the τ_s values of pure water using Equation E7. Substituting the Q_{NPs} with (Q_{ext}-Q_0) in Equation E5, the photothermal conversion efficiency, ϕ, of the NPs could be calculated using the following equation,

$$\phi = \frac{Q_{NPs}}{P_{ex}(1-10^{-E_\lambda})} = \frac{hA(T_{max} - T_{amb}) - Q_0}{P_{ex}(1-10^{-E_\lambda})} \times 100\% \qquad \text{(Equation E10).}$$

Photocatalytic Mineralization of RhB. The reaction mixtures for the photocatalytic reactions were prepared by mixing colloidal Au@CuS or Au@$Cu_{2-x}S$ core-shell NPs with RhB in aqueous solutions at pH of 7.0 in a quartz cuvette (1.0 cm × 1.0 cm × 4.5 cm). The concentrations of colloidal NPs and RhB molecules in the reaction mixtures were ~ 1.0 x 10^9 particles mL^{-1} and 1.0 μM, respectively. The total volume of the reaction mixtures was kept at 2.0 mL. Prior to the laser irradiation, the dispersion was kept in dark with magnetic stir for 4 h to achieve a pre-established adsorption/desorption

equilibrium. After introduction of H_2O_2 (300 μM in the reaction mixture), the photocatalytic reactions were initiated upon illumination by an excitation laser. The reaction kinetics were systematically studied at various excitation powers in the range from 0 to 3.0 W and at three different excitation wavelengths (445, 638, and 980 nm). The collimated laser beams (4 mm x 4 mm square cross-section) were incident vertically from the top surface into the reaction mixtures. The reaction mixtures were kept under magnetic stir (200 rpm) and the cuvette was immersed in a large water bath (4 L in volume) during the entire process to facilitate the dissipation of photothermally generated heat. To monitor the reaction progress, the RhB molecules remaining in the solution were separated from the photocatalysts through centrifugation every 10 minutes during the reactions and the RhB concentration was quantified by UV-visible absorption spectroscopy using a Beckman coulter Du 640 spectrophotometer according to the absorbance at 553 nm (the characteristic absorption peak of RhB). The photocatalysts were then remixed with the remaining RB molecules and subject to further photocatalytic reactions upon exposure to the laser illumination. To test the photocatalytic durability, the photocatalysts were recycled through centrifugation after the photo-reactions proceeded for 20 min and then redispersed in 2 mL solution containing 1.0 μM RhB and 300 μM H_2O_2 for the next reaction cycle.

3.5 References

1. Comin, A.; Manna, L. New Materials for Tunable Plasmonic Colloidal Nanocrystals. *Chem. Soc. Rev.* **2014,** *43* (11), 3957-3975.

2. Naik, G. V.; Shalaev, V. M.; Boltasseva, A. Alternative Plasmonic Materials: Beyond Gold and Silver. *Adv. Mater.* **2013,** *25* (24), 3264-3294.

3. Jain, P. K.; Huang, X. H.; El-Sayed, I. H.; El-Sayed, M. A. Noble Metals on the Nanoscale: Optical and Photothermal Properties and Some Applications in Imaging, Sensing, Biology, and Medicine. *Acc. Chem. Res.* **2008,** *41* (12), 1578-1586.

4. Wang, H.; Brandl, D. W.; Nordlander, P.; Halas, N. J. Plasmonic Nanostructures: Artificial Molecules. *Acc. Chem. Res.* **2007,** *40* (1), 53-62.

5. Brongersma, M. L.; Halas, N. J.; Nordlander, P. Plasmon-Induced Hot Carrier Science and Technology. *Nat. Nanotech.* **2015,** *10* (1), 25-34.

6. Zhang, Y. C.; He, S.; Guo, W. X.; Hu, Y.; Huang, J. W.; Mulcahy, J. R.; Wei, W. D. Surface-Plasmon-Driven Hot Electron Photochemistry. *Chem. Rev.* **2018,** *118* (6), 2927-2954.

7. Kale, M. J.; Avanesian, T.; Christopher, P. Direct Photocatalysis by Plasmonic Nanostructures. *ACS Catal.* **2014,** *4* (1), 116-128.

8. Linic, S.; Aslam, U.; Boerigter, C.; Morabito, M. Photochemical Transformations on Plasmonic Metal Nanoparticles. *Nat. Mater.* **2015,** *14* (6), 567-576.

9. Mukherjee, S.; Libisch, F.; Large, N.; Neumann, O.; Brown, L. V.; Cheng, J.; Lassiter, J. B.; Carter, E. A.; Nordlander, P.; Halas, N. J. Hot Electrons Do the Impossible: Plasmon-Induced Dissociation of H_2 on Au. *Nano Lett.* **2013,** *13* (1), 240-247.

10. Lal, S.; Clare, S. E.; Halas, N. J., Nanoshell-Enabled Photothermal Cancer Therapy: Impending Clinical Impact. *Acc. Chem. Res.* **2008,** *41* (12), 1842-1851.

11. Xia, Y. N.; Li, W. Y.; Cobley, C. M.; Chen, J. Y.; Xia, X. H.; Zhang, Q.; Yang, M. X.; Cho, E. C.; Brown, P. K. Gold Nanocages: From Synthesis to Theranostic Applications. *Acc. Chem. Res.* **2011,** *44* (10), 914-924.

12. Huang, X. H.; Neretina, S.; El-Sayed, M. A. Gold Nanorods: From Synthesis and Properties to Biological and Biomedical Applications. *Adv. Mater.* **2009,** *21* (48), 4880-4910.

13. Zheng, T. T.; Li, G. G.; Zhou, F.; Wu, R.; Zhu, J. J.; Wang, H. Gold-Nanosponge-Based Multistimuli-Responsive Drug Vehicles for Targeted Chemo-Photothermal Therapy. *Adv. Mater.* **2016,** *28* (37), 8218-8226.

14. Zhao, Y.; Pan, H.; Lou, Y.; Qiu, X.; Zhu, J.; Burda, C. Plasmonic $Cu_{2-x}S$ Nanocrystals: Optical and Structural Properties of Copper-Deficient Copper(I) Sulfides. *J. Am. Chem. Soc.* **2009,** *131* (12), 4253-4261.

15. Luther, J. M.; Jain, P. K.; Ewers, T.; Alivisatos, A. P. Localized Surface Plasmon Resonances Arising from Free Carriers in Doped Quantum Dots. *Nat. Mater.* **2011,** *10* (5), 361-366.

16. Dorfs, D.; Härtling, T.; Miszta, K.; Bigall, N. C.; Kim, M. R.; Genovese, A.; Falqui, A.; Povia, M.; Manna, L. Reversible Tunability of the near-Infrared Valence Band Plasmon Resonance in $Cu_{2-x}Se$ Nanocrystals. *J. Am. Chem. Soc.* **2011,** *133* (29), 11175-11180.

17. Hsu, S.-W.; On, K.; Tao, A. R. Localized Surface Plasmon Resonances of Anisotropic Semiconductor Nanocrystals. *J. Am. Chem. Soc.* **2011,** *133* (47), 19072-19075.

18. Kriegel, I.; Jiang, C.; Rodríguez-Fernández, J.; Schaller, R. D.; Talapin, D. V.; da Como, E.; Feldmann, J. Tuning the Excitonic and Plasmonic Properties of Copper Chalcogenide Nanocrystals. *J. Am. Chem. Soc.* **2012,** *134* (3), 1583-1590.

19. Kriegel, I.; Rodríguez-Fernández, J.; Wisnet, A.; Zhang, H.; Waurisch, C.; Eychmüller, A.; Dubavik, A.; Govorov, A. O.; Feldmann, J. Shedding Light on Vacancy-Doped Copper Chalcogenides: Shape-Controlled Synthesis, Optical Properties, and Modeling of Copper Telluride Nanocrystals with Near-Infrared Plasmon Resonances. *ACS Nano* **2013,** *7* (5), 4367-4377.

20. Xie, Y.; Carbone, L.; Nobile, C.; Grillo, V.; D'Agostino, S.; Della Sala, F.; Giannini, C.; Altamura, D.; Oelsner, C.; Kryschi, C.; Cozzoli, P. D. Metallic-Like Stoichiometric Copper Sulfide Nanocrystals: Phase- and Shape-Selective Synthesis, Near-Infrared Surface Plasmon Resonance Properties, and Their Modeling. *ACS Nano* **2013,** *7* (8), 7352-7369.

21. Li, W.; Zamani, R.; Rivera Gil, P.; Pelaz, B.; Ibáñez, M.; Cadavid, D.; Shavel, A.; Alvarez-Puebla, R. A.; Parak, W. J.; Arbiol, J.; Cabot, A. Cute Nanocrystals: Shape and Size Control, Plasmonic Properties, and Use as SERS Probes and Photothermal Agents. *J. Am. Chem. Soc.* **2013,** *135* (19), 7098-7101.

22. Liu, Y.; Liu, M.; Swihart, M. T. Plasmonic Copper Sulfide-Based Materials: A Brief Introduction to Their Synthesis, Doping, Alloying, and Applications. *J. Phys. Chem. C* **2017,** *121* (25), 13435-13447.

23. Cordova-Castro, R. M.; Casavola, M.; van Schilfgaarde, M.; Krasavin, A. V.; Green, M. A.; Richards, D.; Zayats, A. V. Anisotropic Plasmonic Cus Nanocrystals as a Natural Electronic Material with Hyperbolic Optical Dispersion. *ACS Nano* **2019,** *13* (6), 6550-6560.

24. Manthiram, K.; Alivisatos, A. P. Tunable Localized Surface Plasmon Resonances in Tungsten Oxide Nanocrystals. *J. Am. Chem. Soc.* **2012,** *134* (9), 3995-3998.

25. Ye, X. C.; Fei, J. Y.; Diroll, B. T.; Paik, T.; Murray, C. B. Expanding the Spectral Tunability of Plasmonic Resonances in Doped Metal-Oxide Nanocrystals through Cooperative Cation-Anion Codoping. *J. Am. Chem. Soc.* **2014,** *136* (33), 11680-11686.

26. Liu, Z.; Zhong, Y.; Shafei, I.; Jeong, S.; Wang, L.; Nguyen, H. T.; Sun, C.-J.; Li, T.; Chen, J.; Chen, L.; Losovyj, Y.; Gao, X.; Ma, W.; Ye, X. Broadband Tunable Mid-Infrared Plasmon Resonances in Cadmium Oxide Nanocrystals Induced by Size-Dependent Nonstoichiometry. *Nano Lett.* **2020,** *20* (4), 2821-2828.

27. Gordon, T. R.; Paik, T.; Klein, D. R.; Naik, G. V.; Caglayan, H.; Boltasseva, A.; Murray, C. B., Shape-Dependent Plasmonic Response and Directed Self-Assembly in a New Semiconductor Building Block, Indium-Doped Cadmium Oxide (ICO). *Nano Lett.* **2013,** *13* (6), 2857-2863.

28. Manna, G.; Bose, R.; Pradhan, N. Semiconducting and Plasmonic Copper Phosphide Platelets. *Angew. Chem. Int. Ed.* **2013,** *52* (26), 6762-6766.

29. Palomaki, P. K. B.; Miller, E. M.; Neale, N. R. Control of Plasmonic and Interband Transitions in Colloidal Indium Nitride Nanocrystals. *J. Am. Chem. Soc.* **2013,** *135* (38), 14142-14150.

30. Agrawal, A.; Cho, S. H.; Zandi, O.; Ghosh, S.; Johns, R. W.; Milliron, D. J. Localized Surface Plasmon Resonance in Semiconductor Nanocrystals. *Chem. Rev.* **2018,** *118* (6), 3121-3207.

31. Liu, X.; Swihart, M. T. Heavily-Doped Colloidal Semiconductor and Metal Oxide Nanocrystals: An Emerging New Class of Plasmonic Nanomaterials. *Chem. Soc. Rev.* **2014,** *43* (11), 3908-3920.

32. Cui, J. B.; Li, Y. J.; Liu, L.; Chen, L.; Xu, J.; Ma, J. W.; Fang, G.; Zhu, E. B.; Wu, H.; Zhao, L. X.; Wang, L. Y.; Huang, Y. Near-Infrared Plasmonic-Enhanced Solar Energy Harvest for Highly Efficient Photocatalytic Reactions. *Nano Lett.* **2015,** *15* (10), 6295-6301.

33. Gan, X. Y.; Keller, E. L.; Warkentin, C. L.; Crawford, S. E.; Frontiera, R. R.; Millstone, J. E. Plasmon-Enhanced Chemical Conversion Using Copper Selenide Nanoparticles. *Nano Lett.* **2019,** *19* (4), 2384-2388.

34. Huang, X. J.; Zhang, W. L.; Guan, G. Q.; Song, G. S.; Zou, R. J.; Hu, J. Q. Design and Functionalization of the Nir-Responsive Photothermal Semiconductor Nanomaterials for Cancer Theranostics. *Acc. Chem. Res.* **2017,** *50* (10), 2529-2538.

35. Wang, S. H.; Riedinger, A.; Li, H. B.; Fu, C. H.; Liu, H. Y.; Li, L. L.; Liu, T. L.; Tan, L. F.; Barthel, M. J.; Pugliese, G.; De Donato, F.; D'Abbusco, M. S.; Meng, X. W.; Manna, L.; Meng, H.; Pellegrino, T. Plasmonic Copper Sulfide Nanocrystals Exhibiting near-Infrared Photothermal and Photodynamic Therapeutic Effects. *ACS Nano* **2015,** *9* (2), 1788-1800.

36. Hessel, C. M.; Pattani, V. P.; Rasch, M.; Panthani, M. G.; Koo, B.; Tunnell, J. W.; Korgel, B. A. Copper Selenide Nanocrystals for Photothermal Therapy. *Nano Lett.* **2011,** *11* (6), 2560-2566.

37. Liu, Y.; Zhu, D. W.; Hu, Y. J.; Swihart, M. T.; Wei, W. Controlled Synthesis of $Cu_{2-X}Se$ Nanoparticles as Near-Infrared Photothermal Agents and Irradiation Wavelength Dependence of Their Photothermal Conversion Efficiency. *Langmuir* **2018,** *34* (46), 13905-13909.

38. Zhou, M.; Zhang, R.; Huang, M. A.; Lu, W.; Song, S. L.; Melancon, M. P.; Tian, M.; Liang, D.; Li, C. A Chelator-Free Multifunctional Cu-64 CuS Nanoparticle Platform for Simultaneous Micro-Pet/Ct Imaging and Photothermal Ablation Therapy. *J. Am. Chem. Soc.* **2010,** *132* (43), 15351-15358.

39. Liu, X.; Lee, C.; Law, W. C.; Zhu, D. W.; Liu, M. X.; Jeon, M.; Kim, J.; Prasad, P. N.; Kim, C.; Swihart, M. T. Au-$Cu_{2-x}Se$ Heterodimer Nanoparticles with Broad Localized Surface Plasmon Resonance as Contrast Agents for Deep Tissue Imaging. *Nano Lett.* **2013,** *13* (9), 4333-4339.

40. Ma, L.; Chen, Y. L.; Yang, X.; Li, H. X.; Ding, S. J.; Hou, H. Y.; Xiong, L.; Qin, P. L.; Chen, X. B. Growth Behavior of Au/$Cu_{2-x}S$ Hybrids and Their Plasmon-Enhanced Dual-Functional Catalytic Activity. *CrystEngComm* **2019,** *21* (37), 5610-5617.

41. Jiang, R. B.; Li, B. X.; Fang, C. H.; Wang, J. F. Metal/Semiconductor Hybrid Nanostructures for Plasmon-Enhanced Applications. *Adv. Mater.* **2014,** *26* (31), 5274-5309.

42. Zhu, H.; Wang, Y.; Chen, C.; Ma, M. R.; Zeng, J. F.; Li, S. Z.; Xia, Y. S.; Gao, M. Y. Monodisperse Dual Plasmonic Au@$Cu_{2-X}E$ (E=S, Se) Core@Shell Supraparticles: Aqueous Fabrication, Multimodal Imaging, and Tumor Therapy at in Vivo Level. *ACS Nano* **2017,** *11* (8), 8273-8281.

43. Kim, Y.; Park, K. Y.; Jang, D. M.; Song, Y. M.; Kim, H. S.; Cho, Y. J.; Myung, Y.; Park, J. Synthesis of Au-Cu_2S Core-Shell Nanocrystals and Their Photocatalytic and Electrocatalytic Activity. *J. Phys. Chem. C* **2010,** *114* (50), 22141-22146.

44. Muhammed, M. A. H.; Doblinger, M.; Rodriguez-Fernandez, J. Switching Plasmons: Gold Nanorod-Copper Chalcogenide Core-Shell Nanoparticle Clusters with Selectable Metal/Semiconductor Nir Plasmon Resonances. *J. Am. Chem. Soc.* **2015,** *137* (36), 11666-11677.

45. Ji, M. W.; Xu, M.; Zhang, W.; Yang, Z. Z.; Huang, L.; Liu, J. J.; Zhang, Y.; Gu, L.; Yu, Y. X.; Hao, W. C.; An, P. F.; Zheng, L. R.; Zhu, H. S.; Zhang, J. T. Structurally Well-Defined Au@$Cu_{2-x}S$ Core-Shell Nanocrystals for Improved Cancer Treatment Based on Enhanced Photothermal Efficiency. *Adv. Mater.* **2016,** *28* (16), 3094-3101.

46. Sun, Z. H.; Yang, Z.; Zhou, J. H.; Yeung, M. H.; Ni, W. H.; Wu, H. K.; Wang, J. F. A General Approach to the Synthesis of Gold-Metal Sulfide Core-Shell and Heterostructures. *Angew. Chem. Int. Ed.* **2009,** *48* (16), 2881-2885.

47. Chang, Y.; Cheng, Y.; Feng, Y. L.; Jian, H.; Wang, L.; Ma, X. M.; Li, X.; Zhang, H. Y. Resonance Energy Transfer-Promoted Photothermal and Photodynamic Performance of Gold- Copper Sulfide Yolk-Shell Nanoparticles for Chemophototherapy of Cancer. *Nano Lett.* **2018,** *18* (2), 886-897.

48. Ding, X. G.; Liow, C. H.; Zhang, M. X.; Huang, R. J.; Li, C. Y.; Shen, H.; Liu, M. Y.; Zou, Y.; Gao, N.; Zhang, Z. J.; Li, Y. G.; Wang, Q. B.; Li, S. Z.; Jiang, J. Surface Plasmon Resonance Enhanced Light Absorption and Photothermal Therapy in the Second Near-Infrared Window. *J. Am. Chem. Soc.* **2014,** *136* (44), 15684-15693.

49. Huo, D.; Cao, Z. M.; Li, J.; Xie, M. H.; Tao, J.; Xia, Y. N. Seed-Mediated Growth of Au Nanospheres into Hexagonal Stars and the Emergence of a Hexagonal Close-Packed Phase. *Nano Lett.* **2019,** *19* (5), 3115-3121.

50. Fan, Z. X.; Huang, X.; Chen, Y.; Huang, W.; Zhang, H. Facile Synthesis of Gold Nanomaterials with Unusual Crystal Structures. *Nat. Protoc.* **2017,** *12* (11), 2367-2378.

51. Coughlan, C.; Ibanez, M.; Dobrozhan, O.; Singh, A.; Cabot, A.; Ryan, K. M. Compound Copper Chalcogenide Nanocrystals. *Chem. Rev.* **2017,** *117* (9), 5865-6109.

52. Zhang, J. T.; Tang, Y.; Lee, K.; Min, O. Y. Nonepitaxial Growth of Hybrid Core-Shell Nanostructures with Large Lattice Mismatches. *Science* **2010,** *327* (5973), 1634-1638.

53. Lv, Q.; Min, H.; Duan, D. B.; Fang, W.; Pan, G. M.; Shen, A. G.; Wang, Q. Q.; Nie, G. J.; Hu, J. M. Total Aqueous Synthesis of Au@$Cu_{2-x}S$ Core-Shell Nanoparticles for in vitro and in vivo SERS/PA Imaging-Guided Photothermal Cancer Therapy. *Adv. Healthc. Mater.* **2019,** *8* (2), 1801257.

54. Zhang, P.; Li, Y.; Wang, D.; Xia, H. High-Yield Production of Uniform Gold Nanoparticles with Sizes from 31 to 577 nm via One-Pot Seeded Growth and Size-Dependent Sers Property. *Part. Part. Syst. Charact.* **2016,** *33* (12), 924-932.

55. Morales-García, A.; Soares, A. L.; Dos Santos, E. C.; de Abreu, H. A.; Duarte, H. A. First-Principles Calculations and Electron Density Topological Analysis of Covellite (CuS). *J. Phys. Chem. A* **2014,** *118* (31), 5823-5831.

56. Adhikari, S.; Sarkar, D.; Madras, G. Hierarchical Design of Cus Architectures for Visible Light Photocatalysis of 4-Chlorophenol. *ACS Omega* **2017,** *2* (7), 4009-4021.

57. Basu, M.; Sinha, A. K.; Pradhan, M.; Sarkar, S.; Negishi, Y.; Govind; Pal, T. Evolution of Hierarchical Hexagonal Stacked Plates of CuS from Liquid-Liquid Interface and Its Photocatalytic Application for Oxidative Degradation of Different Dyes under Indoor Lighting. *Environ. Sci. Technol.* **2010,** *44* (16), 6313-6318.

58. Xu, Q.; Huang, B.; Zhao, Y. F.; Yan, Y. F.; Noufi, R.; Wei, S. H. Crystal and Electronic Structures of Cuxs Solar Cell Absorbers. *Appl. Phys. Lett.* **2012,** *100* (6), 061906.

59. Martinson, A. B. F.; Riha, S. C.; Thimsen, E.; Elam, J. W.; Pellin, M. J. Structural, Optical, and Electronic Stability of Copper Sulfide Thin Films Grown by Atomic Layer Deposition. *Energy Environ. Sci.* **2013,** *6* (6), 1868-1878.

60. Roper, D. K.; Ahn, W.; Hoepfner, M. Microscale Heat Transfer Transduced by Surface Plasmon Resonant Gold Nanoparticles. *J. Phys. Chem. C* **2007,** *111* (9), 3636-3641.

61. Hoffmann, M. R.; Martin, S. T.; Choi, W. Y.; Bahnemann, D. W. Environmental Applications of Semiconductor Photocatalysis. *Chem. Rev.* **1995,** *95* (1), 69-96.

62. Xu, Y.; Schoonen, M. A. A. The Absolute Energy Positions of Conduction and Valence Bands of Selected Semiconducting Minerals. *Am. Mineral.* **2000,** *85* (3-4), 543-556.

63. Yang, Z. J.; Cao, Y.; Li, J.; Lu, M. M.; Jiang, Z. K.; Hu, X. Y. Smart CuS Nanoparticles as Peroxidase Mimetics for the Design of Novel Label-Free Chemiluminescent Immunoassay. *ACS Appl. Mater. Interfaces* **2016,** *8* (19), 12031-12038.

64. He, W. W.; Jia, H. M.; Li, X. X.; Lei, Y.; Li, J.; Zhao, H. X.; Mi, L. W.; Zhang, L. Z.; Zheng, Z. Understanding the Formation of CuS Concave Superstructures with Peroxidase-Like Activity. *Nanoscale* **2012,** *4* (11), 3501-3506.

65. Zhang, Q. F.; Zhou, Y. D.; Fu, X. Q.; Villarreal, E.; Sun, L. C.; Zou, S. L.; Wang, H. Photothermal Effect, Local Field Dependence, and Charge Carrier Relaying Species in

Plasmon-Driven Photocatalysis: A Case Study of Aerobic Nitrothiophenol Coupling Reaction. *J. Phys. Chem. C* **2019,** *123* (43), 26695-26704.

66. Baffou, G.; Bordacchini, I.; Baldi, A.; Quidant, R. Simple Experimental Procedures to Distinguish Photothermal from Hot-Carrier Processes in Plasmonics. *Light-Sci. Appl.* **2020,** *9* (1), 108.

67. Jain, P. K. Taking the Heat Off of Plasmonic Chemistry. *J. Phys. Chem. C* **2019,** *123* (40), 24347-24351.

68. Zhao, J.; Nguyen, S. C.; Ye, R.; Ye, B. H.; Weller, H.; Somorjai, G. A.; Alivisatos, A. P.; Toste, F. D. A Comparison of Photocatalytic Activities of Gold Nanoparticles Following Plasmonic and Interband Excitation and a Strategy for Harnessing Interband Hot Carriers for Solution Phase Photocatalysis. *ACS Cent. Sci.* **2017,** *3* (5), 482-488.

69. Fu, X. Q.; Li, G. G.; Villarreal, E.; Wang, H. Hot Carriers in Action: Multimodal Photocatalysis on Au@SnO_2 Core-Shell Nanoparticles. *Nanoscale* **2019,** *11* (15), 7324-7334.

70. Goldstein, S.; Aschengrau, D.; Diamant, Y.; Rabani, J. Photolysis of Aqueous H_2O_2: Quantum Yield and Applications for Polychromatic UV Actinometry in Photoreactors. *Environ. Sci. Technol.* **2007,** *41* (21), 7486-7490.

71. Zhang, P.; Li, Y.; Wang, D.; Xia, H. High–Yield Production of Uniform Gold Nanoparticles with Sizes from 31 to 577 nm *via* One-Pot Seeded Growth and Size-Dependent SERS Property. *Part. Part. Syst. Charact.* **2016,** *33* (12), 924-932.

72. Johnson, P. B.; Christy, R. W. Optical Constants of the Noble Metals. *Phys. Rev. B* **1972,** *6* (12), 4370-4379.

73. Incropera, F. P.; DeWitt, D. P.; Incropera, F. P. *Fundamentals of Heat and Mass Transfer*. 2nd Ed.; Wiley: New York, 1985.

CHAPTER 4

COVELLITE NANODISKS AND DIGENITE NANORINGS

4.1 Introduction

Covellite (CuS) have long been regarded as a unique member in the transition metal chalcogenide (TMC) family. Considerable concentration of free charge carriers to support localized surface plasmonic resonance (LSPR)[1-2], rich varieties of colloidal nanocrystals, and excellent chemical robustness render CuS an ideal plasmonic TMC materials that have garnered widespread interests in near-infrared photothermal treatment therapy (PTT)[3-6], photocatalysis[7-9], and energy storage[10-12]. In addition, the intrinsic anisotropy of its crystal structure, arising from the hexagonally closest packed (hcp) crystalline unit cells, conveniently predisposing covellite to adopt antisymmetric growth pattern, presenting CuS to be prospective plasmonic two-dimensional TMD materials[13-15]. Unlike the commonly studied two-dimensional TMD materials MoE_2 or WE_2 (E = S, Se, or Te)[16-20], layered CuS nanomaterials have not only van der waals interactions, but greater tendency to form stronger S-S covalent bonds between layers[21], critically distinguishing CuS from the conventional class of naturally two-dimensional TMD materials, of which vertical thickness is typically sub-10 nm and lateral width is in the scale of micrometers. Rarely researched on, this fundamental uniqueness of the bonding mechanics at the atomic configuration level opens the door for definite tunability on the dimensionality (lateral width, vertical thickness) or planar surface morphology (smoothness, Moirë patterns) of layered CuS nanomaterials. Achieving this tunability makes possible the exploration on geometry dependence of their unfamiliar hyperbolic LSPR features and planar surface distribution of work functions.

As anisotropic plasmonic semiconductor, CuS nanomaterials are known to exhibit a hybrid of two different electromagnetic responses along the in-plane and out-of-plane

orientation with respect to the incident light, when the real part of the dielectric permittivity is positive in one direction (dielectric permittivity) and negative in another (metallic permittivity)[22-23]. This so-called 'optical hyperbolic dispersion' feature of CuS provides valuable insights with regard to the sources of LSPR: In the visible spectrum range, CuS is naturally hyperbolic; In the infrared region, anisotropic LSPR dominates as both in-plane and out-of-plane dielectric permittivities become increasingly negative[22]. It was therefore reasonable to conclude that the geometrical parameters such as shapes and dimensionality of CuS with anisotropic nanostructures can be engineered for its LSPR modulation[15, 22, 24-25]. One important parameter is the aspect ratio, defined as ratio of the lateral width (longitudinal length) to the vertical thickness (transverse length)[15, 24].

Besides manipulating geometrical parameters to modulate LSPR of copper sulfide nanomaterials, adjusting the concentration levels of free charge carriers via changing the crystalline phases of copper sulfide would also impact the LSPR[2, 26-27]. As a self-doped semiconductor, copper sulfide showed plasmonic responses through free hole oscillation in its valence band that was induced by doping levels of Cu vacancies[1, 28].

Herein, we have employed a multi-step temperature-programmed heating-up approach to synthesize anisotropic CuS nanodisks with well-controlled dimensionality and planar surface morphology, as well as have prompted covellite-to-digenite crystalline phase transformation to produce porous digenite ($Cu_{1.8}S$) nanorings. Both of these two-dimensional copper sulfide nanomaterials retained broad LSPR responses that covered a great portion of the infrared spectrum. We have consolidated the previous discoveries that aspect ratios would progressively red-shift the LSPR peaks of anisotropic copper sulfide materials by obtaining larger aspect ratio values and extended coverage by LSPR

on the infrared spectrum in our work. Furthermore, inspired by works on the unique planar surface patterns (surface defects[29-32], Moirë patterns[33-34], Moirë excitons[35-36], etc.) on two-dimensional materials, we have further portrayed the topography and surface work functions distribution of the synthesized CuS nanodisks and $Cu_{1.8}S$ nanoring using surface-sensitive atomic force microscopy (AFM) and kelvin probe force microscopy (KPFM) to better understand the correlations of planar morphology to their electronic properties.

4.2 Results and Discussion

Covellite Nanodisks and Growth Mechanism. As shown in the schematic illustration of the hexagonal unit cell of covellite in Figure 4.1A adapted from Ref. 21, the atomic coordination is either CuS_3 trigonal planes (Cu(1) and S(1)) or CuS_4 tetrahedrals (Cu(2) and S(2)), in which S(2) was covalently bonded with another S(2). This unique interplanar bond is in obvious contrast to that of the conventional two-dimensional TMD nanomaterials, of which each layers of atomic unit cells of TMD were stacked together through only van der waals forces between each chalcogen atoms at the edge,[37] resulting in significant surface energy difference between the planar facets (001) and edge facets (100) or (010) of the atomic units. In the atomic units of CuS, stronger interplanar S-S covalent bonding substantially lessened the gap of surface energy of planar facets and edge facets. Therefore, its anisotropic growth propensity suffered the comparison to conventional two-dimensional TMD nanomaterials, but also foreshadowing the possibility for dimensionality tunability.

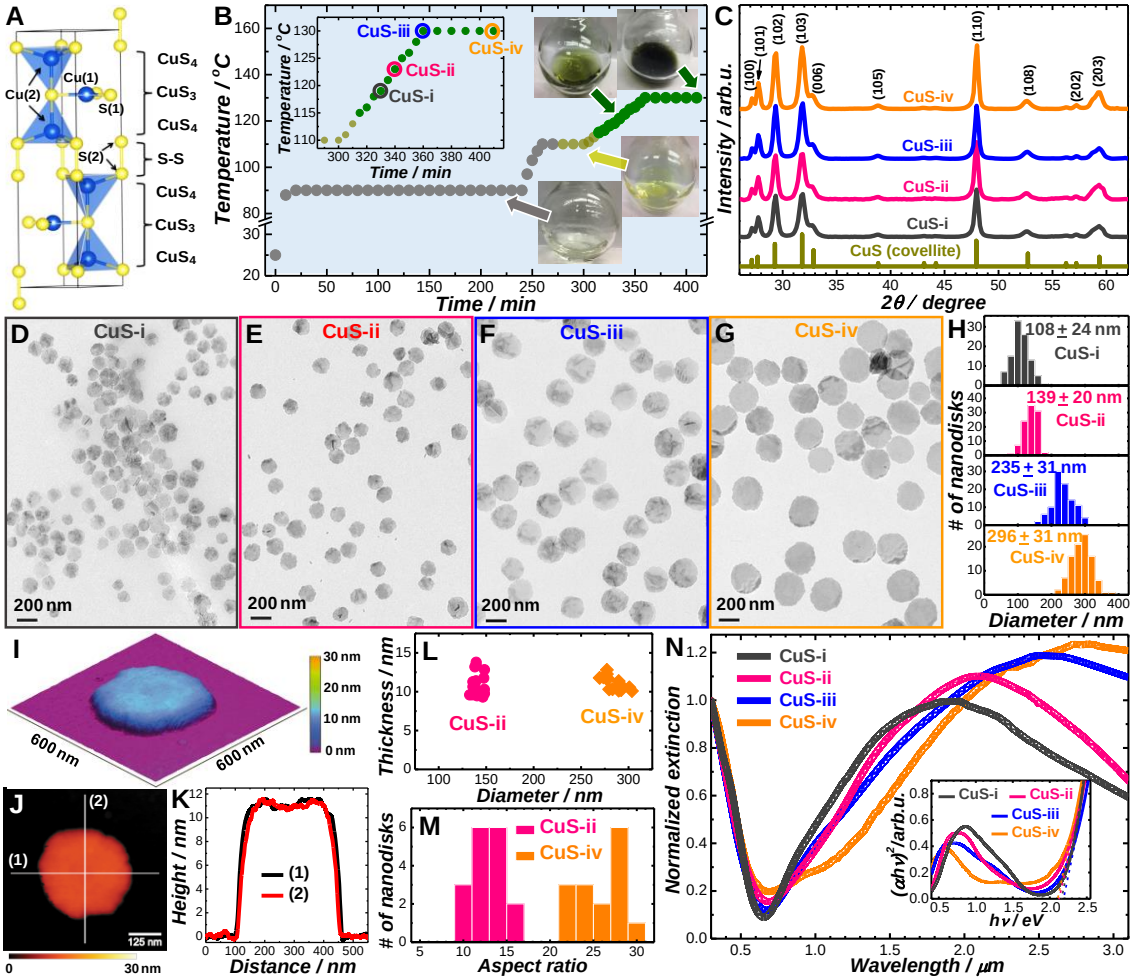

Figure 4.1. (A) Ball-and-stick schematic illustration of unit cell of covellite (CuS), adapted from Ref. 21. (B) Pre-programmed heating profile for CuS nanodisks synthesis. Particles formed at different stages of the reaction were labelled as CuS-i, CuS-ii, CuS-iii, and CuS-iv, respectively, in the inset. (C) PXRD patterns of CuS-i, CuS-ii, CuS-iii, and CuS-iv. Standard pattern (covellite, JCPDS 6-464) of CuS were shown as reference. TEM images of (D) CuS-i, (E) CuS-ii, (F) CuS-iii, and (G) CuS-iv. (H) CuS nanodisk lateral diameter distributions of CuS-i, CuS-ii, CuS-iii, and CuS-iv. The distribution of particles was obtained from 100 particles in TEM images. (I) Three-dimensional and (J) two-dimensional AFM topography of individual particle of CuS-iv nanodisks. (K) Topography profile line-scanned by AFM probe along the direction (1) and (2) specified in (J). (L) Dimensionality and (M) aspect ratio distributions of CuS-ii and CuS-iv. (N) Extinction spectra of CuS-i, CuS-ii, CuS-iii, and CuS-iv. Spectra were normalized at 1.0 at 300 nm. The Tauc plots were shown in the inset.

To enhance the anisotropy of CuS, it is of vital importance to outline a synthetic scheme designed to increase the surface energy gaps and thus reinforce selectivity of horizontal growth along the higher-surface-energy edge facets over vertical growth. To

that end, we purposefully designed a multi-step heating-up synthetic approach to optimize the PVP-directed colloidal synthesis of CuS nanodisks, as shown in the heating profile in Figure 4.1B. Color evolutions of the synthesized colloidal CuS nanocrystals were illustrated by photographs of the reaction solutions taken at different stages of the reaction. The yellow-to-green transition signified the colloidal nucleation process from [Cu-S] complexes to the crystalized CuS nanoparticles. Particles formed after 330^{th} min (CuS-i), 340^{th} min (CuS-ii), 360^{th} min (CuS-iii), and 410^{th} min (CuS-iv) were collected and labelled. Crystalline phases of covellite were verified by powder X-ray diffraction (PXRD) patterns shown in Figure 4.1C. It is evident that the PXRD peaks of all CuS nanodisks agreed well with standard patterns of covellite (JCPDS 6-464) and showed no detectable lattice distortion. Morphological changes were characterized using transmission electron microscopy (TEM) in Figure 4.1D-4.1G. Uniform plate-shaped CuS nanostructures were observed and evolved to grow larger in lateral diameters as the reaction progressed. According to the size distribution histograms in Figure 4.1H, obtained from the TEM images in Figure 4.1D-4.1G, particle diameters of each CuS nanodisks were determined to be 108 nm (CuS-i), 139 nm (CuS-ii), 235 nm (CuS-iii), and 296 nm (CuS-iv). The lattice spacing of (110) plane of CuS-iv nanodisks was determined to be about 0.19 nm.

To have a more thorough portrait of the shape and morphology of CuS nanodisks, AFM was used to provide a high-resolution imaging that reveals more information on the planar surface of CuS nanodisks. As illustrated in the ‘sculptural’ three-dimensional AFM topography in Figure 4.1I, the layered anisotropic feature of CuS-iv nanodisks was put on a more straightforward display. Line-scanned along direction (1) and (2) specified

in the two-dimensional AFM topography in Figure 4.1J, the Pt/Ir AFM probes measured the vertical thickness of CuS-iv nanodisks to be about 10 nm through amplitude modulated (AM) scanning mode, as shown in the topography profile in Figure 4.1K. Also was conducted on CuS-ii nanodisks, AFM determined the vertical thickness of CuS-ii nanodisks to be comparable to that of CuS-iv nanodisks, as illustrated in Figure 4.1L, suggesting the crystalline growth took place overwhelmingly on the lateral direction following this temperature-programmed heating-up profile. Unsurprisingly, the aspect ratios of each CuS nanodisks were increasing as the crystalline growth progressed. The aspect ratio was quantitively determined for CuS-ii nanodisks and CuS-iv nanodisks in Figure 4.1M. Heavily hinged on the aspect ratios, the hyperbolic LSPR feature of CuS nanodisks underwent substantial red-shift of their LSPR peak position when the aspect ratio was increased, as shown in Figure 4.1N. It is worth noting that despite apparent peak-shift of LSPR, the direct band gaps of every CuS nanodisks remained virtually unchanged and were extrapolated to be about 2.2 eV along their respective Tauc plots in the inset of Figure 4.1N.

The multi-step heating-up profile in Figure 4.1B was designed as such to strengthen the anisotropic growth and maintain a smooth planar surface with 10-nm thickness, or roughly 6 covellite unit cells (lattice constant of covellite is about 1.634 nm along z-axis, per JCPDS 6-486), of CuS nanodisks. Mainly, two aspects of synthesis parameters were deliberated: Equilibrating the coordination of PVP, Cu^{2+}, and S^{2-} ions in the early stage of the reaction and slow heating-up to direct the nucleated CuS atoms to grow onto the higher-surface-energy edge facets.

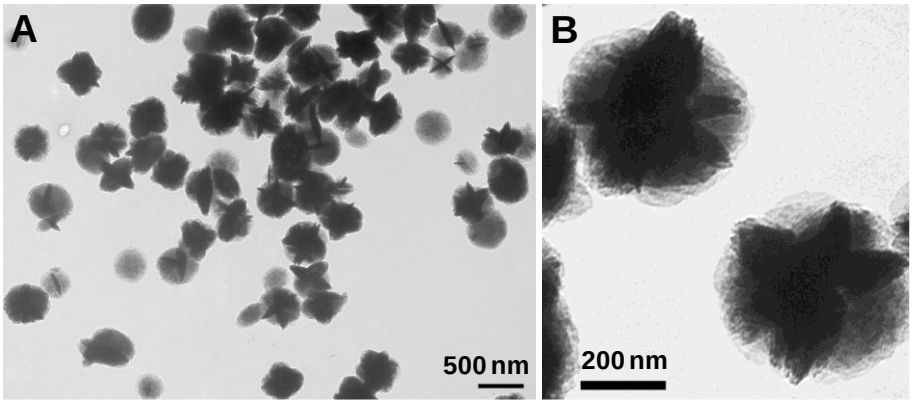

Figure 4.2. TEM images of synthesized CuS nanoparticles without the presence of PVP of both (A) low and (B) high magnification.

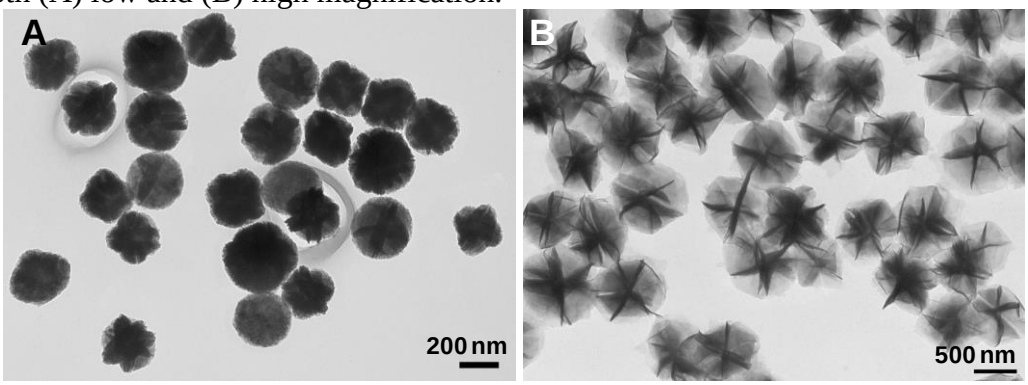

Figure 4.3. TEM images of synthesized superstructures CuS nanoparticles (A) with the application of magnetic stirring of 300 rpm and (B) with the application of magnetic stirring of 300 rpm and 6 times the PVP presented.

It has been well-established that nanocrystal growth tends to proceed in pathway that would minimize the overall surface energies and be dominated by the crystalline facets with the lowest energy[20, 37-39]. However, in principle, non-equilibrium shapes are often produced through numerous means to navigate the growth to deviate from equilibrium shapes. A popular one of those means is the use of organic ligands to modify surface energy and change the energetic landscape for nanocrystal growth[20, 40-42]. As a frequently used surface surfactant in the solution-phase colloidal nanoparticle synthesis, PVP is known to play a critical role in directing the growth of CuS nanoparticles owing to its strong coordination with the Cu^{2+} ions, mild reduction through its electron-rich

hydroxyl terminal group, and surface passivation to avoid particle agglomeration[9, 43-45]. As demonstrated in Figure 4.2A, without the presence of PVP, the synthesized CuS nanoparticles exhibited high polydispersity as irregular shapes of CuS nanoparticles were formed. It is worth noting that the edges of these synthesized CuS nanoparticles were very rough and uneven, as observed in Figure 4.2B, suggesting poor controllability over the growth rate of synthesized CuS nanoparticles. When magnetic stirring was applied to the reaction, PVP coordination was accelerated and strengthened, but its adsorption selectivity was undermined, disrupting the anisotropic growth. As shown in Figure 4.3A, multi-crystalline flower-like superstructures with higher symmetry and comprised of multiple plate-shaped CuS building units clustered together were formed. Upon excessively increasing the amount of PVP in the reaction, not only more superstructures of CuS nanoparticles were formed, but the thickness of each CuS plate units became seemingly thinner, as shown in Figure 4.3B. It therefore can be concluded that PVP assisted the formation of plate-shaped layered CuS nanostructures through modifying the surface energies and favoring the growth along the high-energy edge facet of (100) or (010) planes. However, it was also evident that PVP in excessive quantity will tremendously facilitate the growth of the multi-crystalline superstructures of CuS nanoparticles, which can be regarded as the thermodynamic preference (equilibrium shape) in this synthesis route involving PVP. Consequently, to facilitate anisotropic growth of single-crystalline CuS, maneuvering reaction parameters to deviate the nanocrystal growth from the equilibrium pathway and produce kinetically-trapped plate-shaped CuS nanodisks was instrumental.

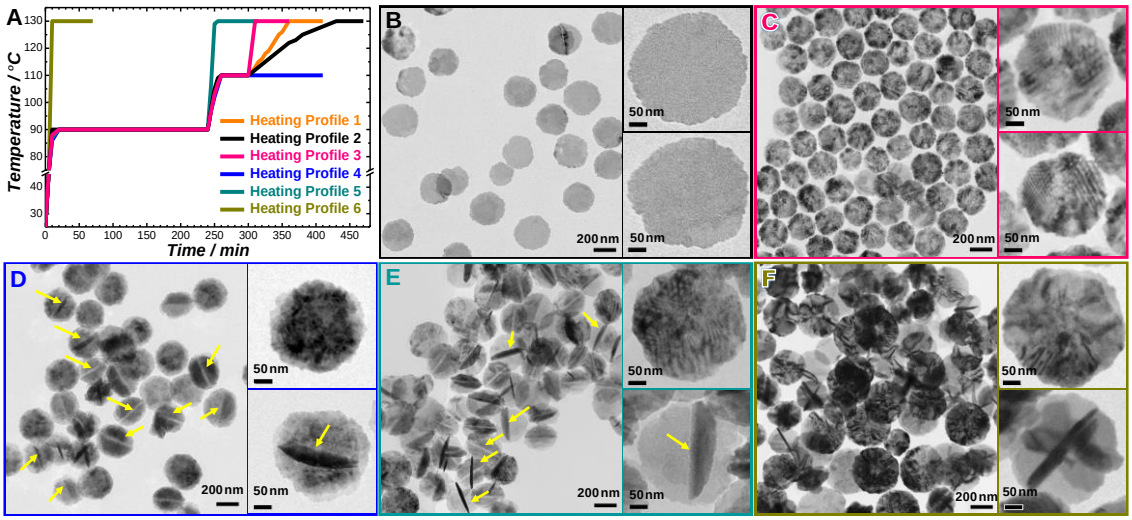

Figure 4.4. (A) Various heating-up profiles for covellite nanodisks synthesis. TEM images of particles formed at the end of (B) heating profile 2, (C) heating profile 3, (D) heating profile 4, (E) heating profile 5, and (F) heating profile 6. Individual particles were shown in the insets.

In Figure 4.4A, different heating-up routes were designed. TEM images of CuS nanoparticles formed at the end of each heating profiles (Excluding main heating profile, heating profile 1) were shown in Figure 4.4B-F (Heating profile 2 in Figure 4.4B, heating profile 3 in Figure 4.4C, heating profile 4 in Figure 4.4D, heating profile 5 in Figure 4.4E, and heating profile 6 in Figure 4.4F). When a direct and rapid heating-up profile was used (heating profile 6), highly polydisperse CuS nanoparticles were formed, as both two-dimensional plate-shaped CuS nanodisks and multi-crystalline superstructures of CuS nanoparticles were observed, demonstrated in the single-particle TEM images in the inset of Figure 4.4E. It is worth noting that the polydispersity of CuS nanoparticles formed at the end of heating profile 6 largely resembled that of the CuS nanoparticles synthesized without PVP (Figure 4.2): Both batches contained plethora of multi-crystalline superstructures of CuS nanoparticles and irregular shapes of CuS nanoparticles with insufficient controllability of both of its lateral diameter and vertical

thickness. It can be seen as PVP is no longer effective in the reaction condition of fast growth rate in heating profile 6.

To fully take advantage of the impact of PVP in directing plate-shaped CuS nanoparticle synthesis, we implemented a 4-hour low-temperature heating at 90 °C in the early stage of the synthesis, entailed in the heating profiles 1-5. In this period, two major processes took place: Cumulation of complexation of Cu^{2+} and S^{2-} ions released from their respective precursor sources and PVP coordination with the incremental [Cu-S] complexes in the reaction. The synthesis was maintained at the low temperature for extended period of time to allow full equilibration of molecular coordination of PVP, Cu^{2+} and S^{2-} ions and avoid premature crystallization of CuS nanoparticles. Afterwards, reaction was brought to higher temperatures to provide essential thermal input to overcome the kinetic barrier and trigger crystallization as the concentration of supersaturated PVP-coordinated CuS monomers in the solution reached minimum nucleation threshold. When another fast heating-up to 130 °C was adopted at the end of 4-hour low-temperature heating at 90 °C (heating profile 5), the polydispersity of synthesized CuS nanoparticles, as indicated in Figure 4.4E, was seemingly lower than that of the CuS nanoparticles synthesized following heating profile 6, but superstructures of multi-plate CuS nanoparticles sill presented in large amounts, marked with yellow arrows. When heating up to 120 °C and allowing reaction to proceed to completion at this temperature (heating profile 4), roughened planar surface of the plate-shaped CuS nanodisks was observed in Figure 4.4D, as well as persistent superstructures of CuS nanoparticles.

Formation of multi-crystalline superstructures of CuS nanoparticles was due to the energetically preferred heterogeneous nucleation of CuS plates to grow onto the nucleated CuS nanoparticles, instead of homogenous self-nucleation of single crystalline CuS plates. Additional thermal elevation was necessitated as higher temperature would induce more self-nucleation than heterogeneous nucleation of CuS plates. When a rapid heating-up to 130 °C was adopted after heating at 90 °C and 110 °C (heating profile 3), monodisperse CuS nanodisks were obtained, with minimal presence of multi-crystalline superstructures of CuS nanoparticles, as presented in the TEM images in Figure 4.4C. However, the planar surface of the synthesized CuS nanodisks were visibly roughened, possibly because of higher growth rate arising from the fast heating-up from 110 °C to 130 °C. It is reasonable to believe that heavy PVP-coordination in the solution would reduce the nucleation and growth rate of CuS monomers, thus allowing the pace of temperature elevation to have a bigger impact on manipulating the nucleation and growth rate. Consequently, when a slow heating-up (about 0.15 ^{o}C/min) from 110 °C to 130 °C was adopted (heating profile 2), selectivity of high-energy edge facets growth over low-energy planar facets growth was enhanced. Therefore, monodisperse CuS nanodisks with smooth and unroughened planar surface was synthesized, as shown in Figure 4.4B. The lateral diameter of the CuS nanodisks obtained following heating profile 2 was similar to that of the CuS nanodisks synthesized from heating profile 1 (with a slow heating-up rate of 0.33 ^{o}C/min), but slightly larger than that of the CuS nanodisks obtained from heating profile 2. This further proved that fast growth rate unsettled the effect of ligand adsorption and favored the low-energy planar surface growth (vertical growth) over high-energy edge surface growth (horizontal growth) of CuS nanodisks.

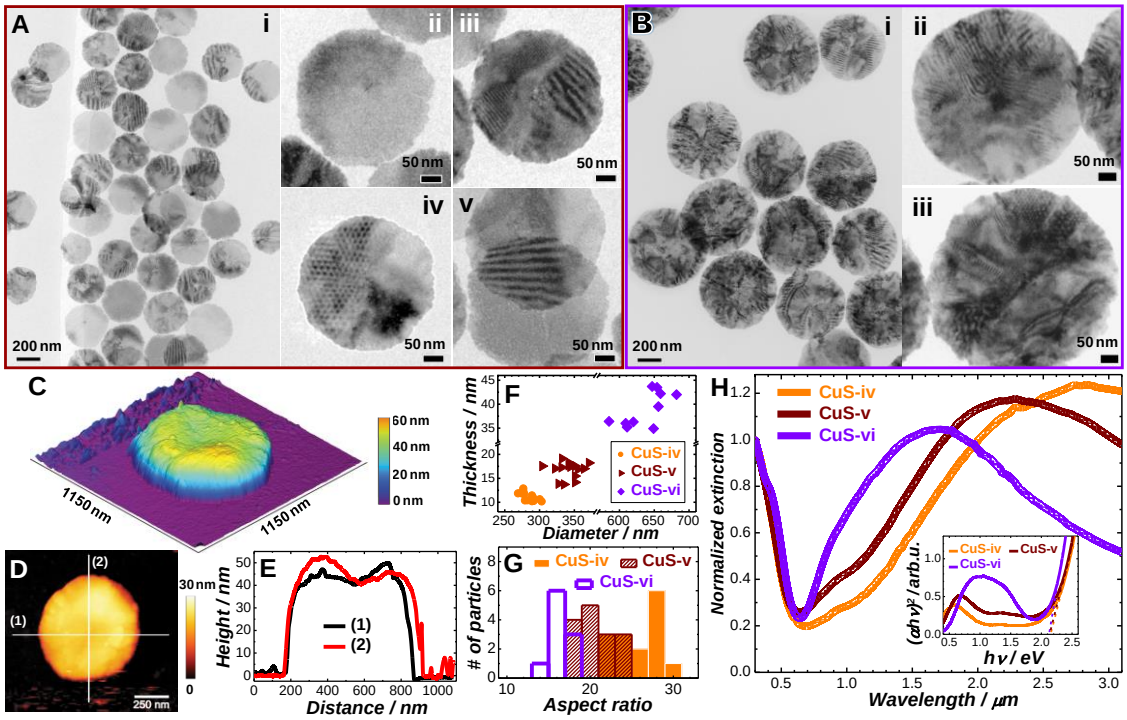

Figure 4.5. (A-i) TEM image of CuS-v nanodisks. Individual particles were shown in the panels (ii-v). (B-i) TEM image of CuS-iv nanodisks. Individual particles were shown in the panels (ii-iii). (C) Three-dimensional and (D) two-dimensional AFM topography of individual particle of CuS-iv nanodisks. (E) Topography profile line-scanned by AFM probe along the direction (1) and (2) specified in (D). (F) Dimensionality and (G) aspect ratio distributions of CuS-iv, CuS-v, and CuS-vi. (H) Extinction spectra of CuS-iv, CuS-v, and CuS-vi. Spectra were normalized at 1.0 at 300 nm. The Tauc plots were shown in the inset.

To modulate dimensionality, CuS nanodisks with larger lateral diameters and vertical thickness were synthesized following the heating profile with a slightly increased concentration of initial precursors of copper and sulfur. Similarly, plate-shaped CuS nanodisks (CuS-v) were produced, shown in Figure 4.5A-i. It is worth remarking that for CuS-v, while some nanodisks with a smooth planar surface (Figure 4.5A-ii), others displayed visible Moirë patterns, as shown in the single-particle TEM images in Figure 4.5A-iii, -iv, and -v. Moirë patterns occurred when multiple layered crystalline structures

stacked together in a mismatched orientation angles and created superimposed lattice periodicity[33-34].

To further boost the production of Moirë patterns, more layers of CuS plates were stacked together in order to generate more superimposition. Larger and thicker CuS-vi nanodisks were synthesized via seeded re-growth method that employed CuS-v nanodisks as the seed, of which more CuS atoms were grown onto both the planar surface and edges, as shown in Figure 4.5B-i. In Figure 4.5B-ii and Figure 4.5B-iii, it is obvious that CuS-vi nanodisks exhibited immense amounts of Moirë patterns on their planar surface.

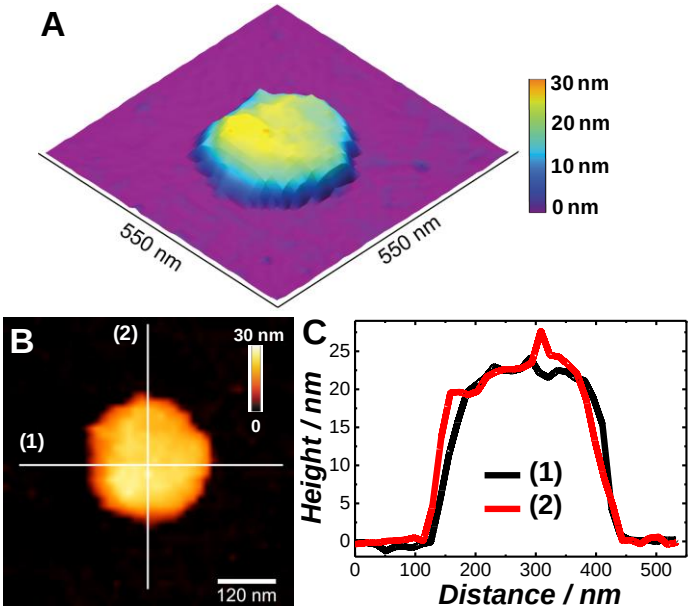

Figure 4.6. (A) Three-dimensional and (B) two-dimensional AFM topography of CuS-v nanodisks. (C) Topography profile line-scanned by AFM probe along the direction (1) and (2) specified in (B).

The three-dimensional and two-dimensional AFM topography of CuS-v nanodisks were shown in Figure 4.6A and Figure 4.6B, respectively. Based on the resulting AFM topography profile in Figure 4.6C, CuS-v nanodisks is estimated to be

about 20 nm in thickness. In Figure 4.5C and 4.5D, three-dimensional and two-dimensional AFM topography of CuS-vi nanodisks were presented, showing an even more roughened and coarsening planar surface of the nanodisks. The line-scanned topography profile in Figure 4.5E determined the thickness of CuS-v nanodisks to be roughly 40 to 45 nm. The lateral diameters of CuS-iv, CuS-v, and CuS-vi nanodisks were determined to be 296 nm, 381 nm, and 598 nm, respectively. Vertical thickness and lateral diameters of CuS-iv, CuS-v, and CuS-vi nanodisks were recorded in Figure 4.5F, showing an increasing trend of both lateral diameter and vertical thickness. Yet, in Figure 4.5G, a decreasing trend of aspect ratios were observed for CuS-iv, CuS-v, and CuS-vi nanodisks. Because of this, LSPR peaks progressively blue-shifted from the nanodisks with higher aspect ratio to nanodisks with lower aspect ratio, as shown in the extinction spectra in Figure 4.5H. Noticeably, the energy band gap remained largely aligned for all CuS nanodisks at about 2.2 eV based on the Tauc plots in the inset.

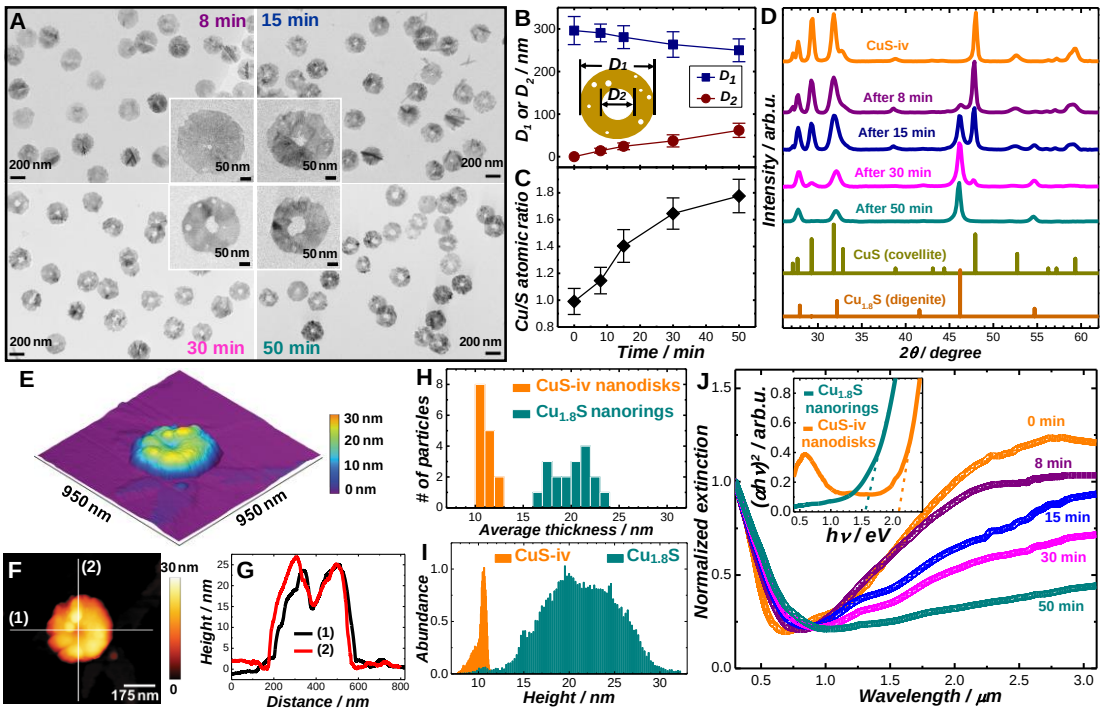

Figure 4.7. (A) TEM images of $Cu_{1.8}S$ nanorings formed at different stages of the covellite-to-digenite phase transformation reaction. Evolutions of (B) inner (D_2) and outer (D_1) diameters, (C) Cu-to-S atomic ratios, and (D) PXRD patterns of particles $Cu_{1.8}S$ nanorings. Standard PXRD patterns of CuS (covellite, JCPDS 6-464) and $Cu_{1.8}S$ (digenite, JCPDS 04-0784) were shown for reference. (E) Three-dimensional and (F) two-dimensional AFM topography of individual particle of $Cu_{1.8}S$ nanorings formed at the conclusion of covellite-to-digenite phase transformation reaction. (G) Topography profile line-scanned by AFM probe along the direction (1) and (2) specified in the (F). (H) Vertical thickness and (I) feedback signal-based pixel distributions of AFM topographies of CuS-iv nanodisks and of $Cu_{1.8}S$ nanorings. Distributions were obtained from 15 particles in AFM topographies. (J) Evolutions of extinction spectra. Spectra were normalized at 1.0 at 300 nm. The Tauc plots were shown in the inset.

Digenite Nanorings. $Cu_{1.8}S$ nanorings were synthesized in TEG upon covellite-to-digenite phase transformation of CuS-iv nanodisks. Under the reducing environment of TEG at a mildly high temperature of 180 ^oC, CuS-vi nanodisks underwent crystalline structural rearrangement from hexagonal covellite phase to cubic digenite phase through reduction of Cu^{2+} to Cu^{+} and sulfur removal via dissolution. This crystalline reconstruction in turn translated to morphology changes of the nanodisks. As indicated in the TEM images of the aliquots obtained after 8^{th}, 15^{th}, 30^{th}, and 50^{th} minute of the phase transformation reaction in Figure 4.7A, the planar surface became seemingly thickening and pores started to emerge and grow in sizes through Ostwald ripening. The growing pores sizes on the planar surface suggested that the bond cleavage likely were initiated at the Cu-S bonds within each layer units, since Cu-S bond is weaker than S-S bond[21]. The evolution of obtained outer (D_1) and inner (D_2) diameters of the plate-shaped nanorings throughout the transformation reaction was shown in Figure 4.7B, indicating a shrinking nanodisks diameter and expanding pores size on the planar surface. Evolution of Cu-to-S atomic ratios was also obtained using EDX in Figure 4.7C, demonstrating a 1.0 Cu-to-S atomic ratios change to nearly 1.8 at the conclusion of the phase transformation reaction.

PXRD patterns gradually progressed from covellite of the starting CuS-iv nanodisks to cubic digenite after 50 minutes of transformation reaction, as indicated in Figure 4.7D.

In Figure 4.7E and 4.7F, three-dimensional and two-dimensional AFM topography of $Cu_{1.8}S$ nanorings were displayed, respectively. The coarsening nature of the planar surface was observed. Topography profile was recorded in Figure 4.7G. The dip in the center of the line-scanned profile corresponded to the pores of the nanorings. Particle distribution of vertical thickness of both CuS-iv nanodisks and $Cu_{1.8}S$ nanorings was recorded in Figure 4.7H, implying about 5-10 nm surface roughening taken place from phase transformation reaction of CuS-iv nanodisks to $Cu_{1.8}S$ nanorings. If converted to the pixels of feedback signals of AFM scanning and normalized at the most frequent vertical thickness (height), the particle distribution in Figure 4.7H became pixel distribution in Figure 4.7I. It was worth noting that the distribution of $Cu_{1.8}S$ nanorings became seemingly broadening in comparison to that of CuS-iv nanodisks, another evidence of planar surface roughening.

Upon increasing Cu contents in the unit cells, LSPR responses of CuS-iv nanodisks weakened due to smaller concentration of Cu vacancies. As observed in Figure 4.7J, LSPR signals progressively dwindled as the covellite-to-digenite phase transformation proceeded. The electronic band structures underwent rearrangement as well. As indicated in the Tauc plots in the inset of Figure 4J, the band gap energy fell from 2.2 eV for CuS to about 1.5 eV for $Cu_{1.8}S$. This energy band reconstructing therefore has noneligible implication on the planar surface work function distributions of both CuS nanodisks and $Cu_{1.8}S$ nanorings.

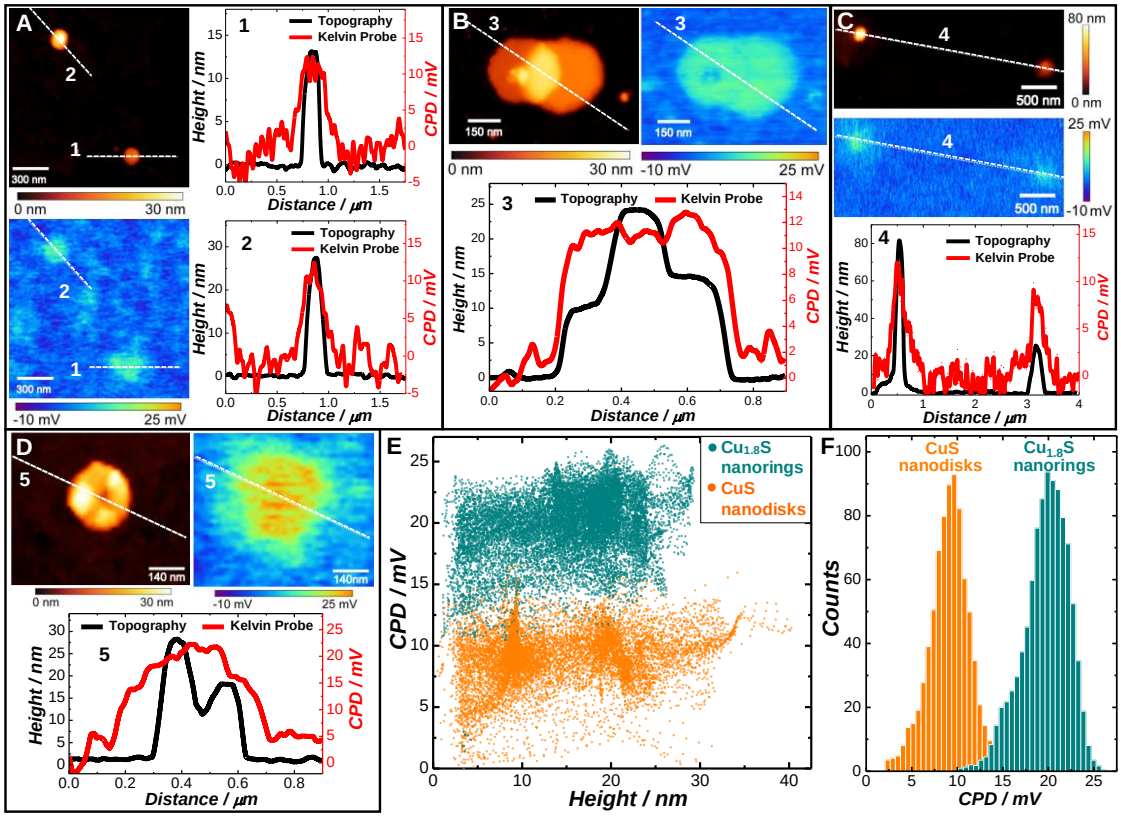

Figure 4.8. Two-dimensional ATM topographies, CPD imaging maps and topography versus CPD profiles of (A) CuS-iv nanodisks and CuS-v nanodisks, (B) two overlayed adjacent particles of CuS-iv nanodisks, (C) two particles of CuS-vi nanodisks, and (D) $Cu_{1.8}S$ nanorings. (E) feedback signal-based pixel CPD distributions and (F) their histograms of CuS nanodisks and $Cu_{1.8}S$ nanorings.

Surface Work Function Distribution. To gain understanding on the impact of planar surface morphology exerted on the electronic properties of CuS nanodisk and $Cu_{1.8}S$ nanorings, KPFM was used to measure the contact potential difference (CPD) between the probe tip and analyte sample that illustrates the work functions of the sample.

It has been suggested that Moirë patterns on two-dimensional materials were able to trap excitons at its local potential minimal and therefore create the so-called Moirë

potentials[33, 46]. To investigate the impact of Moirë patterns might had on altering the surface potentials when unexcited, KPFM measurements were performed on the Moirë patterns-free CuS-iv (Line scan 1) and CuS-vi (Line scan 2) nanodisks that included a large portion of nanodisks particle with Moirë patterns on their planar surface, as shown in Figure 4.8A. It can be seen that with different vertical thickness (vertical height detected), these two nanodisks had comparable CPD values around 11 mV. In the case of two adjacent CuS-iv nanodisks that assembled in an overlayed stacking pattern as shown in Figure 4.8B, line-scanned profile 3 revealed that CPD signals maintained an unaffected value, or insignificantly fluctuated when across nanodisks interfaces. In Figure 4.8C, CuS-v and Moirë patterns-plagued CuS-vi nanodisks were scanned together in line-scanned profile 4 to yield a similar result: CPD values very marginally changed despite the presence of Moirë patterns on their planar surface. However, for $Cu_{1.8}S$ nanorings, the topography and CPD profile (Line scan 5) demonstrated a different CPD value. In Figure 4.8D, as the line-scanned topography profile depicted the dip at the center of $Cu_{1.8}S$ nanoring, the CPD profile indicated a higher CPD value at about 20 mV, almost doubling that of CuS nanodisks.

Therefore, CPD distributions on 20 particles each for both $Cu_{1.8}S$ nanorings and CuS nanodisks were sketched: Feedback signals of CPD by KPFM in pixel with respect to their corresponding vertical height detected by AFM probe were obtained in Figure 4.8E; Histogram of counts of the pixels were constructed in Figure 4.8F. Based on the graphs, it was unequivocal that crystalline phases dictated CPD overwhelmingly, as opposed to vertical height. To interpret this, the electronic band restructuring upon covellite-to-digenite phase transformation drastically changed the intrinsic work

functions of the layered copper sulfide nanomaterials, when the planar surface morphology and assembling patterns delivered inconsequential influence.

4.3 Conclusion

In our work, we have designed multi-step heating up profiles to synthesize anisotropic CuS nanodisks, with great controllability over their dimensionality and surface morphology. With the tunability of the aspect ratio of the synthesized CuS nanodisks and phase-transformed $Cu_{1.8}S$ nanorings varying from roughly 12 to 30, we have extended their shape-dependent hyperbolic LSPR deep into infrared region, peaked beyond 2600 nm. In addition to tuning the plasmonic properties of these anisotropic copper sulfide nanostructures, we also have characterized their surface work functions distribution, aided by surface-sensitive techniques AFM and KPFM. Stacking patterns such as Moirë patterns of CuS nanodisks arising from the superimposition of mismatched planar layers had marginal effect on the surface potentials, as opposed to the electronic band arrangement induced by phase transformation to $Cu_{1.8}S$ nanorings, putting into perspectives the impacts surface features and crystalline phases have on the intrinsic work functions. However, future works can be done to uncover more opto-electronic behaviors (ex. Moirë excitons, Moirë hyperbolic plamons, superconductivity, etc.) on the surface of two-dimensional plasmonic copper sulfide nanomaterials. This work aimed not only to provide useful insights and basis for synthesis of anisotropic nanostructures, but also shed light on the structure-property relationship on the nanophotonic, and optoelectronic applications of such materials.

4.4 Experiments and Materials

Chemicals and Materials. Copper nitrate hydrate ($Cu(NO_3)_2 \cdot 3H_2O$), ethylene glycol (EG), thiourea (TU), polyvinylpyrrolidone (PVP, average molecular weight of 58,000) and tetraethylene glycol (TEG) were purchased from Alfa Aesar. All reagents received were used without further purification. Ultrapure Milli-Q water (18.2 Ω) was used for all experiments.

Characterizations. The transmission electron microscopy (TEM) images were obtained using a Hitachi H-7800 transmission electron microscope, operated at an accelerating voltage of 120 kV. Samples for TEM measurement were dispersed in ethanol and drop-dried on 300 mesh carbon-coated Cu grids (Electron Microscopy Science Inc.). The scanning electron microscopy (SEM) images and energy dispersive spectroscopy (EDS) measurements were conducted using a Zeiss Ultraplus thermal field emission scanning electron microscope. An EDS unit attached to the microscope was used to quantify the Cu and S stoichiometries in the samples. Atomic ratios were quantified based on the relative area of the Cu Lα and S Kα peaks in the EDS spectra. Samples for SEM and EDS measurements were dispersed in ethanol and drop-dried on silicon wafers. Powder X-ray diffraction (PXRD) patterns were collected on a SAXSLab Ganesha at the South Carolina Collaborative (Cu Kα = 1.5405 Å). To characterize the broad band of plasmon resonance of the CuS nanodisks and $Cu_{1.8}S$ nanorings, optical extinction spectra were collected on glass-supported NPs using Cary 5000 UV/vis/NIR spectrophotometer in the wavelength range 300-3300 nm. Samples were drop-dried on glass cover. Raman spectra were acquired on a Bayspec Nomadic confocal Raman

microscopy built on an Olympus BX51 microscope. A 785 nm continuous wave diode laser was used for illumination. The high-resolution TEM (HRTEM) images were obtained using a JEOL JEM-2100 transmission electron microscope operated at an accelerating voltage of 200 kV. Atomic force microscopy (AFM) topographies were constructed using. Contact potential difference (CPD) imaging were obtained using Kelvin probe force microscopy (KPFM).

Synthesis of CuS-iv and CuS-v nanodisks. Both CuS-iv and CuS-v nanodisks were synthesized following the multi-step heating-up protocol outlined in Figure 4.1B. A slightly higher volume of source precursors was required for the synthesis of CuS-v nanodisks. Typically, without magnetic stirring, in a 8 mL of EG solution, first 0.1 g of PVP was added and dissolved completely, followed by addition of 0.4 mL (0.45 mL for CuS-v nanodisks) of 0.1 M $Cu(NO_3)_2 \cdot 3H_2O$ and 1.6 mL (1.8 mL for CuS-v nanodisks) of 0.1 M TU precursor solutions with a molar ratio of Cu:S fixed at 1:4. The solution was kept on temperature-controlled heating mantle to initially heat-up to and maintained at 90 ^oC for 4 hours, then slowly brought to 110 ^oC and kept for 40 mins when the solution started to become densely yellow in color. The pace of the next heating-up was therefore set at 0.33 ^oC/min to reach 130 ^oC in 1 hour. Finally, the solution was allowed to proceed to completion at 130 ^oC for another 50 mins. The produced colloidal particles were obtained through centrifugation-redispersion cycles with ethanol and were stored in ethanol for future uses.

Synthesis of CuS-vi nanodisks. In order to produce more CuS nanodisks with Morie patterns on their planar surface, CuS-vi nanodisks were synthesized via a seeded regrowth method using CuS-v nanodisks as the seed, on which heterogeneous growth

took place. In a typical 8 mL EG solution dissolved with 0.1 g of PVP, as-synthesis CuS-v nanodisks colloidal solution were first added, followed by addition of 0.2 mL of 0.1 M $Cu(NO_3)_2 \cdot 3H_2O$ and 0.8 mL of of 0.1 M TU precursor solutions with a molar ratio of Cu:S fixed at 1:4. The solution was kept on temperature-controlled heating mantle to initially heat-up to and maintained at 90 ^oC for 2 hours, then slowly brought to 110 ^oC and kept for 30 mins. The pace of the next heating-up was therefore set at 0.33 ^oC/min to reach 130 ^oC in 1 hour. Finally, the solution was allowed to proceed to completion at 130 ^oC for another 50 mins. The produced colloidal particles were obtained through centrifugation-redispersion cycles with ethanol and were stored in ethanol for future uses.

Synthesis of CuS Superstructures nanoparticles. With the application of magnetic stirring, multi-crystalline multi-plated CuS superstructures nanoparticles were obtained (Figure 4.3A). In a typical 8 mL EG solution dissolved with 0.1 g of PVP, 0.4 mL of 0.1 M $Cu(NO_3)_2 \cdot 3H_2O$ and 1.6 mL of of 0.1 M TU precursor solutions with a molar ratio of Cu:S fixed at 1:4. The solution was rapidly heated-up to and maintained at 130 ^oC for 90 mins. The produced colloidal particles were obtained through centrifugation-redispersion cycles with ethanol and were stored in ethanol for future uses. For the synthesis of CuS superstructures nanoparticles with thinner CuS plates units (Figure 4.3B), the amount of PVP dissolved in EG were changed from 0.1 g to 0.6 g.

Synthesis of $Cu_{1.8}S$ nanorings. The $Cu_{1.8}S$ nanorings were synthesized by inducing covellite-to-digenite phase transformation on CuS-iv nanodisks in a more reductive TEG. In a 10 mL TEG solution dissolved with 0.1 g of PVP, the as-synthesized CuS-iv nanodisks were added. The solution was therefore brought up to 180 ^oC. Aliquots of samples were taken after 8^{th}, 15^{th}, 30^{th}, and 50^{th} minute of reaction and washed through

centrifugation-redispersion cycles with ethanol. The colloidal products were finally stored in ethanol for future uses.

4.4 References

1. Luther, J. M.; Jain, P. K.; Ewers, T.; Alivisatos, A. P., Localized surface plasmon resonances arising from free carriers in doped quantum dots. *Nat. Mater.* **2011,** *10* (5), 361-366.

2. Zhao, Y. X.; Pan, H. C.; Lou, Y. B.; Qiu, X. F.; Zhu, J. J.; Burda, C., Plasmonic Cu2-xS Nanocrystals: Optical and Structural Properties of Copper-Deficient Copper(I) Sulfides. *J. Am. Chem. Soc.* **2009,** *131* (12), 4253-4261.

3. Bu, X. Y.; Zhou, D.; Li, J.; Zhang, X.; Zhang, K.; Zhang, H.; Yang, B., Copper Sulfide Self-Assembly Architectures with Improved Photothermal Performance. *Langmuir* **2014,** *30* (5), 1416-1423.

4. Tian, Q. W.; Tang, M. H.; Sun, Y. G.; Zou, R. J.; Chen, Z. G.; Zhu, M. F.; Yang, S. P.; Wang, J. L.; Wang, J. H.; Hu, J. Q., Hydrophilic Flower-Like CuS Superstructures as an Efficient 980 nm Laser-Driven Photothermal Agent for Ablation of Cancer Cells. *Adv. Mater.* **2011,** *23* (31), 3542-+.

5. Wang, S. H.; Riedinger, A.; Li, H. B.; Fu, C. H.; Liu, H. Y.; Li, L. L.; Liu, T. L.; Tan, L. F.; Barthel, M. J.; Pugliese, G.; De Donato, F.; D'Abbusco, M. S.; Meng, X. W.; Manna, L.; Meng, H.; Pellegrino, T., Plasmonic Copper Sulfide Nanocrystals Exhibiting Near-Infrared Photothermal and Photodynamic Therapeutic Effects. *ACS Nano* **2015,** *9* (2), 1788-1800.

6. Liu, X. J.; Li, B.; Fu, F. F.; Xu, K. B.; Zou, R. J.; Wang, Q.; Zhang, B. J.; Chen, Z. G.; Hu, J. Q., Facile synthesis of biocompatible cysteine-coated CuS nanoparticles with high photothermal conversion efficiency for cancer therapy. *Dalton Trans.* **2014,** *43* (30), 11709-11715.

7. Zhang, J.; Yu, J. G.; Zhang, Y. M.; Li, Q.; Gong, J. R., Visible Light Photocatalytic H-2-Production Activity of CuS/ZnS Porous Nanosheets Based on Photoinduced Interfacial Charge Transfer. *Nano Lett.* **2011,** *11* (11), 4774-4779.

8. Tanveer, M.; Cao, C. B.; Ali, Z.; Aslam, I.; Idrees, F.; Khan, W. S.; But, F. K.; Tahir, M.; Mahmood, N., Template free synthesis of CuS nanosheet-based hierarchical microspheres: an efficient natural light driven photocatalyst. *CrystEngComm* **2014,** *16* (24), 5290-5300.

9. Zhang, Y. Q.; Zhang, B. P.; Zhu, L. F., Monodisperse CuS nanodisks: low-temperature solvothermal synthesis and enhanced photocatalytic activity. *RSC Adv.* **2014,** *4* (103), 59185-59193.

10. Zhao, L.; Tao, F. Q.; Quan, Z.; Zhou, X. L.; Yuan, Y. H.; Hu, J. C., Bubble template synthesis of copper sulfide hollow spheres and their applications in lithium ion battery. *Mater. Lett.* **2012,** *68*, 28-31.

11. Hosseinpour, Z.; Scarpellini, A.; Najafishirtari, S.; Marras, S.; Colombo, M.; Alemi, A.; De Volder, M.; George, C.; Lesnyak, V., Morphology-Dependent Electrochemical Properties of CuS Hierarchical Superstructures. *ChemPhysChem* **2015,** *16* (16), 3418-3424.

12. Li, Q. W.; Xue, Y.; Zhu, Y. C.; Qian, Y. T., Facile Synthesis and Application of CuS Nanospheres in Aqueous and Organic Lithium Ion Batteries. *J. Nanosci. Nanotechnol.* **2013,** *13* (2), 1265-1269.

13. Gotsis, H. J.; Barnes, A. C.; Strange, P., Experimental and Theoretical Investigation of the Crystal-Structure of Cus. *J. Phys. Condens. Matter* **1992,** *4* (50), 10461-10468.

14. Coughlan, C.; Ibanez, M.; Dobrozhan, O.; Singh, A.; Cabot, A.; Ryan, K. M., Compound Copper Chalcogenide Nanocrystals. *Chem. Rev.* **2017,** *117* (9), 5865-6109.

15. Liu, M. X.; Xue, X. Z.; Ghosh, C.; Liu, X.; Liu, Y.; Furlani, E. P.; Swihart, M. T.; Prasad, P. N., Room-Temperature Synthesis of Covellite Nanoplatelets with Broadly Tunable Localized Surface Plasmon Resonance. *Chem. Mater.* **2015,** *27* (7), 2584-2590.

16. Zhang, K. A.; Zhang, T. N.; Cheng, G. H.; Li, T. X.; Wang, S. X.; Wei, W.; Zhou, X. H.; Yu, W. W.; Sun, Y.; Wang, P.; Zhang, D.; Zeng, C. G.; Wang, X. J.; Hu, W. D.; Fan, H. J.; Shen, G. Z.; Chen, X.; Duan, X. F.; Chang, K.; Dai, N., Interlayer Transition and Infrared Photodetection in Atomically Thin Type-II MoTe2/MoS2 van der Waals Heterostructures. *ACS Nano* **2016,** *10* (3), 3852-3858.

17. Gong, Y. J.; Lin, J. H.; Wang, X. L.; Shi, G.; Lei, S. D.; Lin, Z.; Zou, X. L.; Ye, G. L.; Vajtai, R.; Yakobson, B. I.; Terrones, H.; Terrones, M.; Tay, B. K.; Lou, J.; Pantelides, S. T.; Liu, Z.; Zhou, W.; Ajayan, P. M., Vertical and in-plane heterostructures from WS2/MoS2 monolayers. *Nat. Mater.* **2014,** *13* (12), 1135-1142.

18. Pan, B. J.; Zhang, K. A.; Ding, C. C.; Wu, Z.; Fan, Q. C.; Luo, T. Y.; Zhang, L. J.; Zou, C.; Huang, S. M., Universal Precise Growth of 2D Transition-Metal

Dichalcogenides in Vertical Direction. *ACS Appl. Mater. Interfaces* **2020,** *12* (31), 35337-35344.

19. Lee, C.; Yan, H.; Brus, L. E.; Heinz, T. F.; Hone, J.; Ryu, S., Anomalous Lattice Vibrations of Single- and Few-Layer MoS2. *ACS Nano* **2010,** *4* (5), 2695-2700.

20. Nasilowski, M.; Mahler, B.; Lhuillier, E.; Ithurria, S.; Dubertret, B., Two-Dimensional Colloidal Nanocrystals. *Chem. Rev.* **2016,** *116* (18), 10934-10982.

21. Morales-Garcia, A.; Soares, A. L.; Dos Santos, E. C.; de Abreu, H. A.; Duarte, H. A., First-Principles Calculations and Electron Density Topological Analysis of Covellite (CuS). *J. Phys. Chem. A* **2014,** *118* (31), 5823-5831.

22. Cordova-Castro, R. M.; Casavola, M.; van Schilfgaarde, M.; Krasavin, A. V.; Green, M. A.; Richards, D.; Zayats, A. V., Anisotropic Plasmonic CuS Nanocrystals as a Natural Electronic Material with Hyperbolic Optical Dispersion. *ACS Nano* **2019,** *13* (6), 6550-6560.

23. Drachev, V. P.; Podolskiy, V. A.; Kildishev, A. V., Hyperbolic metamaterials: new physics behind a classical problem. *Opt. Express* **2013,** *21* (12), 15048-15064.

24. Hsu, S. W.; Ngo, C.; Tao, A. R., Tunable and Directional Plasmonic Coupling within Semiconductor Nanodisk Assemblies. *Nano Lett.* **2014,** *14* (5), 2372-2380.

25. Hsu, S. W.; On, K.; Tao, A. R., Localized Surface Plasmon Resonances of Anisotropic Semiconductor Nanocrystals. *J. Am. Chem. Soc.* **2011,** *133* (47), 19072-19075.

26. Liu, L. G.; Zhong, H. Z.; Bai, Z. L.; Zhang, T.; Fu, W. P.; Shi, L. J.; Xie, H. Y.; Deng, L. G.; Zou, B. S., Controllable Transformation from Rhombohedral Cu1.8S

Nanocrystals to Hexagonal CuS Clusters: Phase- and Composition-Dependent Plasmonic Properties. *Chem. Mater.* **2013,** *25* (23), 4828-4834.

27. Kriegel, I.; Jiang, C. Y.; Rodriguez-Fernandez, J.; Schaller, R. D.; Talapin, D. V.; da Como, E.; Feldmann, J., Tuning the Excitonic and Plasmonic Properties of Copper Chalcogenide Nanocrystals. *J. Am. Chem. Soc.* **2012,** *134* (3), 1583-1590.

28. Sun, M. Q.; Fu, X. Q.; Chen, K. X.; Wang, H., Dual-Plasmonic Gold@Copper Sulfide Core-Shell Nanoparticles: Phase-Selective Synthesis and Multimodal Photothermal and Photocatalytic Behaviors. *ACS Appl. Mater. Interfaces* **2020,** *12* (41), 46146-46161.

29. Kim, S. Y.; Kim, J. H.; Lee, S.; Kwak, J.; Jo, Y.; Yoon, E.; Lee, G. D.; Lee, Z.; Kwon, S. Y., The impact of substrate surface defects on the properties of two-dimensional van der Waals heterostructures. *Nanoscale* **2018,** *10* (40), 19212-19219.

30. Kim, K.; Lee, Z.; Regan, W.; Kisielowski, C.; Crommie, M. F.; Zettl, A., Grain Boundary Mapping in Polycrystalline Graphene. *ACS Nano* **2011,** *5* (3), 2142-2146.

31. Hashimoto, A.; Suenaga, K.; Gloter, A.; Urita, K.; Iijima, S., Direct evidence for atomic defects in graphene layers. *Nature* **2004,** *430* (7002), 870-873.

32. Ago, H.; Fukamachi, S.; Endo, H.; Solis-Fernandez, P.; Yunus, R. M.; Uchida, Y.; Panchal, V.; Kazakova, O.; Tsuji, M., Visualization of Grain Structure and Boundaries of Polycrystalline Graphene and Two-Dimensional Materials by Epitaxial Growth of Transition Metal Dichalcogenides. *ACS Nano* **2016,** *10* (3), 3233-3240.

33. He, F.; Zhou, Y. J.; Ye, Z. F.; Cho, S. H.; Jeong, J.; Meng, X. H.; Wang, Y. G., Moire Patterns in 2D Materials: A Review. *ACS Nano* **2021,** *15* (4), 5944-5958.

34. Ryu, Y. K.; Frisenda, R.; Castellanos-Gomez, A., Superlattices based on van der Waals 2D materials. *Chem. Commun.* **2019,** *55* (77), 11498-11510.

35. Shimazaki, Y.; Schwartz, I.; Watanabe, K.; Taniguchi, T.; Kroner, M.; Imamoglu, A., Strongly correlated electrons and hybrid excitons in a moire heterostructure. *Nature* **2020,** *580* (7804), 472-+.

36. Jin, C. H.; Regan, E. C.; Yan, A. M.; Utama, M. I. B.; Wang, D. Q.; Zhao, S. H.; Qin, Y.; Yang, S. J.; Zheng, Z. R.; Shi, S. Y.; Watanabe, K.; Taniguchi, T.; Tongay, S.; Zettl, A.; Wang, F., Observation of moire excitons in WSe2/WS2 heterostructure superlattices. *Nature* **2019,** *567* (7746), 76-+.

37. Han, J. H.; Lee, S.; Cheon, J., Synthesis and structural transformations of colloidal 2D layered metal chalcogenide nanocrystals. *Chem. Soc. Rev.* **2013,** *42* (7), 2581-2591.

38. Wulff, G., On the question of speed of growth and dissolution of crystal surfaces. *Z. Krystallog.* **1901,** *34* (5/6), 449-530.

39. Barmparis, G. D.; Lodziana, Z.; Lopez, N.; Remediakis, I. N., Nanoparticle shapes by using Wulff constructions and first-principles calculations. *Beilstein J. Nanotechnol.* **2015,** *6*, 361-368.

40. Viswanath, B.; Kundu, P.; HaIder, A.; Ravishankar, N., Mechanistic Aspects of Shape Selection and Symmetry Breaking during Nanostructure Growth by Wet Chemical Methods. *J. Phys. Chem. C* **2009,** *113* (39), 16866-16883.

41. Peng, X. G.; Manna, L.; Yang, W. D.; Wickham, J.; Scher, E.; Kadavanich, A.; Alivisatos, A. P., Shape control of CdSe nanocrystals. *Nature* **2000,** *404* (6773), 59-61.

42. Milliron, D. J.; Hughes, S. M.; Cui, Y.; Manna, L.; Li, J. B.; Wang, L. W.; Alivisatos, A. P., Colloidal nanocrystal heterostructures with linear and branched topology. *Nature* **2004,** *430* (6996), 190-195.

43. Xiong, Y. J.; Washio, I.; Chen, J. Y.; Cai, H. G.; Li, Z. Y.; Xia, Y. N., Poly(vinyl pyrrolidone): A dual functional reductant and stabilizer for the facile synthesis of noble metal nanoplates in aqueous solutions. *Langmuir* **2006,** *22* (20), 8563-8570.

44. Qi, H.; Huang, J. F.; Cao, L. Y.; Wu, J. P.; Li, J. Y., Controlled synthesis and optical properties of doughnut-aggregated hollow sphere-like CuS. *Ceram. Int.* **2012,** *38* (8), 6659-6664.

45. Sun, S. D.; Li, P. J.; Liang, S. H.; Yang, Z. M., Diversified copper sulfide (Cu2-xS) micro-/nanostructures: a comprehensive review on synthesis, modifications and applications. *Nanoscale* **2017,** *9* (32), 11357-11404.

46. Geng, W. T.; Wang, V.; Liu, Y. C.; Ohno, T.; Nara, J., Moire Potential, Lattice Corrugation, and Band Gap Spatial Variation in a Twist-Free MoTe2/MoS2 Heterobilayer. *J. Phys. Chem. Lett.* **2020,** *11* (7), 2637-2646.

APPENDIX A

CUMULATIVE BIBLIOGRAPHY

- Agrawal, A.; Cho, S. H.; Zandi, O.; Ghosh, S.; Johns, R. W.; Milliron, D. J., Localized Surface Plasmon Resonance in Semiconductor Nanocrystals. *Chem. Rev.* **2018,** *118* (6), 3121-3207.
- Mayer, K. M.; Hafner, J. H., Localized Surface Plasmon Resonance Sensors. *Chem. Rev.* **2011,** *111* (6), 3828-3857.
- Jain, P. K.; Huang, X. H.; El-Sayed, I. H.; El-Sayed, M. A., Noble Metals on the Nanoscale: Optical and Photothermal Properties and Some Applications in Imaging, Sensing, Biology, and Medicine. *Acc. Chem. Res.* **2008,** *41* (12), 1578-1586.
- Coughlan, C.; Ibanez, M.; Dobrozhan, O.; Singh, A.; Cabot, A.; Ryan, K. M., Compound Copper Chalcogenide Nanocrystals. *Chem. Rev.* **2017,** *117* (9), 5865-6109.
- Mie, G., Articles on the optical characteristics of turbid tubes, especially colloidal metal solutions. *Ann. Phys.* **1908,** *25* (3), 377-445.
- Anderson, L. J. E.; Mayer, K. M.; Fraleigh, R. D.; Yang, Y.; Lee, S.; Hafner, J. H., Quantitative Measurements of Individual Gold Nanoparticle Scattering Cross Sections. *J. Phys. Chem. C* **2010,** *114* (25), 11127-11132.
- Drude, P., On the electron theory of metals. *Ann. Phys.* **1900,** *1* (3), 566-613.

- Giannini, V.; Fernandez-Dominguez, A. I.; Heck, S. C.; Maier, S. A., Plasmonic Nanoantennas: Fundamentals and Their Use in Controlling the Radiative Properties of Nanoemitters. *Chem. Rev.* **2011,** *111* (6), 3888-3912.
- Zhong, Y. J.; Malagari, S. D.; Hamilton, T.; Wasserman, D., Review of mid-infrared plasmonic materials. *J. Nanophotonics.* **2015,** *9*.
- Li, W. H.; Zamani, R.; Gil, P. R.; Pelaz, B.; Ibanez, M.; Cadavid, D.; Shavel, A.; Alvarez-Puebla, R. A.; Parak, W. J.; Arbiol, J.; Cabot, A., CuTe Nanocrystals: Shape and Size Control, Plasmonic Properties, and Use as SERS Probes and Photothermal Agents. *J. Am. Chem. Soc.* **2013,** *135* (19), 7098-7101.
- Jackson, J. B.; Halas, N. J., Surface-enhanced Raman scattering on tunable plasmonic nanoparticle substrates. *Proc. Natl. Acad. Sci. U.S.A.* **2004,** *101* (52), 17930-17935.
- Nikoobakht, B.; El-Sayed, M. A., Surface-enhanced Raman scattering studies on aggregated gold nanorods. *J. Phys. Chem. A* **2003,** *107* (18), 3372-3378.
- Wu, Y.; Wadia, C.; Ma, W. L.; Sadtler, B.; Alivisatos, A. P., Synthesis and photovoltaic application of copper(I) sulfide nanocrystals. *Nano Lett.* **2008,** *8* (8), 2551-2555.
- Kale, M. J.; Avanesian, T.; Christopher, P., Direct Photocatalysis by Plasmonic Nanostructures. *ACS Catal.* **2014,** *4* (1), 116-128.
- Boerigter, C.; Aslam, U.; Linic, S., Mechanism of Charge Transfer from Plasmonic Nanostructures to Chemically Attached Materials. *ACS Nano* **2016,** *10* (6), 6108-6115.

- Wu, K.; Chen, J.; McBride, J. R.; Lian, T., Efficient hot-electron transfer by a plasmon-induced interfacial charge-transfer transition. *Science* **2015,** *349* (6248), 632-635.
- Cui, J. B.; Li, Y. J.; Liu, L.; Chen, L.; Xu, J.; Ma, J. W.; Fang, G.; Zhu, E. B.; Wu, H.; Zhao, L. X.; Wang, L. Y.; Huang, Y., Near-Infrared Plasmonic-Enhanced Solar Energy Harvest for Highly Efficient Photocatalytic Reactions. *Nano Lett.* **2015,** *15* (10), 6295-6301.
- Gan, X. Y.; Keller, E. L.; Warkentin, C. L.; Crawford, S. E.; Frontiera, R. R.; Millstone, J. E., Plasmon-Enhanced Chemical Conversion Using Copper Selenide Nanoparticles. *Nano Lett.* **2019,** *19* (4), 2384-2388.
- Govorov, A. O.; Richardson, H. H., Generating heat with metal nanoparticles. *Nano Today* **2007,** *2* (1), 30-38.
- Murphy, C. J.; Chang, H. H.; Falagan-Lotsch, P.; Gole, M. T.; Hofmann, D. M.; Hoang, K. N. L.; McClain, S. M.; Meyer, S. M.; Turner, J. G.; Unnikrishnan, M.; Wu, M.; Zhang, X.; Zhang, Y. S., Virus-Sized Gold Nanorods: Plasmonic Particles for Biology. *Acc. Chem. Res.* **2019,** *52* (8), 2124-2135.
- Wang, S. H.; Riedinger, A.; Li, H. B.; Fu, C. H.; Liu, H. Y.; Li, L. L.; Liu, T. L.; Tan, L. F.; Barthel, M. J.; Pugliese, G.; De Donato, F.; D'Abbusco, M. S.; Meng, X. W.; Manna, L.; Meng, H.; Pellegrino, T., Plasmonic Copper Sulfide Nanocrystals Exhibiting Near-Infrared Photothermal and Photodynamic Therapeutic Effects. *ACS Nano* **2015,** *9* (2), 1788-1800.

- Hessel, C. M.; Pattani, V. P.; Rasch, M.; Panthani, M. G.; Koo, B.; Tunnell, J. W.; Korgel, B. A., Copper Selenide Nanocrystals for Photothermal Therapy. *Nano Lett.* **2011,** *11* (6), 2560-2566.
- Huang, X. H.; El-Sayed, I. H.; Qian, W.; El-Sayed, M. A., Cancer cell imaging and photothermal therapy in the near-infrared region by using gold nanorods. *J. Am. Chem. Soc.* **2006,** *128* (6), 2115-2120.
- Willets, K. A.; Van Duyne, R. P., Localized surface plasmon resonance spectroscopy and sensing. *Annu. Rev. Phys. Chem.* **2007,** *58*, 267-297.
- Haes, A. J.; Zou, S. L.; Schatz, G. C.; Van Duyne, R. P., Nanoscale optical biosensor: Short range distance dependence of the localized surface plasmon resonance of noble metal nanoparticles. *J. Phys. Chem. B* **2004,** *108* (22), 6961-6968.
- Yu, C. X.; Irudayaraj, J., Multiplex biosensor using gold nanorods. *Anal. Chem.* **2007,** *79* (2), 572-579.
- Sun, Y. G.; Xia, Y. N., Increased sensitivity of surface plasmon resonance of gold nanoshells compared to that of gold solid colloids in response to environmental changes. *Anal. Chem.* **2002,** *74* (20), 5297-5305.
- Link, S.; El-Sayed, M. A., Size and temperature dependence of the plasmon absorption of colloidal gold nanoparticles. *J. Phys. Chem. B* **1999,** *103* (21), 4212-4217.
- Murphy, C. J.; San, T. K.; Gole, A. M.; Orendorff, C. J.; Gao, J. X.; Gou, L.; Hunyadi, S. E.; Li, T., Anisotropic metal nanoparticles: Synthesis, assembly, and optical applications. *J. Phys. Chem. B* **2005,** *109* (29), 13857-13870.

- Link, S.; Mohamed, M. B.; El-Sayed, M. A., Simulation of the optical absorption spectra of gold nanorods as a function of their aspect ratio and the effect of the medium dielectric constant. *J. Phys. Chem. B* **1999,** *103* (16), 3073-3077.
- Hu, M.; Chen, J. Y.; Li, Z. Y.; Au, L.; Hartland, G. V.; Li, X. D.; Marquez, M.; Xia, Y. N., Gold nanostructures: engineering their plasmonic properties for biomedical applications. *Chem. Soc. Rev.* **2006,** *35* (11), 1084-1094.
- Sun, Y. G.; Mayers, B. T.; Xia, Y. N., Template-engaged replacement reaction: A one-step approach to the large-scale synthesis of metal nanostructures with hollow interiors. *Nano Lett.* **2002,** *2* (5), 481-485.
- Jain, P. K.; El-Sayed, M. A., Universal scaling of plasmon coupling in metal nanostructures: Extension from particle pairs to nanoshells. *Nano Lett.* **2007,** *7* (9), 2854-2858.
- Wang, Y. W.; Xie, X. Y.; Wang, X. D.; Ku, G.; Gill, K. L.; O'Neal, D. P.; Stoica, G.; Wang, L. V., Photoacoustic tomography of a nanoshell contrast agent in the in vivo rat brain. *Nano Lett.* **2004,** *4* (9), 1689-1692.
- Wang, H.; Tam, F.; Grady, N. K.; Halas, N. J., Cu nanoshells: Effects of interband transitions on the nanoparticle plasmon resonance. *J. Phys. Chem. B* **2005,** *109* (39), 18218-18222.
- Wang, H.; Wu, Y. P.; Lassiter, B.; Nehl, C. L.; Hafner, J. H.; Nordlander, P.; Halas, N. J., Symmetry breaking in individual plasmonic nanoparticles. *Proc. Natl. Acad. Sci. U.S.A.* **2006,** *103* (29), 10856-10860.

- Jing, H.; Zhang, Q. F.; Large, N.; Yu, C. M.; Blom, D. A.; Nordlander, P.; Wang, H., Tunable Plasmonic Nanoparticles with Catalytically Active High-Index Facets. *Nano Lett.* **2014,** *14* (6), 3674-3682.
- Luther, J. M.; Jain, P. K.; Ewers, T.; Alivisatos, A. P., Localized surface plasmon resonances arising from free carriers in doped quantum dots. *Nat. Mater.* **2011,** *10* (5), 361-366.
- Naik, G. V.; Shalaev, V. M.; Boltasseva, A., Alternative Plasmonic Materials: Beyond Gold and Silver. *Adv. Mater.* **2013,** *25* (24), 3264-3294.
- Zhao, Y. X.; Pan, H. C.; Lou, Y. B.; Qiu, X. F.; Zhu, J. J.; Burda, C., Plasmonic $Cu_{2-x}S$ Nanocrystals: Optical and Structural Properties of Copper-Deficient Copper(I) Sulfides. *J. Am. Chem. Soc.* **2009,** *131* (12), 4253-4261.
- Kriegel, I.; Jiang, C. Y.; Rodriguez-Fernandez, J.; Schaller, R. D.; Talapin, D. V.; da Como, E.; Feldmann, J., Tuning the Excitonic and Plasmonic Properties of Copper Chalcogenide Nanocrystals. *J. Am. Chem. Soc.* **2012,** *134* (3), 1583-1590.
- Xie, Y.; Riedinger, A.; Prato, M.; Casu, A.; Genovese, A.; Guardia, P.; Sottini, S.; Sangregorio, C.; Miszta, K.; Ghosh, S.; Pellegrino, T.; Manna, L., Copper Sulfide Nanocrystals with Tunable Composition by Reduction of Covellite Nanocrystals with Cu^+ Ions. *J. Am. Chem. Soc.* **2013,** *135* (46), 17630-17637.
- Kriegel, I.; Rodriguez-Fernandez, J.; Wisnet, A.; Zhang, H.; Waurisch, C.; Eychmuller, A.; Dubavik, A.; Govorov, A. O.; Feldmann, J., Shedding Light on Vacancy-Doped Copper Chalcogenides: Shape-Controlled Synthesis, Optical Properties, and Modeling of Copper Telluride Nanocrystals with Near-Infrared Plasmon Resonances. *ACS Nano* **2013,** *7* (5), 4367-4377.

- Liu, Y.; Liu, M.; Swihart, M. T., Plasmonic Copper Sulfide-Based Materials: A Brief Introduction to Their Synthesis, Doping, Alloying, and Applications. *J. Phys. Chem. C* **2017,** *121* (25), 13435-13447.
- Hsu, S. W.; Ngo, C.; Tao, A. R., Tunable and Directional Plasmonic Coupling within Semiconductor Nanodisk Assemblies. *Nano Lett.* **2014,** *14* (5), 2372-2380.
- Cordova-Castro, R. M.; Casavola, M.; van Schilfgaarde, M.; Krasavin, A. V.; Green, M. A.; Richards, D.; Zayats, A. V., Anisotropic Plasmonic CuS Nanocrystals as a Natural Electronic Material with Hyperbolic Optical Dispersion. *ACS Nano* **2019,** *13* (6), 6550-6560.
- Liu, Z. K.; Zhong, Y. X.; Shafei, I.; Jeong, S.; Wang, L. G.; Nguyen, H. T.; Sun, C. J.; Li, T.; Chen, J.; Chen, L.; Losovyj, Y.; Gao, X. F.; Ma, W. L.; Ye, X. C., Broadband Tunable Mid-infrared Plasmon Resonances in Cadmium Oxide Nanocrystals Induced by Size-Dependent Nonstoichiometry. *Nano Lett.* **2020,** *20* (4), 2821-2828.
- Lounis, S. D.; Runnerstrom, E. L.; Bergerud, A.; Nordlund, D.; Milliron, D. J., Influence of Dopant Distribution on the Plasmonic Properties of Indium Tin Oxide Nanocrystals. *J. Am. Chem. Soc.* **2014,** *136* (19), 7110-7116.
- Palomaki, P. K. B.; Miller, E. M.; Neale, N. R., Control of Plasmonic and Interband Transitions in Colloidal Indium Nitride Nanocrystals. *J. Am. Chem. Soc.* **2013,** *135* (38), 14142-14150.
- Barragan, A. A.; Ilawe, N. V.; Zhong, L.; Wong, B. M.; Mangolini, L., A Non-Thermal Plasma Route to Plasmonic TiN Nanoparticles. *J. Phys. Chem. C* **2017,** *121* (4), 2316-2322.

- Kasic, A.; Schubert, M.; Einfeldt, S.; Hommel, D.; Tiwald, T. E., Free-carrier and phonon properties of n- and p-type hexagonal GaN films measured by infrared ellipsometry. *Phys. Rev. B* **2000,** *62* (11), 7365-7377.
- Donovan, B. F.; Sachet, E.; Maria, J. P.; Hopkins, P. E., Interplay between mass-impurity and vacancy phonon scattering effects on the thermal conductivity of doped cadmium oxide. *Appl. Phys. Lett.* **2016,** *108* (2).
- Dorfs, D.; Hartling, T.; Miszta, K.; Bigall, N. C.; Kim, M. R.; Genovese, A.; Falqui, A.; Povia, M.; Manna, L., Reversible Tunability of the Near-Infrared Valence Band Plasmon Resonance in $Cu_{2-x}Se$ Nanocrystals. *J. Am. Chem. Soc.* **2011,** *133* (29), 11175-11180.
- Muhammed, M. A. H.; Doblinger, M.; Rodriguez-Fernandez, J., Switching Plasmons: Gold Nanorod-Copper Chalcogenide Core-Shell Nanoparticle Clusters with Selectable Metal/Semiconductor NIR Plasmon Resonances. *J. Am. Chem. Soc.* **2015,** *137* (36), 11666-11677.
- Faucheaux, J. A.; Jain, K., Plasmons in Photocharged ZnO Nanocrystals Revealing the Nature of Charge Dynamics. *J. Phys. Chem. Lett.* **2013,** *4* (18), 3024-3030.
- Gavrilyuk, A. I., Photochromism in WO3 thin films. *Electrochim. Acta* **1999,** *44* (18), 3027-3037.
- Schimpf, A. M.; Lounis, S. D.; Runnerstrom, E. L.; Milliron, D. J.; Gamelin, D. R., Redox Chemistries and Plasmon Energies of Photodoped In2O3 and Sn-Doped In2O3 (ITO) Nanocrystals. *J. Am. Chem. Soc.* **2015,** *137* (1), 518-524.

- Garcia, G.; Buonsanti, R.; Runnerstrom, E. L.; Mendelsberg, R. J.; Llordes, A.; Anders, A.; Richardson, T. J.; Milliron, D. J., Dynamically Modulating the Surface Plasmon Resonance of Doped Semiconductor Nanocrystals. *Nano Lett.* **2011,** *11* (10), 4415-4420.
- Wang, C. J.; Shim, M.; Guyot-Sionnest, P., Electrochromic nanocrystal quantum dots. *Science* **2001,** *291* (5512), 2390-2392.
- Landau, L., On the Vibrations of the Electronic Plasma. *Zh. Eksperim. i Teor. Fiz.* **1946,** *16* (7), 574-586.
- Ryutov, D. D., Landau damping: half a century with the great discovery. *Plasma Phys. Control. Fusion* **1999,** *41*, A1-A12.
- Linic, S.; Christopher, P.; Ingram, D. B., Plasmonic-metal nanostructures for efficient conversion of solar to chemical energy. *Nat. Mater.* **2011,** *10* (12), 911-921.
- Zhang, Q. F.; Zhou, Y. D.; Fu, X. Q.; Villarreal, E.; Sun, L. C.; Zou, S. L.; Wang, H., Photothermal Effect, Local Field Dependence, and Charge Carrier Relaying Species in Plasmon-Driven Photocatalysis: A Case Study of Aerobic Nitrothiophenol Coupling Reaction. *J. Phys. Chem. C* **2019,** *123* (43), 26695-26704.
- Brongersma, M. L.; Halas, N. J.; Nordlander, P., Plasmon-induced hot carrier science and technology. *Nat. Nanotechnol.* **2015,** *10* (1), 25-34.
- Zhang, Y. C.; He, S.; Guo, W. X.; Hu, Y.; Huang, J. W.; Mulcahy, J. R.; Wei, W. D., Surface-Plasmon-Driven Hot Electron Photochemistry. *Chem. Rev.* **2018,** *118* (6), 2927-2954.

- Zhu, H. Y.; Chen, X.; Zheng, Z. F.; Ke, X. B.; Jaatinen, E.; Zhao, J. C.; Guo, C.; Xie, T. F.; Wang, D. J., Mechanism of supported gold nanoparticles as photocatalysts under ultraviolet and visible light irradiation. *Chem. Commun.* **2009,** (48), 7524-7526.
- Zhao, J.; Nguyen, S. C.; Ye, R.; Ye, B. H.; Weller, H.; Somorjai, G. A.; Alivisatos, A. P.; Toste, F. D., A Comparison of Photocatalytic Activities of Gold Nanoparticles Following Plasmonic and Interband Excitation and a Strategy for Harnessing Interband Hot Carriers for Solution Phase Photocatalysis. *ACS Cent. Sci.* **2017,** *3* (5), 482-488.
- Fu, X. Q.; Li, G. G.; Villarreal, E.; Wang, H., Hot carriers in action: multimodal photocatalysis on Au@SnO2 core-shell nanoparticles. *Nanoscale* **2019,** *11* (15), 7324-7334.
- Sun, M. Q.; Fu, X. Q.; Chen, K. X.; Wang, H., Dual-Plasmonic Gold@Copper Sulfide Core-Shell Nanoparticles: Phase-Selective Synthesis and Multimodal Photothermal and Photocatalytic Behaviors. *ACS Appl. Mater. Interfaces* **2020,** *12* (41), 46146-46161.
- Hou, W. B.; Hung, W. H.; Pavaskar, P.; Goeppert, A.; Aykol, M.; Cronin, S. B., Photocatalytic Conversion of CO2 to Hydrocarbon Fuels via Plasmon-Enhanced Absorption and Metallic Interband Transitions. *ACS Catal.* **2011,** *1* (8), 929-936.
- Johnson, P. B.; Christy, R. W., Optical-Constants of Copper and Nickel as a Function of Temperature. *Phys. Rev. B* **1975,** *11* (4), 1315-1323.
- Motl, N. E.; Ewusi-Annan, E.; Sines, I. T.; Jensen, L.; Schaak, R. E., Au-Cu Alloy Nanoparticles with Tunable Compositions and Plasmonic Properties:

Experimental Determination of Composition and Correlation with Theory. *J. Phys. Chem. C* **2010,** *114* (45), 19263-19269.

- Mulvaney, P., Surface plasmon spectroscopy of nanosized metal particles. *Langmuir* **1996,** *12* (3), 788-800.
- Sundararaman, R.; Narang, P.; Jermyn, A. S.; Goddard, W. A.; Atwater, H. A., Theoretical predictions for hot-carrier generation from surface plasmon decay. *Nat. Commun.* **2014,** *5*.
- Kim, D.; Resasco, J.; Yu, Y.; Asiri, A. M.; Yang, P. D., Synergistic geometric and electronic effects for electrochemical reduction of carbon dioxide using gold-copper bimetallic nanoparticles. *Nat. Commun.* **2014,** *5*.
- Gilroy, K. D.; Ruditskiy, A.; Peng, H. C.; Qin, D.; Xia, Y. N., Bimetallic Nanocrystals: Syntheses, Properties, and Applications. *Chem. Rev.* **2016,** *116* (18), 10414-10472.
- Ozolins, V.; Wolverton, C.; Zunger, A., Cu-Au, Ag-Au, Cu-Ag, and Ni-Au intermetallics: First-principles study of temperature-composition phase diagrams and structures. *Phys. Rev. B* **1998,** *57* (11), 6427-6443.
- Li, G. G.; Villarreal, E.; Zhang, Q. F.; Zheng, T. T.; Zhu, J. J.; Wang, H., Controlled Dealloying of Alloy Nanoparticles toward Optimization of Electrocatalysis on Spongy Metallic Nanoframes. *ACS Appl. Mater. Interfaces* **2016,** *8* (36), 23920-23931.
- Aden, A. L.; Kerker, M., Scattering of Electromagnetic Waves from 2 Concentric Spheres. *J. Appl. Phys.* **1951,** *22* (10), 1242-1246.

- Macdonald, F.; Lide, D. R., CRC handbook of chemistry and physics: From paper to web. *Abstr. Pap. Am. Chem. Soc.* **2003,** *225*, U552-U552.
- Scholl, J. A.; Koh, A. L.; Dionne, J. A., Quantum plasmon resonances of individual metallic nanoparticles. *Nature* **2012,** *483* (7390), 421-U68.
- Vegard, L., The constitution of the mixed crystals and the filling of space of the atoms. *Z. Phys.* **1921,** *5*, 17-26.
- Lubarda, V. A., On the effective lattice parameter of binary alloys. *Mech. Mater.* **2003,** *35* (1-2), 53-68.
- Jain, P. K., Taking the Heat Off of Plasmonic Chemistry. *J. Phys. Chem. C* **2019,** *123* (40), 24347-24351.
- Li, G. G.; Sun, M. Q.; Villarreal, E.; Pandey, S.; Phillpot, S. R.; Wang, H., Galvanic Replacement-Driven Transformations of Atomically Intermixed Bimetallic Colloidal Nanocrystals: Effects of Compositional Stoichiometry and Structural Ordering. *Langmuir* **2018,** *34* (14), 4340-4350.
- Roper, D. K.; Ahn, W.; Hoepfner, M., Microscale heat transfer transduced by surface plasmon resonant gold nanoparticles. *J. Phys. Chem. C* **2007,** *111* (9), 3636-3641.
- Comin, A.; Manna, L. New Materials for Tunable Plasmonic Colloidal Nanocrystals. *Chem. Soc. Rev.* **2014,** *43* (11), 3957-3975.
- Wang, H.; Brandl, D. W.; Nordlander, P.; Halas, N. J. Plasmonic Nanostructures: Artificial Molecules. *Acc. Chem. Res.* **2007,** *40* (1), 53-62.
- Linic, S.; Aslam, U.; Boerigter, C.; Morabito, M. Photochemical Transformations on Plasmonic Metal Nanoparticles. *Nat. Mater.* **2015,** *14* (6), 567-576.

- Mukherjee, S.; Libisch, F.; Large, N.; Neumann, O.; Brown, L. V.; Cheng, J.; Lassiter, J. B.; Carter, E. A.; Nordlander, P.; Halas, N. J. Hot Electrons Do the Impossible: Plasmon-Induced Dissociation of H_2 on Au. *Nano Lett.* **2013,** *13* (1), 240-247.
- Lal, S.; Clare, S. E.; Halas, N. J., Nanoshell-Enabled Photothermal Cancer Therapy: Impending Clinical Impact. *Acc. Chem. Res.* **2008,** *41* (12), 1842-1851.
- Xia, Y. N.; Li, W. Y.; Cobley, C. M.; Chen, J. Y.; Xia, X. H.; Zhang, Q.; Yang, M. X.; Cho, E. C.; Brown, P. K. Gold Nanocages: From Synthesis to Theranostic Applications. *Acc. Chem. Res.* **2011,** *44* (10), 914-924.
- Huang, X. H.; Neretina, S.; El-Sayed, M. A. Gold Nanorods: From Synthesis and Properties to Biological and Biomedical Applications. *Adv. Mater.* **2009,** *21* (48), 4880-4910.
- Zheng, T. T.; Li, G. G.; Zhou, F.; Wu, R.; Zhu, J. J.; Wang, H. Gold-Nanosponge-Based Multistimuli-Responsive Drug Vehicles for Targeted Chemo-Photothermal Therapy. *Adv. Mater.* **2016,** *28* (37), 8218-8226.
- Dorfs, D.; Härtling, T.; Miszta, K.; Bigall, N. C.; Kim, M. R.; Genovese, A.; Falqui, A.; Povia, M.; Manna, L. Reversible Tunability of the near-Infrared Valence Band Plasmon Resonance in $Cu_{2-x}Se$ Nanocrystals. *J. Am. Chem. Soc.* **2011,** *133* (29), 11175-11180.
- Xie, Y.; Carbone, L.; Nobile, C.; Grillo, V.; D'Agostino, S.; Della Sala, F.; Giannini, C.; Altamura, D.; Oelsner, C.; Kryschi, C.; Cozzoli, P. D. Metallic-Like Stoichiometric Copper Sulfide Nanocrystals: Phase- and Shape-Selective

Synthesis, Near-Infrared Surface Plasmon Resonance Properties, and Their Modeling. *ACS Nano* **2013,** *7* (8), 7352-7369.

- Manthiram, K.; Alivisatos, A. P. Tunable Localized Surface Plasmon Resonances in Tungsten Oxide Nanocrystals. *J. Am. Chem. Soc.* **2012,** *134* (9), 3995-3998.
- Ye, X. C.; Fei, J. Y.; Diroll, B. T.; Paik, T.; Murray, C. B. Expanding the Spectral Tunability of Plasmonic Resonances in Doped Metal-Oxide Nanocrystals through Cooperative Cation-Anion Codoping. *J. Am. Chem. Soc.* **2014,** *136* (33), 11680-11686.
- Gordon, T. R.; Paik, T.; Klein, D. R.; Naik, G. V.; Caglayan, H.; Boltasseva, A.; Murray, C. B., Shape-Dependent Plasmonic Response and Directed Self-Assembly in a New Semiconductor Building Block, Indium-Doped Cadmium Oxide (ICO). *Nano Lett.* **2013,** *13* (6), 2857-2863.
- Manna, G.; Bose, R.; Pradhan, N. Semiconducting and Plasmonic Copper Phosphide Platelets. *Angew. Chem. Int. Ed.* **2013,** *52* (26), 6762-6766.
- Liu, X.; Swihart, M. T. Heavily-Doped Colloidal Semiconductor and Metal Oxide Nanocrystals: An Emerging New Class of Plasmonic Nanomaterials. *Chem. Soc. Rev.* **2014,** *43* (11), 3908-3920.
- Huang, X. J.; Zhang, W. L.; Guan, G. Q.; Song, G. S.; Zou, R. J.; Hu, J. Q. Design and Functionalization of the Nir-Responsive Photothermal Semiconductor Nanomaterials for Cancer Theranostics. *Acc. Chem. Res.* **2017,** *50* (10), 2529-2538.
- Liu, Y.; Zhu, D. W.; Hu, Y. J.; Swihart, M. T.; Wei, W. Controlled Synthesis of $Cu_{2-x}Se$ Nanoparticles as Near-Infrared Photothermal Agents and Irradiation

Wavelength Dependence of Their Photothermal Conversion Efficiency. *Langmuir* **2018,** *34* (46), 13905-13909.

- Zhou, M.; Zhang, R.; Huang, M. A.; Lu, W.; Song, S. L.; Melancon, M. P.; Tian, M.; Liang, D.; Li, C. A Chelator-Free Multifunctional Cu-64 CuS Nanoparticle Platform for Simultaneous Micro-Pet/Ct Imaging and Photothermal Ablation Therapy. *J. Am. Chem. Soc.* **2010,** *132* (43), 15351-15358.
- Liu, X.; Lee, C.; Law, W. C.; Zhu, D. W.; Liu, M. X.; Jeon, M.; Kim, J.; Prasad, P. N.; Kim, C.; Swihart, M. T. Au-$Cu_{2-x}Se$ Heterodimer Nanoparticles with Broad Localized Surface Plasmon Resonance as Contrast Agents for Deep Tissue Imaging. *Nano Lett.* **2013,** *13* (9), 4333-4339.
- Ma, L.; Chen, Y. L.; Yang, X.; Li, H. X.; Ding, S. J.; Hou, H. Y.; Xiong, L.; Qin, P. L.; Chen, X. B. Growth Behavior of Au/$Cu_{2-x}S$ Hybrids and Their Plasmon-Enhanced Dual-Functional Catalytic Activity. *CrystEngComm* **2019,** *21* (37), 5610-5617.
- Jiang, R. B.; Li, B. X.; Fang, C. H.; Wang, J. F. Metal/Semiconductor Hybrid Nanostructures for Plasmon-Enhanced Applications. *Adv. Mater.* **2014,** *26* (31), 5274-5309.
- Zhu, H.; Wang, Y.; Chen, C.; Ma, M. R.; Zeng, J. F.; Li, S. Z.; Xia, Y. S.; Gao, M. Y. Monodisperse Dual Plasmonic Au@$Cu_{2-X}E$ (E=S, Se) Core@Shell Supraparticles: Aqueous Fabrication, Multimodal Imaging, and Tumor Therapy at in Vivo Level. *ACS Nano* **2017,** *11* (8), 8273-8281.
- Kim, Y.; Park, K. Y.; Jang, D. M.; Song, Y. M.; Kim, H. S.; Cho, Y. J.; Myung, Y.; Park, J. Synthesis of Au-Cu_2S Core-Shell Nanocrystals and Their

Photocatalytic and Electrocatalytic Activity. *J. Phys. Chem. C* **2010,** *114* (50), 22141-22146.

- Ji, M. W.; Xu, M.; Zhang, W.; Yang, Z. Z.; Huang, L.; Liu, J. J.; Zhang, Y.; Gu, L.; Yu, Y. X.; Hao, W. C.; An, P. F.; Zheng, L. R.; Zhu, H. S.; Zhang, J. T. Structurally Well-Defined Au@$Cu_{2-x}S$ Core-Shell Nanocrystals for Improved Cancer Treatment Based on Enhanced Photothermal Efficiency. *Adv. Mater.* **2016,** *28* (16), 3094-3101.
- Sun, Z. H.; Yang, Z.; Zhou, J. H.; Yeung, M. H.; Ni, W. H.; Wu, H. K.; Wang, J. F. A General Approach to the Synthesis of Gold-Metal Sulfide Core-Shell and Heterostructures. *Angew. Chem. Int. Ed.* **2009,** *48* (16), 2881-2885.
- Chang, Y.; Cheng, Y.; Feng, Y. L.; Jian, H.; Wang, L.; Ma, X. M.; Li, X.; Zhang, H. Y. Resonance Energy Transfer-Promoted Photothermal and Photodynamic Performance of Gold- Copper Sulfide Yolk-Shell Nanoparticles for Chemophototherapy of Cancer. *Nano Lett.* **2018,** *18* (2), 886-897.
- Ding, X. G.; Liow, C. H.; Zhang, M. X.; Huang, R. J.; Li, C. Y.; Shen, H.; Liu, M. Y.; Zou, Y.; Gao, N.; Zhang, Z. J.; Li, Y. G.; Wang, Q. B.; Li, S. Z.; Jiang, J. Surface Plasmon Resonance Enhanced Light Absorption and Photothermal Therapy in the Second Near-Infrared Window. *J. Am. Chem. Soc.* **2014,** *136* (44), 15684-15693.
- Huo, D.; Cao, Z. M.; Li, J.; Xie, M. H.; Tao, J.; Xia, Y. N. Seed-Mediated Growth of Au Nanospheres into Hexagonal Stars and the Emergence of a Hexagonal Close-Packed Phase. *Nano Lett.* **2019,** *19* (5), 3115-3121.

- Fan, Z. X.; Huang, X.; Chen, Y.; Huang, W.; Zhang, H. Facile Synthesis of Gold Nanomaterials with Unusual Crystal Structures. *Nat. Protoc.* **2017,** *12* (11), 2367-2378.
- Zhang, J. T.; Tang, Y.; Lee, K.; Min, O. Y. Nonepitaxial Growth of Hybrid Core-Shell Nanostructures with Large Lattice Mismatches. *Science* **2010,** *327* (5973), 1634-1638.
- Lv, Q.; Min, H.; Duan, D. B.; Fang, W.; Pan, G. M.; Shen, A. G.; Wang, Q. Q.; Nie, G. J.; Hu, J. M. Total Aqueous Synthesis of Au@$Cu_{2-x}S$ Core-Shell Nanoparticles for in vitro and in vivo SERS/PA Imaging-Guided Photothermal Cancer Therapy. *Adv. Healthc. Mater.* **2019,** *8* (2), 1801257.
- Zhang, P.; Li, Y.; Wang, D.; Xia, H. High-Yield Production of Uniform Gold Nanoparticles with Sizes from 31 to 577 nm via One-Pot Seeded Growth and Size-Dependent Sers Property. *Part. Part. Syst. Charact.* **2016,** *33* (12), 924-932.
- Morales-García, A.; Soares, A. L.; Dos Santos, E. C.; de Abreu, H. A.; Duarte, H. A. First-Principles Calculations and Electron Density Topological Analysis of Covellite (CuS). *J. Phys. Chem. A* **2014,** *118* (31), 5823-5831.
- Adhikari, S.; Sarkar, D.; Madras, G. Hierarchical Design of CuS Architectures for Visible Light Photocatalysis of 4-Chlorophenol. *ACS Omega* **2017,** *2* (7), 4009-4021.
- Basu, M.; Sinha, A. K.; Pradhan, M.; Sarkar, S.; Negishi, Y.; Govind; Pal, T. Evolution of Hierarchical Hexagonal Stacked Plates of CuS from Liquid-Liquid Interface and Its Photocatalytic Application for Oxidative Degradation of

Different Dyes under Indoor Lighting. *Environ. Sci. Technol.* **2010,** *44* (16), 6313-6318.

- Xu, Q.; Huang, B.; Zhao, Y. F.; Yan, Y. F.; Noufi, R.; Wei, S. H. Crystal and Electronic Structures of Cu_xS Solar Cell Absorbers. *Appl. Phys. Lett.* **2012,** *100* (6), 061906.
- Martinson, A. B. F.; Riha, S. C.; Thimsen, E.; Elam, J. W.; Pellin, M. J. Structural, Optical, and Electronic Stability of Copper Sulfide Thin Films Grown by Atomic Layer Deposition. *Energy Environ. Sci.* **2013,** *6* (6), 1868-1878.
- Hoffmann, M. R.; Martin, S. T.; Choi, W. Y.; Bahnemann, D. W. Environmental Applications of Semiconductor Photocatalysis. *Chem. Rev.* **1995,** *95* (1), 69-96.
- Xu, Y.; Schoonen, M. A. A. The Absolute Energy Positions of Conduction and Valence Bands of Selected Semiconducting Minerals. *Am. Mineral.* **2000,** *85* (3-4), 543-556.
- Yang, Z. J.; Cao, Y.; Li, J.; Lu, M. M.; Jiang, Z. K.; Hu, X. Y. Smart CuS Nanoparticles as Peroxidase Mimetics for the Design of Novel Label-Free Chemiluminescent Immunoassay. *ACS Appl. Mater. Interfaces* **2016,** *8* (19), 12031-12038.
- He, W. W.; Jia, H. M.; Li, X. X.; Lei, Y.; Li, J.; Zhao, H. X.; Mi, L. W.; Zhang, L. Z.; Zheng, Z. Understanding the Formation of CuS Concave Superstructures with Peroxidase-Like Activity. *Nanoscale* **2012,** *4* (11), 3501-3506.
- Baffou, G.; Bordacchini, I.; Baldi, A.; Quidant, R. Simple Experimental Procedures to Distinguish Photothermal from Hot-Carrier Processes in Plasmonics. *Light-Sci. Appl.* **2020,** *9* (1), 108.

- Goldstein, S.; Aschengrau, D.; Diamant, Y.; Rabani, J. Photolysis of Aqueous H_2O_2: Quantum Yield and Applications for Polychromatic UV Actinometry in Photoreactors. *Environ. Sci. Technol.* **2007,** *41* (21), 7486-7490.
- Zhang, P.; Li, Y.; Wang, D.; Xia, H. High–Yield Production of Uniform Gold Nanoparticles with Sizes from 31 to 577 nm *via* One-Pot Seeded Growth and Size-Dependent SERS Property. *Part. Part. Syst. Charact.* **2016,** *33* (12), 924-932.
- Johnson, P. B.; Christy, R. W. Optical Constants of the Noble Metals. *Phys. Rev. B* **1972,** *6* (12), 4370-4379.
- Incropera, F. P.; DeWitt, D. P.; Incropera, F. P. *Fundamentals of Heat and Mass Transfer*. 2nd Ed.; Wiley: New York, 1985.
- Bu, X. Y.; Zhou, D.; Li, J.; Zhang, X.; Zhang, K.; Zhang, H.; Yang, B., Copper Sulfide Self-Assembly Architectures with Improved Photothermal Performance. *Langmuir* **2014,** *30* (5), 1416-1423.
- Tian, Q. W.; Tang, M. H.; Sun, Y. G.; Zou, R. J.; Chen, Z. G.; Zhu, M. F.; Yang, S. P.; Wang, J. L.; Wang, J. H.; Hu, J. Q., Hydrophilic Flower-Like CuS Superstructures as an Efficient 980 nm Laser-Driven Photothermal Agent for Ablation of Cancer Cells. *Adv. Mater.* **2011,** *23* (31), 3542-+.
- Liu, X. J.; Li, B.; Fu, F. F.; Xu, K. B.; Zou, R. J.; Wang, Q.; Zhang, B. J.; Chen, Z. G.; Hu, J. Q., Facile synthesis of biocompatible cysteine-coated CuS nanoparticles with high photothermal conversion efficiency for cancer therapy. *Dalton Trans.* **2014,** *43* (30), 11709-11715.

- Zhang, J.; Yu, J. G.; Zhang, Y. M.; Li, Q.; Gong, J. R., Visible Light Photocatalytic H-2-Production Activity of CuS/ZnS Porous Nanosheets Based on Photoinduced Interfacial Charge Transfer. *Nano Lett.* **2011,** *11* (11), 4774-4779.
- Tanveer, M.; Cao, C. B.; Ali, Z.; Aslam, I.; Idrees, F.; Khan, W. S.; But, F. K.; Tahir, M.; Mahmood, N., Template free synthesis of CuS nanosheet-based hierarchical microspheres: an efficient natural light driven photocatalyst. *CrystEngComm* **2014,** *16* (24), 5290-5300.
- Zhang, Y. Q.; Zhang, B. P.; Zhu, L. F., Monodisperse CuS nanodisks: low-temperature solvothermal synthesis and enhanced photocatalytic activity. *RSC Adv.* **2014,** *4* (103), 59185-59193.
- Zhao, L.; Tao, F. Q.; Quan, Z.; Zhou, X. L.; Yuan, Y. H.; Hu, J. C., Bubble template synthesis of copper sulfide hollow spheres and their applications in lithium ion battery. *Mater. Lett.* **2012,** *68*, 28-31.
- Hosseinpour, Z.; Scarpellini, A.; Najafishirtari, S.; Marras, S.; Colombo, M.; Alemi, A.; De Volder, M.; George, C.; Lesnyak, V., Morphology-Dependent Electrochemical Properties of CuS Hierarchical Superstructures. *ChemPhysChem* **2015,** *16* (16), 3418-3424.
- Li, Q. W.; Xue, Y.; Zhu, Y. C.; Qian, Y. T., Facile Synthesis and Application of CuS Nanospheres in Aqueous and Organic Lithium Ion Batteries. *J. Nanosci. Nanotechnol.* **2013,** *13* (2), 1265-1269.
- Gotsis, H. J.; Barnes, A. C.; Strange, P., Experimental and Theoretical Investigation of the Crystal-Structure of Cus. *J. Phys. Condens. Matter* **1992,** *4* (50), 10461-10468.

- Liu, M. X.; Xue, X. Z.; Ghosh, C.; Liu, X.; Liu, Y.; Furlani, E. P.; Swihart, M. T.; Prasad, P. N., Room-Temperature Synthesis of Covellite Nanoplatelets with Broadly Tunable Localized Surface Plasmon Resonance. *Chem. Mater.* **2015,** *27* (7), 2584-2590.
- Zhang, K. A.; Zhang, T. N.; Cheng, G. H.; Li, T. X.; Wang, S. X.; Wei, W.; Zhou, X. H.; Yu, W. W.; Sun, Y.; Wang, P.; Zhang, D.; Zeng, C. G.; Wang, X. J.; Hu, W. D.; Fan, H. J.; Shen, G. Z.; Chen, X.; Duan, X. F.; Chang, K.; Dai, N., Interlayer Transition and Infrared Photodetection in Atomically Thin Type-II MoTe2/MoS2 van der Waals Heterostructures. *ACS Nano* **2016,** *10* (3), 3852-3858.
- Gong, Y. J.; Lin, J. H.; Wang, X. L.; Shi, G.; Lei, S. D.; Lin, Z.; Zou, X. L.; Ye, G. L.; Vajtai, R.; Yakobson, B. I.; Terrones, H.; Terrones, M.; Tay, B. K.; Lou, J.; Pantelides, S. T.; Liu, Z.; Zhou, W.; Ajayan, P. M., Vertical and in-plane heterostructures from WS2/MoS2 monolayers. *Nat. Mater.* **2014,** *13* (12), 1135-1142.
- Pan, B. J.; Zhang, K. A.; Ding, C. C.; Wu, Z.; Fan, Q. C.; Luo, T. Y.; Zhang, L. J.; Zou, C.; Huang, S. M., Universal Precise Growth of 2D Transition-Metal Dichalcogenides in Vertical Direction. *ACS Appl. Mater. Interfaces* **2020,** *12* (31), 35337-35344.
- Lee, C.; Yan, H.; Brus, L. E.; Heinz, T. F.; Hone, J.; Ryu, S., Anomalous Lattice Vibrations of Single- and Few-Layer MoS2. *ACS Nano* **2010,** *4* (5), 2695-2700.
- Nasilowski, M.; Mahler, B.; Lhuillier, E.; Ithurria, S.; Dubertret, B., Two-Dimensional Colloidal Nanocrystals. *Chem. Rev.* **2016,** *116* (18), 10934-10982.

- Drachev, V. P.; Podolskiy, V. A.; Kildishev, A. V., Hyperbolic metamaterials: new physics behind a classical problem. *Opt. Express* **2013,** *21* (12), 15048-15064.
- Hsu, S. W.; On, K.; Tao, A. R., Localized Surface Plasmon Resonances of Anisotropic Semiconductor Nanocrystals. *J. Am. Chem. Soc.* **2011,** *133* (47), 19072-19075.
- Liu, L. G.; Zhong, H. Z.; Bai, Z. L.; Zhang, T.; Fu, W. P.; Shi, L. J.; Xie, H. Y.; Deng, L. G.; Zou, B. S., Controllable Transformation from Rhombohedral Cu1.8S Nanocrystals to Hexagonal CuS Clusters: Phase- and Composition-Dependent Plasmonic Properties. *Chem. Mater.* **2013,** *25* (23), 4828-4834.
- Kim, S. Y.; Kim, J. H.; Lee, S.; Kwak, J.; Jo, Y.; Yoon, E.; Lee, G. D.; Lee, Z.; Kwon, S. Y., The impact of substrate surface defects on the properties of two-dimensional van der Waals heterostructures. *Nanoscale* **2018,** *10* (40), 19212-19219.
- Kim, K.; Lee, Z.; Regan, W.; Kisielowski, C.; Crommie, M. F.; Zettl, A., Grain Boundary Mapping in Polycrystalline Graphene. *ACS Nano* **2011,** *5* (3), 2142-2146.
- Hashimoto, A.; Suenaga, K.; Gloter, A.; Urita, K.; Iijima, S., Direct evidence for atomic defects in graphene layers. *Nature* **2004,** *430* (7002), 870-873.
- Ago, H.; Fukamachi, S.; Endo, H.; Solis-Fernandez, P.; Yunus, R. M.; Uchida, Y.; Panchal, V.; Kazakova, O.; Tsuji, M., Visualization of Grain Structure and Boundaries of Polycrystalline Graphene and Two-Dimensional Materials by

Epitaxial Growth of Transition Metal Dichalcogenides. *ACS Nano* **2016,** *10* (3), 3233-3240.

- He, F.; Zhou, Y. J.; Ye, Z. F.; Cho, S. H.; Jeong, J.; Meng, X. H.; Wang, Y. G., Moire Patterns in 2D Materials: A Review. *ACS Nano* **2021,** *15* (4), 5944-5958.
- Ryu, Y. K.; Frisenda, R.; Castellanos-Gomez, A., Superlattices based on van der Waals 2D materials. *Chem. Commun.* **2019,** *55* (77), 11498-11510.
- Shimazaki, Y.; Schwartz, I.; Watanabe, K.; Taniguchi, T.; Kroner, M.; Imamoglu, A., Strongly correlated electrons and hybrid excitons in a moire heterostructure. *Nature* **2020,** *580* (7804), 472-+.
- Jin, C. H.; Regan, E. C.; Yan, A. M.; Utama, M. I. B.; Wang, D. Q.; Zhao, S. H.; Qin, Y.; Yang, S. J.; Zheng, Z. R.; Shi, S. Y.; Watanabe, K.; Taniguchi, T.; Tongay, S.; Zettl, A.; Wang, F., Observation of moire excitons in WSe2/WS2 heterostructure superlattices. *Nature* **2019,** *567* (7746), 76-+.
- Han, J. H.; Lee, S.; Cheon, J., Synthesis and structural transformations of colloidal 2D layered metal chalcogenide nanocrystals. *Chem. Soc. Rev.* **2013,** *42* (7), 2581-2591.
- Wulff, G., On the question of speed of growth and dissolution of crystal surfaces. *Z. Krystallog.* **1901,** *34* (5/6), 449-530.
- Barmparis, G. D.; Lodziana, Z.; Lopez, N.; Remediakis, I. N., Nanoparticle shapes by using Wulff constructions and first-principles calculations. *Beilstein J. Nanotechnol.* **2015,** *6*, 361-368.

- Viswanath, B.; Kundu, P.; HaIder, A.; Ravishankar, N., Mechanistic Aspects of Shape Selection and Symmetry Breaking during Nanostructure Growth by Wet Chemical Methods. *J. Phys. Chem. C* **2009,** *113* (39), 16866-16883.
- Peng, X. G.; Manna, L.; Yang, W. D.; Wickham, J.; Scher, E.; Kadavanich, A.; Alivisatos, A. P., Shape control of CdSe nanocrystals. *Nature* **2000,** *404* (6773), 59-61.
- Milliron, D. J.; Hughes, S. M.; Cui, Y.; Manna, L.; Li, J. B.; Wang, L. W.; Alivisatos, A. P., Colloidal nanocrystal heterostructures with linear and branched topology. *Nature* **2004,** *430* (6996), 190-195.
- Xiong, Y. J.; Washio, I.; Chen, J. Y.; Cai, H. G.; Li, Z. Y.; Xia, Y. N., Poly(vinyl pyrrolidone): A dual functional reductant and stabilizer for the facile synthesis of noble metal nanoplates in aqueous solutions. *Langmuir* **2006,** *22* (20), 8563-8570.
- Qi, H.; Huang, J. F.; Cao, L. Y.; Wu, J. P.; Li, J. Y., Controlled synthesis and optical properties of doughnut-aggregated hollow sphere-like CuS. *Ceram. Int.* **2012,** *38* (8), 6659-6664.
- Sun, S. D.; Li, P. J.; Liang, S. H.; Yang, Z. M., Diversified copper sulfide (Cu2-xS) micro-/nanostructures: a comprehensive review on synthesis, modifications and applications. *Nanoscale* **2017,** *9* (32), 11357-11404.
- Geng, W. T.; Wang, V.; Liu, Y. C.; Ohno, T.; Nara, J., Moire Potential, Lattice Corrugation, and Band Gap Spatial Variation in a Twist-Free MoTe2/MoS2 Heterobilayer. *J. Phys. Chem. Lett.* **2020,** *11* (7), 2637-2646.

APPENDIX B

COPYRIGHT PERMISSION

Copyright for Chapter 3

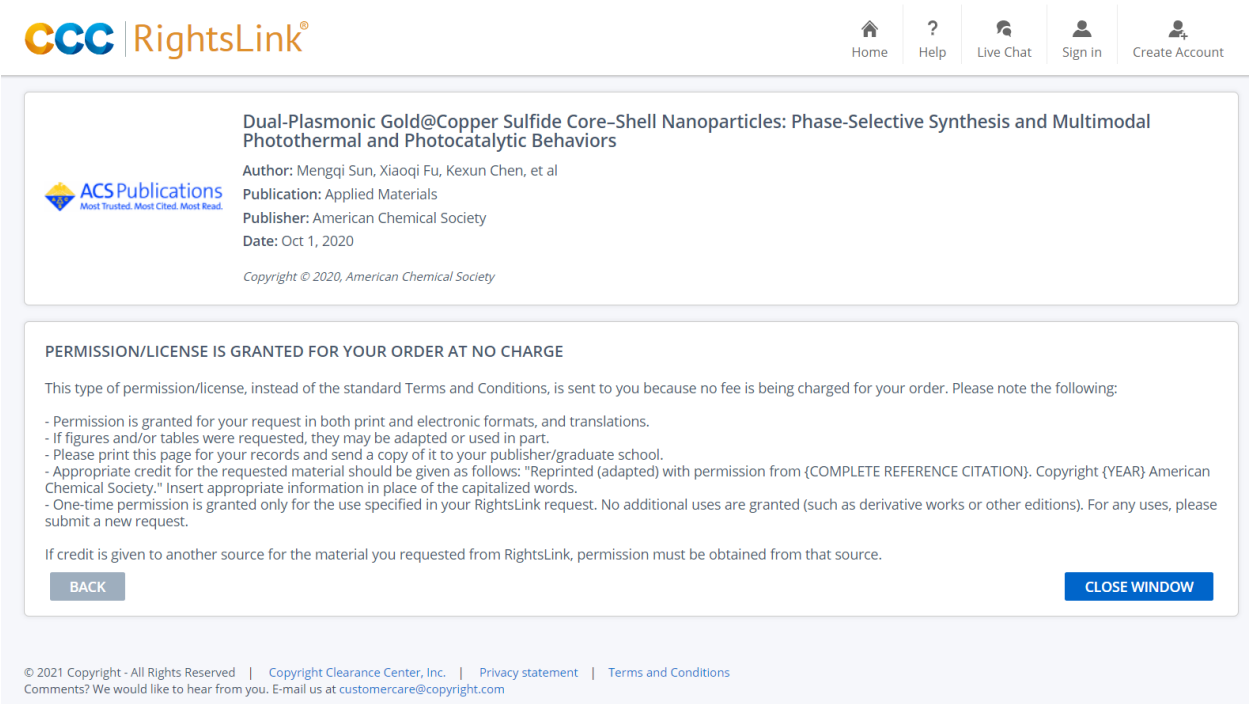

CCC | RightsLink®

Home | Help | Live Chat | Sign in | Create Account

ACS Publications
Most Trusted. Most Cited. Most Read.

Dual-Plasmonic Gold@Copper Sulfide Core–Shell Nanoparticles: Phase-Selective Synthesis and Multimodal Photothermal and Photocatalytic Behaviors

Author: Mengqi Sun, Xiaoqi Fu, Kexun Chen, et al
Publication: Applied Materials
Publisher: American Chemical Society
Date: Oct 1, 2020

Copyright © 2020, American Chemical Society

PERMISSION/LICENSE IS GRANTED FOR YOUR ORDER AT NO CHARGE

This type of permission/license, instead of the standard Terms and Conditions, is sent to you because no fee is being charged for your order. Please note the following:

- Permission is granted for your request in both print and electronic formats, and translations.
- If figures and/or tables were requested, they may be adapted or used in part.
- Please print this page for your records and send a copy of it to your publisher/graduate school.
- Appropriate credit for the requested material should be given as follows: "Reprinted (adapted) with permission from {COMPLETE REFERENCE CITATION}. Copyright {YEAR} American Chemical Society." Insert appropriate information in place of the capitalized words.
- One-time permission is granted only for the use specified in your RightsLink request. No additional uses are granted (such as derivative works or other editions). For any uses, please submit a new request.

If credit is given to another source for the material you requested from RightsLink, permission must be obtained from that source.

BACK CLOSE WINDOW